

Structure-dynamics relations in mixtures of highly charged polymer colloid dispersions

Dissertation

to acquire the academic degree
doctor rerum naturalium (Dr. rer. nat.)
of the Faculty of Mathematics and Natural Sciences
at the University of Rostock

submitted by
M. Sc. Falko Ziegert,
born on November 18, 1987 in Lübz

Rostock, 2017

Referees:

Prof. Dr. Joachim Wagner, University of Rostock

Prof. Dr. Ralf Stannarius, Otto-von-Guericke University Magdeburg

Date of submission: March 24, 2017

Date of scientific colloquium: July 11, 2017

Research for and preparation of this dissertation were performed during the time from October 2013 until March 2017 at the University of Rostock, Institute of Chemistry under supervision of Prof. Dr. Joachim Wagner.

*If your determination is fixed, I do not counsel you to despair.
Few things are impossible to diligence and skill.
Great works are performed not by strength, but perseverance.*

— Samuel Johnson

Zusammenfassung

In der vorliegenden Arbeit werden Struktur-Dynamik-Beziehungen in binären und ternären Mischungen hochgeladener, sphärischer Polymerkolloide untersucht. Experimentellen Zugang zu Struktur und Dynamik liefern statische und quasielastische Lichtstreuexperimente, die mit Index-Matching selektiv die Bestimmung partieller Strukturfaktoren $S_{ij}(Q)$ und intermediärer Streufunktionen $S_{ij}(Q, t)$ ermöglichen. Um den Brechungsindex protischer Wasser/Glycerol-Mischungen auf denjenigen der Polymerpartikel einstellen zu können, wird als kolloidales Modellsystem eine neue Klasse von Copolymer-Partikeln aus Alkyl- und Perfluoroalkylacrylaten entwickelt. Die theoretische Beschreibung erfolgt mit Hilfe von Integralgleichungen und Brownscher Dynamik. Hierzu wird der Ermak-Algorithmus auf Mischungen verschiedener Partikelklassen erweitert. Aus den Trajektorien werden Raum-Zeit-Korrelationsfunktionen berechnet, die mittels räumlicher Fourier-Transformation in die partiellen, intermediären Streufunktionen und Strukturfaktoren überführt werden können. Hiermit ist ein direkter Vergleich mit experimentellen Lichtstreuendaten möglich.

Abstract

In this work structure-dynamics relations in binary and ternary mixtures of highly charged, spherical polymer colloids are investigated. Experimental access to structure and dynamics is provided by static and quasi-elastic light scattering experiments, that enable a selective determination of partial structure factors $S_{ij}(Q)$ and intermediate scattering functions $S_{ij}(Q, t)$ by index-matching. To adjust the refractive index of water/glycerol mixtures to that of the polymer particles, a new class of copolymer particles consisting of alkyl and perfluoroalkyl acrylates is developed as a colloidal model system. Integral equations and Brownian Dynamics are employed for a theoretical description. To that end the Ermak algorithm is extended to mixtures of different particle classes. From the trajectories space-time correlation functions are determined, which may be converted into partial, intermediate scattering functions and structure factors by spatial Fourier transform. Thus, a direct comparison with experimental light scattering data is possible.

Contents

List of abbreviations	VIII
1 Introduction	1
2 Theoretical principles	4
2.1 Colloids	4
2.2 Theory of Brownian Dynamics simulations	6
2.3 Theory of light scattering	8
2.3.1 Static light scattering	9
2.3.2 Dynamic light scattering	10
3 Methods	17
3.1 Monomer preparation	17
3.2 Emulsion polymerisation	17
3.3 Determination of the particle refractive index	18
3.4 Light scattering experiments	20
3.4.1 Determination of the particle size	20
3.4.2 Determination of the static structure factor	22
3.4.3 Investigation of collective diffusion	23
3.5 Brownian Dynamics simulations	24
3.5.1 Simulation of homo-colloidal systems	26
3.5.2 Simulation of binary mixtures	26
3.5.3 Simulation of ternary mixtures	26
4 Preparation and characterisation of colloidal model systems	27
4.1 Synthesis of fluorinated alkyl acrylates	27
4.2 Preparation of colloidal polymer particles	27
4.3 Characterisation of particle-specific properties	30
4.4 Characterisation of self-organised single compound systems	35
4.5 Influence of index-matching with glycerol on the number of surface charges	41
5 Investigations of binary mixtures	43
5.1 Tracer particles in a homo-colloidal matrix	43
5.1.1 Light scattering investigations of tracer self-diffusion in a homo-colloidal matrix	43
5.1.2 Brownian Dynamics simulations of tracer self-diffusion in a homo-colloidal matrix	53
5.2 Binary mixtures with similar number densities	58
5.2.1 Intermediate scattering functions obtained by light scattering experiments and Brownian Dynamics simulations	58

5.2.2	Systematic simulation study on influences of system parameters on the intermediate scattering function	66
6	Investigations of ternary mixtures	79
7	Summary and outlook	88
	Appendix	IX
A	Nuclear magnetic resonance spectra of prepared fluorinated acrylates	X
B	Intermediate scattering functions for BB and AB correlations	XIII
C	Relaxation of intermediate scattering functions for BB and AB correlations	XV
	List of figures	XVII
	List of tables	XXIV
	Bibliography	XXVI

List of abbreviations

AC	acryloyl chloride
BA	n-butyl acrylate
BD	Brownian Dynamics
DLS	dynamic light scattering
DLVO	Derjaguin-Landau-Verwey-Overbeek
DWS	diffusing-wave spectroscopy
HCl	hydrochloric acid
HQ	hydroquinone
IUPAC	International Union of Pure and Applied Chemistry
MD	Molecular Dynamics
MSA	mean spherical approximation
MSD	mean squared displacement
NMR	nuclear magnetic resonance
OFFP	1H,1H,5H-octafluoropentanol
OFPA	1H,1H,5H-octafluoropentyl acrylate
OZ	Ornstein-Zernike
pBA	poly(n-butyl acrylate)
pOFPA	poly(1H,1H,5H-octafluoropentyl acrylate)
PS	polystyrene
pTcB	poly(TFEA-co-BA)
pTcO	poly(TFEA-co-OFPA)
pTFEA	poly(2,2,2-trifluoroethyl acrylate)
PY	Percus-Yevick
RMSA	rescaled mean spherical approximation
SAS	small angle scattering
SE	Stokes-Einstein
SLS	static light scattering
TFE	2,2,2-trifluoroethanol
TFEA	2,2,2-trifluoroethyl acrylate

1 Introduction

Soft matter denotes a subgroup of condensed matter comprising systems such as foams, gels, proteins, other polymers, microemulsions, or colloids. A common property of all these complex systems is their structural response to an external constraint with an energy comparable to the thermal energy $k_B T$ at room temperature, where k_B is the Boltzmann constant and T the temperature. Since also proteins and DNA with their secondary and tertiary structure or lipid membranes are typical soft matter systems, self-organisation of soft matter at mesoscopic length scales and comparably slow dynamic processes in such systems are of importance for life. On the one hand, mesoscale structures often are too small for direct observation with a microscope. On the other hand, they are orders of magnitude larger than molecular length scales, information on which may be obtained by scattering experiments with X-Rays or neutrons with wavelengths from ångströms to nanometres. The progress in experimental soft matter research during the last decades is strongly related to the emergence of scattering techniques with high spatial and energy resolution. Particularly the development of quasi-elastic scattering experiments analysing temporal fluctuations of scattered coherent radiation, i. e., photon correlation spectroscopy employing laser light [1] or coherent X-Rays [2], has given access to processes at relevant time scales from microseconds to seconds. The insights based on these experimental methods have helped understanding natural soft matter systems and have enabled the design of synthetic soft matter systems with tailor-made properties.

Colloidal systems have been investigated ever since the middle of the 19th century, when especially the works of the Scottish chemist Thomas Graham constituted the field of interface and colloid science [3, 4]. At the beginning of the 20th century the German scientist Wolfgang Ostwald became another pioneer of colloid chemistry [5–7]. His designation of colloidal systems as the "world of neglected dimensions" [6] proves that even at the time he recognised the great potential of this kind of soft matter. Nowadays colloids are an interesting example of the variety of both naturally existing and synthetically prepared soft matter, with great significance in biological domains, technical applications, and everyday life. A more detailed approach to the theory of colloids is given in section 2.1.

Throughout the last decades extensive investigations, particularly of polymer colloids, have lead to an in-depth understanding of structure and dynamics of single species colloidal dispersions. Different particle interactions such as hard-sphere repulsion [8–10], soft short-range interactions [11, 12], long-range electrostatic repulsion [13–16], and even multipole interactions resulting from electric [17] and magnetic dipoles [18, 19] and electrostatic quadrupoles [20, 21] can be introduced by appropriate surface functionalities or volume properties of the colloidal particles. These systems with a multitude of possible interactions can be considered as model systems at enlarged scales of length and time for atomic or molecular condensed matter [22, 23]. Since typical colloidal length scales are comparable with optical wavelengths, coherent laser light is a suitable probe for investigations of structure-dynamics relations in such systems by means of laboratory methods, that are comparably easily realisable. To observe analogous phenomena in atomic or

molecular systems, access to large scale research facilities would be necessary. If possible at all to cover several magnitudes of time as provided by photon correlation spectroscopy, a combination of multiple neutron spectrometers or admission to coherent X-Rays at third generation synchrotron sources or free electron lasers would be required.

Due to size polydispersity, natural and synthetic colloids are in fact mixtures of diversely sized species, which differently interact based on responsible volume and surface related properties. A systematic approach to investigate such real dispersions is the preparation of mixtures of various species, each with a narrow particle size distribution. The complexity of colloidal mixtures is enhanced by influences of the ratios of particle sizes, number densities and potential energy between particles of the mixed species, compared to a single component, in first approximation monodisperse system. The knowledge about effects of these additional parameters on structure and dynamics of colloidal mixtures is sparse. Sophisticated methods including X-Ray and neutron scattering experiments often are necessary due to opacity of available colloidal model systems, such as poly(methyl methacrylate) (PMMA) or polystyrene (PS), at moderate concentrations for radiation with optical wavelengths caused by refractive indices of these polymer materials much larger than, for example, those of aqueous dispersion media [24]. However, such techniques are limited to a finite number of large scale research centres, including synchrotron radiation or neutron sources, and being granted the opportunity for performing experiments there is in great demand. Therefore, the development of new colloidal materials with properties that facilitate investigations with readily available physical and chemical laboratory techniques is highly desirable, to give access to a shortcut path to new insights in soft matter physics.

In this work, a new class of monodisperse, charge-stabilised colloidal particles composed of a copolymer consisting either of two different, highly fluorinated alkyl acrylates or one highly fluorinated alkyl acrylate and n-butyl acrylate is prepared for the first time by emulsion polymerisation, introducing highly acidic sulfonic acid surface groups for stabilisation of the particles in protic dispersion media. The striking feature of these copolymer particles is the tunability of the particle refractive index n_p in a comparably low domain $1.380 \leq n_p \leq 1.449$, depending on the molar ratio of the two copolymerised monomers, enabling index-matching in protic water/glycerol mixtures as dispersion media. Although two color cross-correlation [25] or diffusing wave spectroscopy [26] with visible light are well-established methods that may be employed in standard laboratories to overcome difficulties caused by multiple scattering due to a large particle refractive index, utilising low refractive index polymers in an index-matched, protic dispersion medium is an elegant way to suppress multiple scattering even in concentrated dispersions.

The characteristics of the prepared particles, such as particle sizes and polydispersities, as well as dynamical properties of dilute homocolloidal systems are investigated by means of dynamic light scattering experiments. Pronounced liquid-like structures formed by self-organisation of the prepared colloidal particles, interestingly even at unusually low volume fractions $\varphi < 0.005$, are probed by static light scattering experiments. The electrostatic interaction as quantified by the effective number of surface charges, is investigated via integral equations describing the static structure factors of self-organised systems and by Brownian Dynamics simulations reproducing the experimentally obtained structure factors. The refractive index of (co)polymer particles is determined from spectrophotometric transmission experiments varying the refractive index of the dispersion medium by changing the composition of water/glycerol mixtures.

The particle sizes determined from dilute, aqueous dispersions of prepared (co)polymer

particles as well as their numbers of effective surface charges and number densities derived from the equilibrium structure of self-organised, moderately concentrated dispersions are used for the considered preparation of mixtures of highly charged colloids. Binary systems in terms of strongly scattering tracer particles in an index-matched matrix of highly fluorinated poly(alkyl acrylate) spheres are investigated by means of static and dynamic light scattering experiments and theoretically modelled by Brownian Dynamics simulations to quantify the influences of changing tracer and matrix particle number densities on the short-time and long-time self-diffusion coefficients of tracers in the binary mixture.

Static and dynamic light scattering experiments are performed, complemented by Brownian Dynamics simulations, to illustrate the comparably easy access to partial static and dynamic intermediate scattering functions $S_{ij}(Q)$ and $S_{ij}(Q, t)$, respectively, in mixtures of two moderately concentrated colloidal species with similar number densities, exploiting the possibility of index-matching given by the newly prepared (co)polymer colloids. Simultaneously, the imperative of a high degree of diligence while selectively index-matching one component for scattering experiments is emphasised. In further Brownian Dynamics simulations of realistic binary mixtures, independent of the performed light scattering experiments, the complex influences of varying system parameters, such as the ratio of particle sizes, ratio of number densities, ratio of numbers of effective surface charges, and temperature, on structure as well as collective dynamics of the mixture are systematically investigated. These simulations reveal comprehensive information about the effects of these parameters on binary mixtures of moderately concentrated, highly charged, spherical particles that have not been studied so far.

The last part of this work comprises systematic Brownian Dynamics simulations of ternary colloidal mixtures, in terms of tracer particles in a matrix composed of two different colloidal species. Under systematic variation of particle sizes, number densities and effective surface charges of the matrix particles as well as the total colloidal number density of the system and the ionic strength of the dispersion medium, intriguing results about the influences of these varying parameters on the self-organisation of the matrix particles and hence the self-diffusion behaviour of the tracer particles are obtained for the first time.

2 Theoretical principles

2.1 Colloids

The term "colloid" in its simplest meaning describes a mixture of two components, one being microscopically dispersed in the other. While in a solution solute and solvent form one common phase, a colloid per definition is a heterogeneous system composed of a dispersed phase and the surrounding continuous phase, even though macroscopically it may appear homogeneous. Thus a colloid can only be formed, if the dispersed particles are insoluble in the continuous medium.

Depending on the aggregate states of the two components, colloidal dispersions can be divided into several classes [27], compiled in table 2.1. This classification in principle already dates back to Wolfgang Ostwald [5, 28], a German pioneer in colloid science of the early 20th century. Examples of some of these classes may be encountered every day, e. g., smoke (solid particles in a gaseous phase), fog (liquid droplets in a gaseous phase) or lather (gas bubbles in a liquid phase).

Table 2.1: General classification of colloidal dispersions depending on the aggregate states of dispersed and continuous phase

		Continuous phase		
		gaseous	liquid	solid
Dispersed phase	gaseous	n/a	foam	solid foam
	liquid	liquid aerosol	emulsion	solid emulsion or gel
	solid	solid aerosol	suspension or sol	solid sol

After Ostwald, Hermann Staudinger, one of the fathers of macromolecular chemistry, approached the colloidal state from a thermodynamic and structural point of view [28]. His classification into dispersion colloids, molecular colloids and associated colloids is also valid up to now, albeit with the progress of colloid science various sub-classes have been defined.

Beside the two-phase character there is a second part to the definition of a colloid regarding the size of the dispersed particles. According to the International Union of Pure and Applied Chemistry (IUPAC) the term "colloidal" refers to a "state of subdivision such that the molecules or polymolecular particles dispersed in a medium have at least one dimension between approximately 1 nm and 1 μm , or that in a system discontinuities are found at distances of that order" [29]. However, due to the mesoscale character of colloids as a fluent link between the molecular dimension of true solutions and macroscopically heterogeneous systems, the length scale boundaries are not at all rigid. Other than the IUPAC definition, upper size limits ranging from only 500 nm up to 10 μm can be found in the literature [27, 28].

There are a lot of natural examples for colloidal systems, many of them consisting of latex, i. e., a "colloidal dispersion of polymer particles in a liquid" (IUPAC [29]). In

general, the polymer in that sense can be organic or inorganic. One very important material in natural latices is *cis*-1,4-polyisoprene, also called natural rubber, that can be found in the Brazilian rubber tree, *Hevea brasiliensis* [30, 31]. Due to its unique high performance properties, natural rubber even today is a significant raw material for industrially processed products.

After substantial progress in the field of colloid science since the early 20th century, today synthetic colloids are an essential part of everyday life, e. g., in paints, coatings or pharmaceuticals. Naturally existing colloids have been widely complemented with synthetic colloidal systems, for the preparation of which several techniques have been developed. Basically, one can distinguish between two ways of preparing colloids. On the one hand, there is the bottom-up preparation starting from smaller molecules and polymerising those into nanoparticles inside a given medium. On the other hand, a bulk material can be finely dispersed in another one to result in a colloidal system, which is referred to as a top-down approach.

This work deals with dispersion colloids of polymer particles in liquid media. If the permittivities and the polarisabilities of dispersed particles and dispersion medium differ, a short-range attractive dispersion or van der Waals potential V_a [28, 32] acts between the particles due to the emergence of induced electric dipoles.

$$V_a(r_{ij}) = -\frac{A}{6} \left[\frac{2R^2}{r_{ij}^2 - 4R^2} + \frac{2R^2}{r_{ij}^2} + \ln \left(\frac{r_{ij}^2 - 4R^2}{r_{ij}^2} \right) \right] \quad (2.1)$$

In 2.1 A denotes the Hamaker constant, r_{ij} the particle interdistance and R the particle radius.

As a consequence, these colloids are thermodynamically unstable and would finally agglomerate. Thus, to maintain the colloidal state, a stabilisation mechanism has to be introduced, three of which can be principally distinguished [30]:

- a) Electrostatic - like-charged surface stabiliser groups introduce a long-range electrostatic repulsive potential between particles
- b) Steric - repulsion by osmotic and entropic forces when sterically demanding stabiliser surface layers of approaching particles overlap
- c) Electrosteric - polyelectrolyte surface groups exhibit a competition between osmotic pressure inside the polyelectrolyte layer and entropic elasticity of the polyelectrolyte chains

The colloids in this work are electrostatically stabilised by the introduction of highly acidic sulfonic acid groups during preparation (cf. section 3.2). In protic media, such as water, alcohols or mixtures of both, these acid groups dissociate, such that the particle surface is negatively charged. Due to the surrounding positively charged counter ion cloud, an electric double layer is formed, resulting in a screened Coulomb potential V_c , that for two colloidal macroions i and j has the form

$$V_c(r_{ij}) = \frac{(Z_{\text{eff}}e_0)^2}{4\pi\epsilon_0\epsilon_r r_{ij}} \cdot \exp\left(-\frac{r_{ij}}{\lambda_D}\right), \quad (2.2)$$

with the number of effective surface charges Z_{eff} , the elementary charge e_0 , the absolute permittivity $\varepsilon_0\varepsilon_r$ and the Debye length λ_D . In electrolytes the latter is a function of the ionic strength I

$$\lambda_D = \sqrt{\frac{\varepsilon_0\varepsilon_r k_B T}{2N_A e_0^2 I}}, \quad (2.3)$$

where k_B denotes the Boltzmann constant, T is the temperature and N_A the Avogadro constant, which in German literature is also referred to as Loschmidt constant. Thus, the presence of stray ions leads to a stronger screening of the Coulomb potential. The combination of van der Waals attraction according to (2.1) and electrostatic repulsion according to (2.2) leads to the commonly known Derjaguin-Landau-Verwey-Overbeek (DLVO) potential [33, 34].

By variation of the ionic strength of the dispersion medium and the number density ϱ of dispersed particles a rich phase behaviour is accessible in charged dispersion colloids. In the absence of stray ions, where only protons as counter ions are present, and even at comparably low volume fractions of $\varphi \approx 10^{-3}$ charged colloidal particles self-organise not only into liquid-like structures [13], but also colloidal crystals [35, 36] or even glasses [37]. Due to the comparably large range of electrostatic interaction the volume fractions of particles, necessary to form these structures, are much smaller than for particles interacting via a hard body potential [17, 38].

As colloidal dispersions exhibit this rich phase behaviour, they have been considered model systems of condensed matter for a long time and significant contributions to fundamental phenomena in the physics of condensed matter have been made. Still today colloidal systems are of great significance, e. g., in the process of understanding the glass transition that still is one of the major challenges in condensed matter physics. The reason for the successful utilisation of colloids as model systems are the larger length (comparable to optical wavelengths) and time (ms to s) scales of relevance, compared to molecular matter ($\ll 1$ nm, range of ps), that enable the application of a variety of modern methods to study the structure and dynamics of colloidal systems. This ranges from microscopy methods (transmission electron microscopy [39], fluorescence confocal laser scanning microscopy [40]), that allow the direct observation of colloidal systems, to the most different scattering or scattering-related techniques (diffusing-wave spectroscopy (DWS) [41, 42], small angle scattering (SAS) [43, 44], light scattering [22]), from which indirectly conclusions regarding colloidal structure and dynamics can be drawn.

2.2 Theory of Brownian Dynamics simulations

The random motion of particles dispersed in a fluid is called Brownian motion, in honour of the Scottish botanist Robert Brown, who first described this phenomenon after he observed pollen [45] and later dust particles in water. The first to observe similar motions of carbon dust particles was Jan Ingenhousz [46], who did not further investigate on the topic though. The cause of this random motion was theoretically described in the early 20th century by Albert Einstein, Marian von Smoluchowski and Paul Langevin [47–49], who pointed out, that the Brownian particles move due to collisions with the much faster molecules of their surrounding medium. Shortly after, Jean-Baptiste Perrin experimentally proved this theoretical approach to be correct [50]. Two of the first scientists to

describe the mathematical basics of Brownian motion were Thorvald Niclas Thiele and Norbert Wiener [51, 52].

The Einstein-Smoluchowski diffusion equation in three dimensions

$$\langle r^2 \rangle = 6D_E t, \quad (2.4)$$

with the mean squared displacement (MSD) $\langle r^2 \rangle$, the time t and the Einstein diffusion coefficient D_E , describes the diffusive motion of Brownian particles. Under the assumption of spherical particles, the Stokes-Einstein equation (2.17) can be obtained.

Nowadays, computer simulations are a widely applied and powerful tool for the prediction of experimental properties or for comparing specific models to purely theoretical and experimental findings. Sufficient computing power is more or less easily available to simulate the behaviour even of complex systems, e. g., by means of Molecular Dynamics (MD) methods. However, trying to model a colloidal system consisting of the dispersed particles and the comparably large number of molecules of the dispersion medium via MD simulations with sufficient statistics, would still be impractical and time-consuming if not impossible at all. Assume a typical system of colloidal particles dispersed in water. The number densities of water molecules, ${}^1\rho_{\text{H}_2\text{O}} \approx 10^{28} \text{ m}^{-3}$, and of the dispersed particles, ${}^1\rho_{\text{coll.}} \approx 10^{18} \text{ m}^{-3}$, would vary by about ten orders of magnitude. However, due to the discrepancy in size, colloidal particles also move much slower than water molecules, which can be quantified by typical diffusion coefficients ($D_{\text{SE}}^{\text{H}_2\text{O}} \approx 10^{-9} \text{ m}^2 \text{ s}^{-1}$ vs. $D_{\text{SE}}^{\text{coll.}} \approx 10^{-12} \text{ m}^2 \text{ s}^{-1}$). Therefore, the molecules of the dispersion medium can be considered a continuum, that instantaneously reacts to the motion of the dispersed particles on the relevant time scale, which is exploited in Brownian Dynamics (BD) simulations. Zwanzig and Mori achieved the separation of the fast dynamics of the dispersion medium from the slow dynamics of the colloidal particles via a simplification of the equations of motion of such a colloidal system by application of a projection operator [53, 54]. The resulting equations of motion can be numerically integrated following the Ermak algorithm [55]

$$\mathbf{r}_i(t + \Delta t) = \mathbf{r}_i(t) + \frac{D_0}{k_B T} \mathbf{F}_i(t) \Delta t + \mathbf{R}_i + \mathcal{O}(\Delta t^2), \quad (2.5)$$

with \mathbf{r}_i denoting the position vector of the simulated particle before and after a time step Δt . For the investigation of charged particles the second term describes the motion caused by an electrostatic force \mathbf{F}_i , originating from the effective screened Coulomb potential, proportional to the ratio of short-time self-diffusion coefficient and thermal energy $D_0/(k_B T)$, which is the reciprocal Stokes friction coefficient of a sphere $\xi^{-1} = (6\pi\eta a)^{-1}$ with the dynamic viscosity η and the sphere radius a . \mathbf{R}_i is a random displacement due to Brownian motion of the particle, that underlies a Gaussian probability distribution with $\langle \mathbf{R}_i \rangle = 0$ and has a mean square value $\langle \mathbf{R}_i^2 \rangle = 6D\Delta t$. In this way the trajectories of a given number of particles can be computed and the coordinates of each particle at each time step are known. Thus, the pair distribution function $g^{(2)}(r)$ and the MSD $\langle r^2 \rangle$ are accessible for the characterisation of the colloidal structure and self-dynamics. The computation of the partial, distinct space-time pair distribution function in mixtures, $g_{ij}^{(2)}(r, t)$, from trajectories of Brownian systems is also possible, although computationally much more demanding than determining the MSD. However, $g_{ij}^{(2)}(r, t)$ enables an access

to collective dynamics of colloidal dispersions. Details on the method of BD simulations performed in this work are given in section 3.5.

2.3 Theory of light scattering

Electromagnetic radiation interacts with matter. Due to the typical colloidal length scales (cf. 2.1) visible light, with wavelengths λ in the range $400 \text{ nm} \leq \lambda \leq 700 \text{ nm}$, is a suitable probe for the investigation of structure and dynamics of colloidal systems by evaluation of scattering experiments.

If a primary electromagnetic wave hits a colloidal material, the electric field vector induces a fluctuating dipole moment which is related to the electric field by the polarisability tensor. Thus the colloidal particles can be described as oscillating Hertzian dipoles, which emit secondary electromagnetic waves. The interference pattern resulting from the entirety of secondary waves can be detected as a characteristic angle-dependent intensity called scattering function $I(\mathbf{Q})$. The analysis of a time-dependent scattering function $I(\mathbf{Q}, t)$ enables conclusions regarding not only the structure but also the dynamics of the investigated sample. $\mathbf{Q} = \mathbf{k}_i - \mathbf{k}_f$ is the scattering vector, defined as the difference of wave vectors of the incident wave \mathbf{k}_i and the final wave after scattering \mathbf{k}_f . A schematic representation of the scattering geometry is displayed in Fig. 2.1.

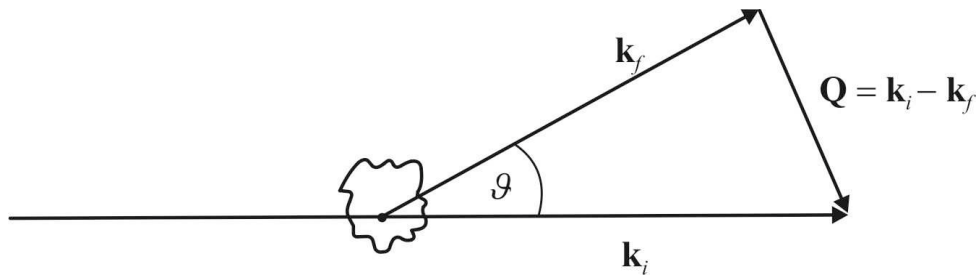


Fig. 2.1: Typical geometry of a scattering event caused by interaction of light with matter. The angle between the wave vectors of incident wave \mathbf{k}_i and scattered wave \mathbf{k}_f is designated as ϑ . The wave vector difference $\mathbf{Q} = \mathbf{k}_i - \mathbf{k}_f$ is the scattering vector.

For isotropic systems, the scattering function solely depends on the modulus of the scattering vector

$$|\mathbf{Q}| = Q = \frac{4\pi n}{\lambda} \sin \frac{\vartheta}{2}, \quad (2.6)$$

that is a function of the scattering angle ϑ , the vacuum wavelength of the probe λ and the refractive index of the sample n [56].

To access information regarding the time-averaged structure of a probed sample, the average scattering intensity is analysed in static light scattering (SLS) experiments. On the other hand, dynamic light scattering (DLS) is employed to obtain information about the dynamics of an investigated system. Both SLS and DLS are widely used methods for the characterisation of colloidal dispersions and are of great significance for the experimental investigations in this work.

2.3.1 Static light scattering

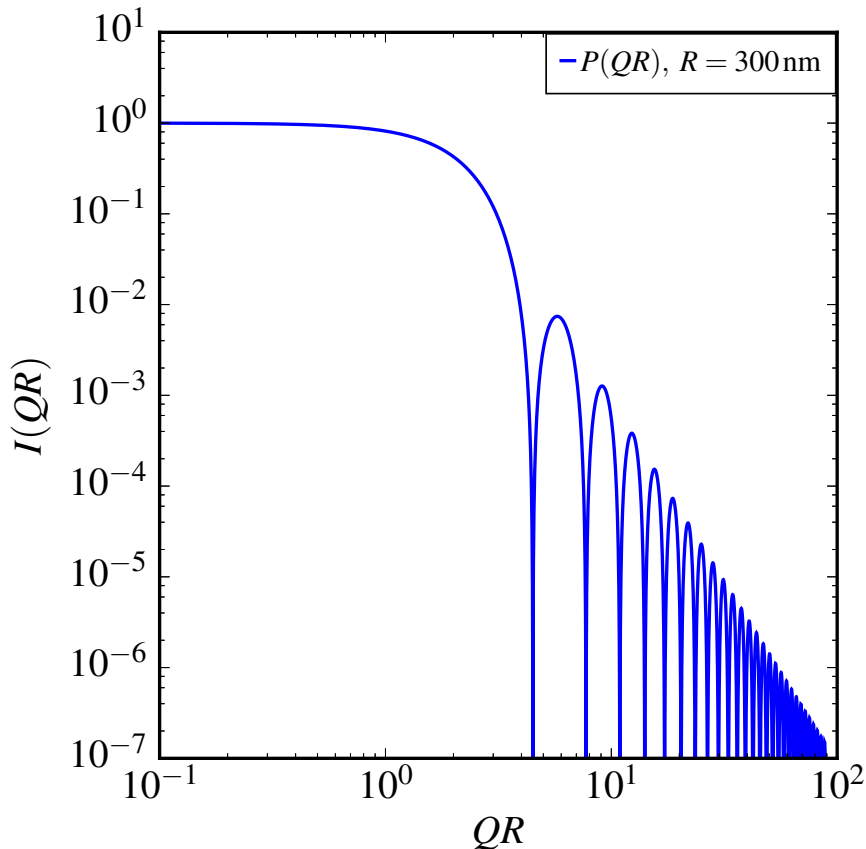
In reciprocal space, for spherically symmetric particles, the scattered intensity $I(Q)$ factorises as [57]

$$I(Q) \propto S(Q) \cdot P(Q) \quad (2.7)$$

with $S(Q)$ denoting the structure factor and $P(Q)$ the particle form factor. The structure factor accounts for interparticle correlations whereas the particle form factor describes intraparticle correlations. For ideally monodisperse, spherical particles the form factor in dependence on the reduced scattering vector QR can be expressed as [58]

$$P(QR) = \left(3 \frac{\sin(QR) - QR \cos(QR)}{(QR)^3} \right)^2, \quad (2.8)$$

where R is the radius of the particles. An extract of the theoretical form factor of monodisperse spheres with $R = 300$ nm is shown in figure 2.2. The first minimum has a characteristic significance, as it always is observed at $QR \approx 4.49$ [59].



For dilute systems, in the absence of particle interactions, colloids behave as ideal gases with $S(Q) \equiv 1$, such that $I(Q) \propto P(Q)$. For systems of colloidal spheres, in which interparticle correlations cannot be neglected, the structure factor of an isotropic, liquid-like system is given by a Fourier-Bessel transform [16, 60]

$$S(Q) = 1 + 4\pi {}^1\varrho \int_0^\infty [g^{(2)}(r) - 1] j_0(Qr) r^2 dr, \quad (2.9)$$

where ${}^1\varrho$ is the particle number density, $g^{(2)}(r)$ the distinct pair distribution function in dependence on the distance r and $j_0(Qr) = \sin(Qr) \cdot (Qr)^{-1}$ denotes the spherical Bessel function of zeroth order.

The structure of simple liquids is theoretically well understood. There are a number of established models, all of which are based on the Ornstein-Zernike (OZ) equation [61]

$$h(r_{12}) = c(r_{12}) + {}^1\varrho \int c(r_{13}) h(r_{23}) d\mathbf{r}_3, \quad (2.10)$$

which separates the total correlation function $h(r) = g^{(2)}(r) - 1$ into a direct part and an indirect part. $c(r_{12})$ describes interactions directly caused by the pair potential between two particles 1 and 2. The integral term proportional to ${}^1\varrho$ accounts for indirect interactions between particles 1 and 2 mediated by a third particle of the N -particle system, depending on the position of that particle \mathbf{r}_3 . By infinite recursion, (2.10) leads to a hierarchy of equations, regarding influences of the other $N - 3$ particles, for the solution of which additional approximations, known as closure relations, are necessary. With respect to the interaction potential in different sorts of liquid systems, several different closure relations have been developed, that combined with the OZ-equation enable the theoretical approximation of the structure of liquids. Examples for these closure relations are the Percus-Yevick (PY) relation for systems dominated by a hard-sphere potential [62] or the mean spherical approximation (MSA), that delivers good results for short-range attractive or repulsive potentials [63]. The obtainment of unphysical negative values for $g(r)$ at small volume fractions [64] is corrected by a rescaling of the real system proposed by Hansen and Hayter [65] (rescaled mean spherical approximation (RMSA)). RMSA is a suitable technique for the quick determination of particle number density and potential parameters in a system dominated by electrostatic interactions, like the effective number of surface charges Z_{eff} , due to the availability of a semianalytical solution of the resulting integral equation for a screened Coulomb potential and a good approximation of experimental data for $S(Q)$ around the coordination maximum. However, one has to be aware that RMSA overestimates Z_{eff} and for larger Q increasingly bad agrees with experimental data.

2.3.2 Dynamic light scattering

Due to temporal fluctuations of the local dielectric constant inside an illuminated sample the scattered intensity also exhibits fluctuations over time [56]. These specific sample-dependent fluctuations can be analysed by means of an intensity autocorrelation function

$$g_2(\tau) = \frac{\langle I(t) \cdot I(t + \tau) \rangle}{\langle I(t) \rangle^2}, \quad (2.11)$$

which is normalised, such that it takes on values between 2, for time increments $\tau \rightarrow 0$, and 1, for $\tau \rightarrow \infty$. Experimentally, $g_2(\tau)$ is accessible via homodyne scattering experiments, where the scattered light of different sub-ensembles of the scattering volume is optically mixed before detection. Therefore, $g_2(\tau)$ is also called homodyne autocorrelation function.

If in a scattering experiment a small portion of the primary beam is mixed with the scattered light, this is called heterodyne optical mixing. The corresponding autocorrelation function

$$g_1(\tau) = \frac{\langle E(t) \cdot E^*(t + \tau) \rangle}{\langle E(t) \cdot E^*(t) \rangle} \quad (2.12)$$

accounts for fluctuations of the scattered electric field [56] and thus is called heterodyne or field autocorrelation function. For ergodic systems, e. g., liquid-like ordered colloids, $g_2(\tau)$ and $g_1(\tau)$ are related via the expression

$$g_2(\tau) = 1 + \beta [g_1(\tau)]^2, \quad (2.13)$$

with a correction factor β that accounts for the average number of speckles detected in an experiment. If an appropriate laser light source is employed, $\beta \approx 1$, such that for a Gaussian distribution of the fluctuations of the electric field $g_2(\tau)$ and $g_1(\tau)$ are simply related via

$$g_1(\tau) = \sqrt{g_2(\tau) - 1}, \quad (2.14)$$

the Siegert equation [66]. With these prerequisites it is possible to determine the intensity autocorrelation function from a homodyne experiment, the setup of which is more easily realisable than a heterodyne experiment, and transform it into the field autocorrelation function via (2.14). Obviously, $g_1(\tau)$ can take on values between 1 ($\tau \rightarrow 0$) and 0 ($\tau \rightarrow \infty$). An intensity and a corresponding field autocorrelation function, typical for a colloidal system, are displayed in Fig. 2.3.

Under the condition of free Gaussian diffusion the functional form of the field autocorrelation function is

$$g_1(\tau) = \exp(-\Gamma\tau), \quad (2.15)$$

for a system with exactly one relaxation process, e. g., an ideally monodisperse colloid. Γ is the inverse relaxation time or relaxation rate related to the Einstein diffusion coefficient D_E via

$$\Gamma = D_E Q^2, \quad (2.16)$$

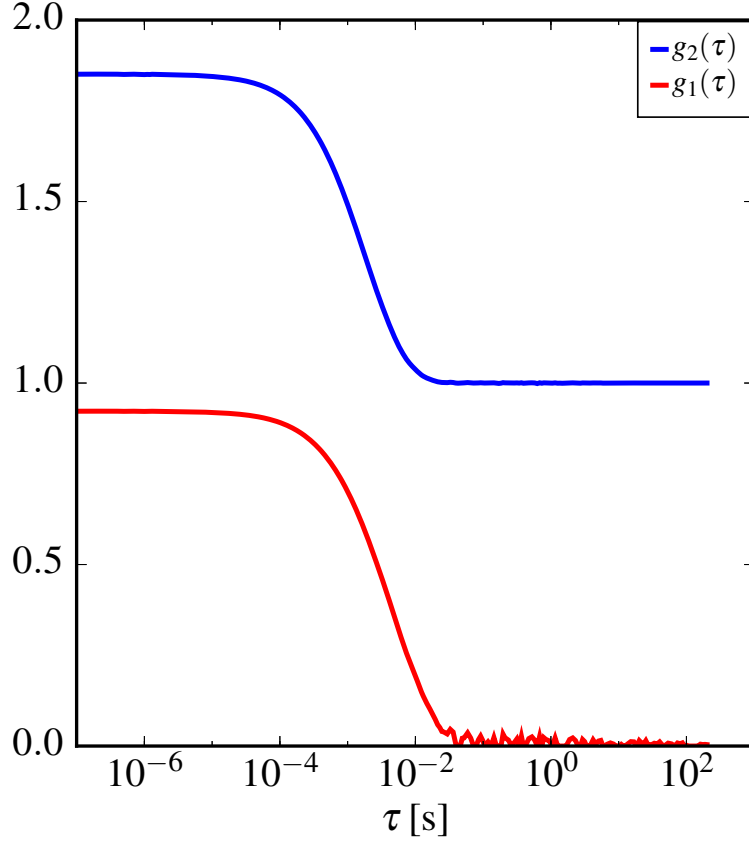


Fig. 2.3: Examples for an intensity autocorrelation function $g_2(\tau)$, determined by means of a homodyne scattering experiment, and the corresponding field autocorrelation function $g_1(\tau)$, obtained using the Siegert equation (2.14).

known as the Landau-Placzek relation [57, 67]. For spherical particles in an aqueous medium at low Reynolds number, this also holds for the Stokes-Einstein (SE) diffusion coefficient [47]

$$D_{\text{SE}} = D_0 = \frac{k_{\text{B}}T}{\xi} = \frac{k_{\text{B}}T}{6\pi\eta R_{\text{h}}}, \quad (2.17)$$

where ξ is the drag coefficient, η denotes the dynamic viscosity of the medium and R_{h} the hydrodynamic radius of the particles. (2.17) in this form is only valid for systems, that meet the stick boundary or no-slip condition, which is the case for particles that are large compared to the molecule size of the dispersion medium.

Real systems ordinarily exhibit a certain degree of polydispersity, so that due to a distribution of diffusion coefficients $g_1(\tau)$ has to be expressed as a sum of exponentials or an integral [68]

$$g_1(\tau) = \lim_{n \rightarrow \infty} \sum_{i=1}^n G_i(\Gamma_i) \exp(-\Gamma_i \tau) = \int_0^{\infty} G(\Gamma) \exp(-\Gamma \tau) d\Gamma, \quad (2.18)$$

with the normalised distribution function of the relaxation rates $G(\Gamma)$, that contains information on the size distribution of the observed polydisperse system. The inversion of (2.18) to extract $G(\Gamma)$ from experimental data of $g_1(\tau)$ is known as an ill-posed problem [69]. To overcome this, different techniques have been developed, such as the cumulant method [68, 70] or the CONTIN algorithm [71, 72]. The latter utilises Laplace transformation and Tikhonov regularisation [73] for numerical treatment of the ill-posed problem. In this work, the CONTIN algorithm is employed for the determination of the size distribution of real colloidal dispersions (cf. 3.4.1).

In moderately dilute dispersions of spherical colloidal particles D_0 very well agrees with

$$\lim_{t \rightarrow "0"} D_S(t) = D_S^S, \quad (2.19)$$

the short-time limit of the time-dependent self-diffusion coefficient $D_S(t)$, where $t \rightarrow "0"$ describes times larger than typical momentum relaxation times in the order of $\tau_B \approx 10^{-8}$ s but smaller than typical structural relaxation times in the order of $\tau_t \approx 10^{-4}$ s [74].

For times long compared to τ_t there is another significant value D_S^L ,

$$\lim_{t \rightarrow \infty} D_S(t) = \lim_{t \rightarrow \infty} \frac{1}{6t} \langle r^2 \rangle = D_S^L, \quad (2.20)$$

the long-time self-diffusion coefficient [75]. Equation (2.20) originates from the Einstein-Smoluchowski diffusion equation (2.4) from section 2.2, where $\langle r^2 \rangle$ denotes the mean squared displacement (MSD) of diffusing particles. Due to direct particle interactions in moderately dilute systems on longer time scales, there occur so-called memory effects. Because of the electrostatic repulsion from other like-charged macroions, particles are deflected from their expected diffusion-path, which results in a smaller value of the MSD. Therefore, generally $D_S^L \leq D_S^S$. The limiting case $D_S^L = D_S^S$ can be observed in charged colloidal dispersions only at very high dilution or strong electrostatic screening. Figure 2.4 shows an example for the typical behaviour of the mean squared displacement over time. At very small times there is a linear increase of the MSD, the slope of which represents D_S^S . At comparably long times there is another region of $\langle r^2 \rangle \propto t$ with a smaller slope, indicating $D_S^L < D_S^S$. At intermediate times a sub-diffusive region can be recognised, that is caused by memory effects due to particle interactions [74].

Löwen and co-workers found, that the ratio D_S^L/D_S^S can serve as a dynamical criterion for the freezing transition in charged colloidal liquids [75] and they could show, that on the freezing line of the investigated systems this ratio has a practically constant value of 0.098, even in the limits of zero and infinite screening of the electrostatic repulsion. Thus the knowledge of the short- and long-time diffusion coefficients exhibits significance for investigations of the phase behaviour of a colloidal dispersion, complementing from a dynamical point of view the Hansen-Verlet criterion [76], which is based on the time-averaged structure.

In less diluted systems, that self-organise to ordered structures, the dynamics of the

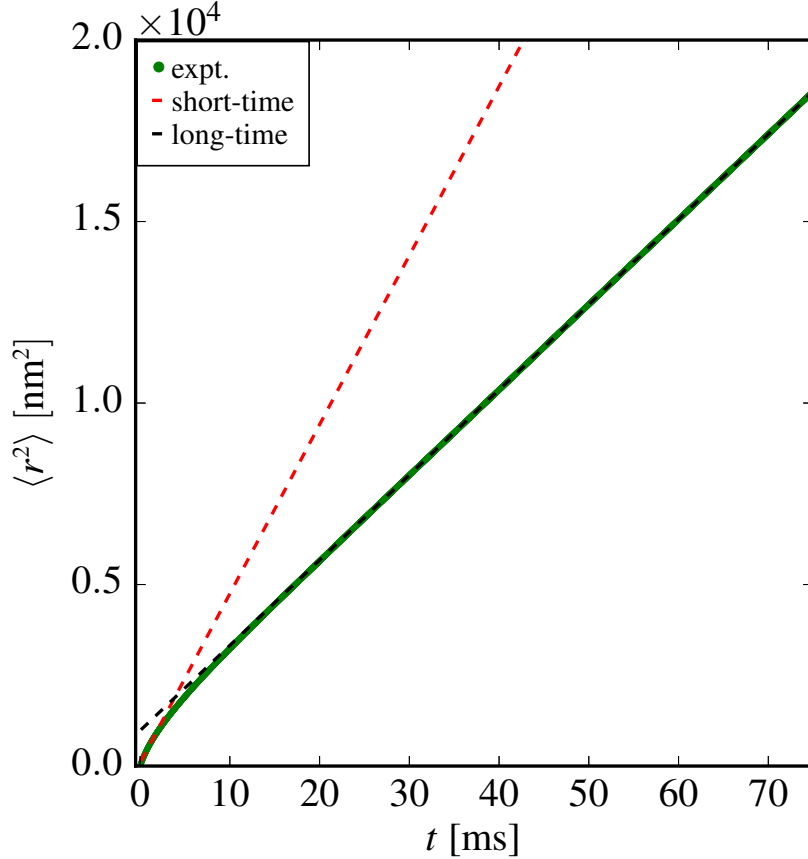


Fig. 2.4: Typical time dependency of the mean squared displacement $\langle r^2 \rangle$ of Brownian particles. The different slopes at very short and long times correspond to a short-time and a long-time self-diffusion coefficient D_S^S and D_S^L , respectively, which generally relate to each other as $D_S^L \leq D_S^S$. In between these limits there is a sub-diffusive region caused by memory effects.

colloidal particles is not only defined by self-diffusion of single particles but by collective diffusion as well. For time increments τ in the range $\tau_B \ll \tau \ll \tau_t$ (cf. (2.19)), the collective short-time or effective diffusion coefficient $D_{\text{eff}}(Q)$

$$D_{\text{eff}}(Q) = \frac{D_0}{S(Q)} \cdot H(Q) \quad (2.21)$$

is related to the self-diffusion coefficient by the static structure factor and a hydrodynamic function $H(Q)$ [77]. $H(Q)$ accounts for indirect, retarded interactions that are mediated by the dispersion medium and can accelerate or decelerate collective particle motion [78]. Eq. (2.21) is also called extended de Gennes relation. Assuming the absence of hydrodynamic interactions with $H(Q) \equiv 1$, it is obvious that $S(Q) = D_0/D_{\text{eff}}(Q)$, which predicts an alternating progression of the structure factor and the effective diffusion coefficient. Thus it can be concluded, that for particularly stable configurations, given by local maxima in $S(Q)$, a deceleration of $D_{\text{eff}}(Q)$ in relation to D_0 and, for more unstable configurations with minima in $S(Q)$, an accelerated collective diffusion is to be expected.

A typical example for this behaviour is displayed in Fig. 2.5.

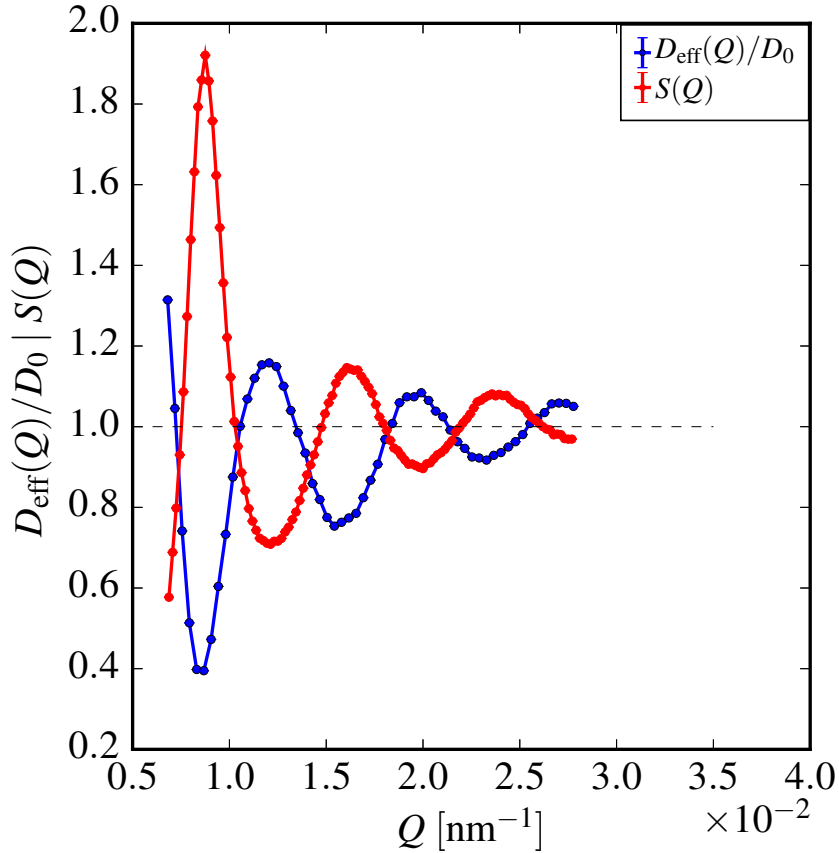


Fig. 2.5: Typical structure factor $S(Q)$ of a liquid-like ordered colloidal dispersion of charged particles and the corresponding collective short-time diffusion coefficient normalised to the self-diffusion coefficient $D_{\text{eff}}(Q)/D_0$. Maxima in $S(Q)$ indicate preferred, more stable configurations leading to a slowed down particle motion, while more unstable configurations marked by minima in $S(Q)$ are not favoured, which causes a faster collective motion on length scales $d \approx 2\pi/Q$.

From (2.21) it is apparent, that the hydrodynamic function of a given system is accessible, if $D_{\text{eff}}(Q)$, D_0 and $S(Q)$ are known, e. g., from static and dynamic light scattering experiments. Any deviations between $S(Q, 0) = D_0/D_{\text{eff}}(Q)$, which is called the short-time limit of the dynamic structure factor or intermediate scattering function, and the static structure factor indicate the presence of hydrodynamic interactions between the observed particles. A quantification is possible via $H(Q) = S(Q) \cdot D_{\text{eff}}(Q)/D_0$.

A more fundamental definition of the hydrodynamic function is given by [79, 80]

$$H(\mathbf{Q}) = \frac{1}{ND_0} \sum_{i,j=1}^N \left(\hat{\mathbf{Q}} \cdot \mathbf{D}_{ij}(\mathbf{r}^N) \cdot \hat{\mathbf{Q}} \exp(i\mathbf{Q}[\mathbf{r}_i - \mathbf{r}_j]) \right), \quad (2.22)$$

where N denotes the number of particles in the system and $\hat{\mathbf{Q}}$ is the unit scattering vector. $\mathbf{r}^N = \{\mathbf{r}_1, \dots, \mathbf{r}_N\}$ are the position vectors of the particle centres and $\mathbf{D}_{ij}(\mathbf{r}^N)$

designate diffusion tensors that describe interdiffusion among particles i and j . There is no exact solution to eq. (2.22) due to the complexity of $\mathbf{D}_{ij}(\mathbf{r}^N)$ for many-particle systems. In case of rather dilute, charge-stabilised colloidal dispersions, utilising the Rotne-Prager approximation [81] for the diffusion tensor, a pairwise additive approach enables calculations in good agreement to experimental findings [78]. The hydrodynamic function is then approximated as

$$H(Q^*) = 1 - 15\varphi \frac{j_1(Q^*)}{Q^*} + 18\varphi \int_1^\infty \frac{r}{\sigma} \left[g^{(2)}\left(\frac{r}{\sigma}\right) - 1 \right] \left[j_0(Qr) - \frac{j_1(Qr)}{Qr} + \frac{j_2(Qr)\sigma^2}{6r^2} \right] d\left(\frac{r}{\sigma}\right), \quad (2.23)$$

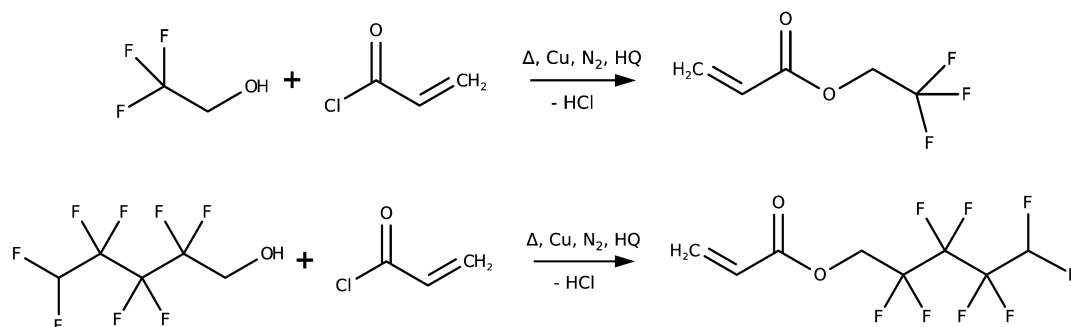
where $Q^* = Q\sigma$ with the particle diameter σ , φ is the particle volume fraction, j_n denotes the spherical Bessel function of n -th order and $g^{(2)}(r/\sigma)$ designates the pair distribution function in dependence on the reduced distance r/σ .

For concentrated dispersions a pairwise additive description does no longer suffice to calculate hydrodynamic interactions between charged particles in a colloidal dispersion correctly. Beenakker and Mazur formulated a many-body approximation that takes into account the hydrodynamic interactions between more than two particles in terms of so-called renormalised connectors [82]. This method, also denoted as $\delta\gamma$ -expansion, is proven useful for predicting the hydrodynamic interactions influencing diffusive motion of charged particles in more concentrated dispersions [83]. A more detailed treatment of this field, however, is relinquished here, as hydrodynamic interactions are not comprised within the scope of this work.

3 Methods

3.1 Monomer preparation

The fluorinated alcohols, 2,2,2-trifluoroethanol (TFE) and 1H,1H,5H-octafluoropentanol (OFP), are esterified following a modification of the Schotten-Baumann reaction [84, 85]. Therein the respective alcohol is brought to reaction with one and a half times the amount of acryloyl chloride (AC) by heating to reflux. 1 g copper powder and 1 g hydroquinone (HQ) are added and a steady nitrogen flux is maintained, as described in the literature [14, 86], yielding the corresponding acrylate esters 2,2,2-trifluoroethyl acrylate (TFEA) and 1H,1H,5H-octafluoropentyl acrylate (OFPA). The reaction equations are displayed in scheme 3.1. Copper (Cu) serves as a catalyst, nitrogen (N₂) supersedes the air-oxygen to prevent polymerisation and HQ inhibits a thermally induced polymerisation during esterification.



Scheme 3.1: Modified Schotten-Baumann reactions of 2,2,2-trifluoroethanol (above) and 1H,1H,5H-octafluoropentanol (below) with acryloyl chloride in the presence of a copper catalyst. By separation of hydrochloric acid the corresponding alkyl acrylates are formed. The presence of nitrogen and hydroquinone prevents unintended polymerisation during esterification.

After four hours the reaction is completed and the desired product is obtained via fractional distillation, in case of OFPA applying reduced pressure. The ester is purified by extracting remaining hydrochloric acid (HCl) and AC with diluted ammonia (NH₃) solution (pH = 9) and is dried afterwards over sodium sulfate (Na₂SO₄). The identity of TFEA and OFPA is verified via ¹H, ¹³C and ¹⁹F nuclear magnetic resonance (NMR) experiments by comparison with literature data [87].

3.2 Emulsion polymerisation

Heterophase polymerisation methods are widely used in the preparation of synthetic colloidal dispersions [30]. One popular example is the emulsion polymerisation technique [88, 89], that has been employed for the preparation of colloidal model systems in this

work. Therein, generally, two immiscible liquid components are emulsified, followed by radical polymerisation of one component. The resulting polymer particles are growing while being dispersed in the continuous second component, eventually forming the desired colloidal dispersion. Many modifications regarding the method of emulsification and the way of initiating the radical polymerisation have been developed, optimising the preparation process for the specific monomer mixture or desired properties of colloids. Numerous descriptions and mechanistic investigations of these are published elsewhere but comprehensive compilations can be found in references [88, 89].

In this work, highly fluorinated, monodisperse, charged polymer colloids are obtained from the self-prepared monomers TFEA, OFPA and commercially available n-butyl acrylate (BA), which are immiscible with water. The employed emulsion polymerisation is well-established for similar monomer systems throughout literature [90–92]. The respective acrylate monomer or monomer mixture is emulsified in water by vigorous stirring, heating to the reaction temperature of 70 °C, which is maintained throughout the whole reaction. A N₂-atmosphere is generated inside the reaction vessel to prevent an uncontrolled polymerisation initiated by the radical character of oxygen molecules from air. Subsequently, a redox catalyst system consisting of sodium sulfite (Na₂SO₃) and ammonium iron(II) sulfate ((NH₄)₂Fe(SO₄)₂) is added. Finally, the addition of potassium persulfate (K₂S₂O₈), by thermolytic radical cleavage of the persulfate anion promoted by the redox catalyst, initiates the radical polymerisation that is typically finished within 12 h. The purified colloidal dispersion is obtained after filtration and dialysis against water for at least one week.

3.3 Determination of the particle refractive index

The total scattered intensity I_t of an illuminated sample can be expressed via the scattering invariant

$$I_t = 4\pi \int_0^{Q'} I(Q)Q^2 dQ, \quad (3.1)$$

which is the integral of the scattered intensity over the entire accessible reciprocal space. This quantity is independent of the particle shape, but solely related to the product of the total squared volume of scatterers and their scattering length density. The scattering length density of suspended, homogeneous particles in light scattering experiments is proportional to the squared difference of the refractive index n_p of the particle and n_m of the dispersion medium. Independent of the scattering vector Q , the proportionality

$$I_{sc} \propto (n_p - n_m)^2 \quad (3.2)$$

holds for the scattered intensity I_{sc} . In a transmission experiment, the intensity of transmitted light is attenuated both, by absorption from the particles and the medium, and by the intensity scattered to the entire solid angle 4π , except the forward scattering at $Q \rightarrow 0$. The latter contribution can be neglected using a sufficiently small aperture. The attenuation due to scattering according to (3.1) and (3.2) is proportional to the squared

difference of the refractive indices n_p and n_m . At the optical matching point $n_p = n_m$ with vanishing scattering invariant, a maximum transmitted intensity is reached.

To deduce the refractive index of suspended particles, the transmission of colloidal dispersions is determined in dependence on the refractive index of the suspending medium employing a standard UV/VIS spectrometer (Lambda 25, Perkin Elmer). The refractive index of the dispersion medium is tuned by changing the composition of water/glycerol mixtures. Starting with a defined volume of a colloidal dispersion and the same volume of water as a reference, equal amounts of glycerol are added to the colloid and the reference. In addition to the altered scattering power, the influence of dilution has to be considered. The transmission is defined as

$$T = \frac{I}{I_0} = \frac{I_0 - {}^1\varrho(I_{\text{abs}} + I_{\text{sc}})}{I_0} = 1 - \frac{{}^1\varrho(I_{\text{abs}} + I_{\text{sc}})}{I_0}, \quad (3.3)$$

where I_0 is the incident intensity and I the transmitted intensity. The latter quantity is attenuated by the absorption of the colloidal particles, I_{abs} , and the light scattered by the colloidal particles, I_{sc} . Changes of the absorption related to the composition of the suspending medium are eliminated by the reference with identical water/glycerol ratio. Absorption and scattering related to the dispersed particles both are proportional to their number density ${}^1\varrho$. Hence the complement $1 - T$ of the transmission normalised to the number density ${}^1\varrho$ is proportional to the sum of absorption and scattering of the colloidal particles

$$\frac{1 - T}{{}^1\varrho} = \frac{I_{\text{abs}}}{I_0} + \frac{I_{\text{sc}}}{I_0} = \frac{I_{\text{abs}}}{I_0} + (n_p - n_m)^2 \frac{I_t}{I_0}, \quad (3.4)$$

which has the functional form of a parabola with its vertex at the optical matching point. Employing the relation

$${}^1\varrho = \frac{V_0}{V_0 + \sum_i V_i} {}^1\varrho_0 \quad (3.5)$$

with V_0 denoting the initial volume of the suspension, V_i the added volumes of glycerol and ${}^1\varrho_0$ the initial number density, the final expression

$$T = 1 - \frac{{}^1\varrho_0}{I_0} \frac{V_0}{V_0 + \sum_i V_i} [I_{\text{abs}} + (n_p - n_m)^2 I_t] \quad (3.6)$$

for the parabola is obtained. The particle refractive index can be determined from the minimum of $\Phi(n_m)$, the relative attenuation $(1 - T(n_m))$ weighted by the ratio of the total volume $V_0 + \sum_i V_i$ to the initial volume V_0 , in dependence on the refractive index n_m of the dispersion medium.

$$\Phi(n_m) = (1 - T(n_m)) \frac{V_0 + \sum_i V_i}{V_0} = \frac{{}^1\varrho_0}{I_0} [I_{\text{abs}} + (n_p - n_m)^2 I_t] \quad (3.7)$$

The refractive indices of water/glycerol mixtures are given in dependence on the mass ratio of both components by an interpolation of literature data [93].

3.4 Light scattering experiments

All light scattering experiments in this work are performed with a CGS-3 goniometer, manufactured by ALV (Langen, Germany). A scheme of the homodyne setup is presented in figure 3.1 (redrawn with permission from [94]).

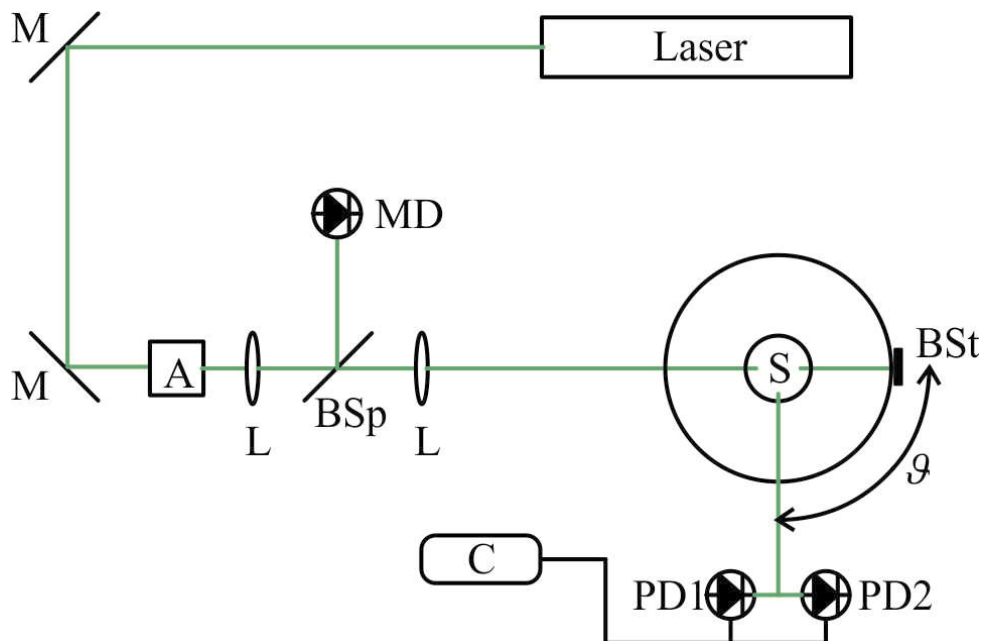


Fig. 3.1: Schematic representation of the homodyne setup employed for light scattering experiments in this work (redrawn with permission from [94]). A detailed description is given in the text.

Coherent, monochromatic ($\lambda_L = 532$ nm) light is emitted by a frequency-doubled Nd:YAG laser with a power of 50 mW. By a system of mirrors (M) and lenses (L), the light is directed to a vat consisting of silica glass. A silica glass cuvette, containing the sample (S), is inserted into the vat, which is filled with toluene and coupled to an external thermostat to maintain a constant temperature throughout the experiment. All light scattering experiments in this work are performed at 293 K. The refractive index of toluene is close to that of silica glass, such that reflections at the interfaces are minimised. The intensity of the primary laser beam is quantified by a monitor diode (MD), utilising a beam splitter (BSp), and is adjusted by an attenuator (A). The non-scattered part of the primary beam is annihilated by a beam stop (BSt). The scattered light, detected at a scattering angle ϑ , is guided by a single-mode fibre and a fibre-optical beam splitter to two Avalanche photo diodes (PD), the signal of which is pseudo-cross correlated to intensity autocorrelation functions, utilising an ALV/LSE-5004 multiple τ digital correlator.

3.4.1 Determination of the particle size

Particle sizes are determined from diluted samples by means of DLS [91]. To screen electrostatic interactions, an ionic strength of $I = 10^{-3}$ mol L⁻¹ is adjusted by addition

of potassium chloride, KCl. The scattered light intensities are detected at an angle of $\vartheta = 90^\circ$ for 900 s each. The particle size distributions are then computed using the CONTIN algorithm proposed by Provencher [71, 72]. The size distributions are therein derived from the distributions of relaxation rates Γ (cf. 2.3.2), which are connected to the diffusion coefficients via (2.16), employing the Stokes-Einstein relation (2.17), under the assumption of non-interacting particles.

To verify the absence of particle interactions, the dependence of the relaxation rate $\Gamma(Q)$ on the scattering vector is investigated by means of DLS. For that, scattering intensities are detected at 64 equidistant Q in the angular range $25^\circ \leq \vartheta \leq 150^\circ$ for 900 s each, using the identical samples as for particle size determination. Digital correlation of $I(Q, t)$ leads to $g_2(Q, \tau)$, which for the observed samples can be simply transformed into $g_1(Q, \tau)$ via the Siegert equation (2.14). The relaxation rate $\Gamma(Q)$ can be determined from the initial slope of the field autocorrelation function

$$\lim_{\tau \rightarrow "0"} -\frac{\partial \ln g_1(Q, \tau)}{\partial \tau} = \Gamma(Q) = D_0 Q^2, \quad (3.8)$$

where $\tau \rightarrow "0"$ denotes time differences larger than the momentum relaxation time but significantly smaller than the structural relaxation time [74] (cf. 2.3.2). If particle interactions are not present, $\Gamma(Q)$ obeys the Landau-Placzek relation (2.16) indicated by a linear dependence on Q^2 . This behaviour is exemplified by figure 3.2.

Colloidal particles of dispersions prepared by means of emulsion polymerisation are not entirely uniform but exhibit a size distribution. The non-uniformity of colloidal particles is usually quantified via the polydispersity p or the polydispersity index ($\text{PDI} = p^2$). It is the author's choice to use this designation throughout this work as it is commonly known from literature. However, it should be mentioned that IUPAC [95] has recommended the exchange of the term "polydispersity" with "dispersity" due to intrinsic redundancy of the former.

In terms of the molecular weight distribution of polymer coils, the Schulz-Flory distribution describes the probability of existence of polymer coils of a defined size [96, 97]. This definition can be transferred onto the distribution of colloidal particles consisting of polymer chains [90, 98], as the particles prepared in this work. The function

$$c(R) = \frac{1}{\Gamma(Z+1)} \left(\frac{Z+1}{R_0} \right)^{Z+1} \cdot R^Z \cdot \exp \left(-\frac{Z+1}{R_0} R \right) \quad (3.9)$$

gives a mathematical description of the probability density of the colloidal particle sizes, where R is a given particle radius, R_0 denotes the mean particle radius and Z is a parameter quantifying the distribution width. The transcendent Γ -function for positive arguments represents a generalised factorial: $\Gamma(N+1) = N!$ for integer N . The polydispersity is defined as the relative variance of the distribution and relates to Z via [98]

$$p = \sqrt{\frac{\langle R^2 \rangle}{\langle R \rangle^2} - 1} = \sqrt{\frac{1}{Z+1}}. \quad (3.10)$$

In this way, a Schulz-Flory approximation to the particle size distribution of a colloidal dispersion obtained by DLS can be employed to determine the non-uniformity of the

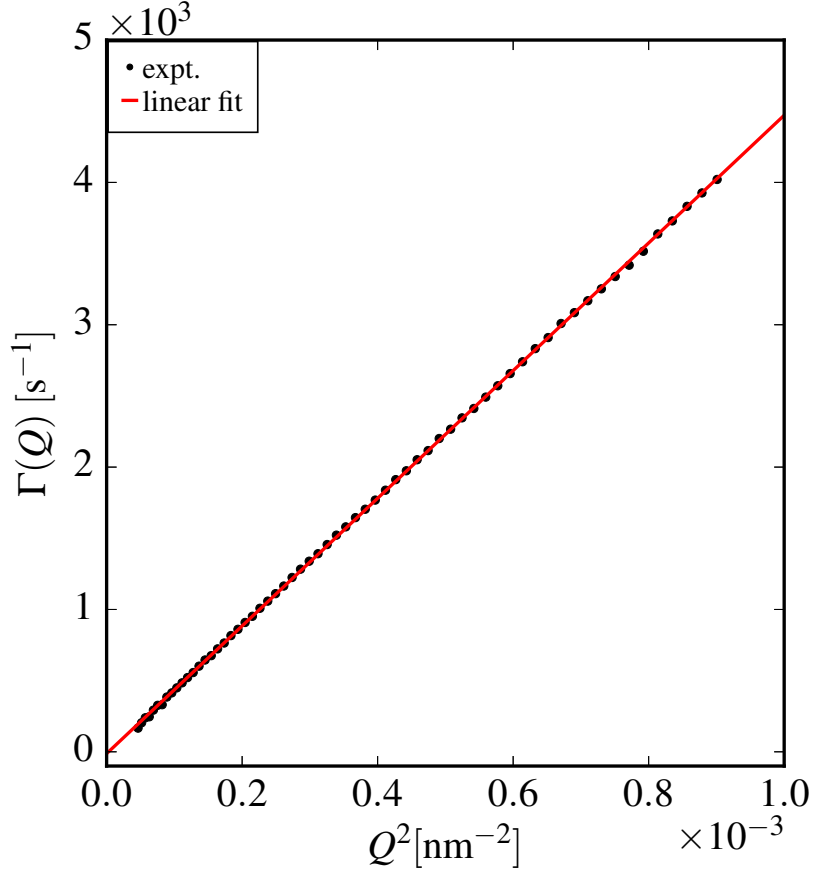


Fig. 3.2: Linear dependence of the relaxation rate $\Gamma(Q)$ on Q^2 for non-interacting spherical particles. According to the Landau-Placzek relation $\Gamma(Q) = D_E Q^2$ the slope of the straight line defines the Einstein diffusion coefficient D_E of the observed particles.

prepared colloidal polymer particles [90].

3.4.2 Determination of the static structure factor

To characterise the self-organisation of less diluted systems to liquid-like ordered systems, the structure factor $S(Q)$ is determined employing SLS [99]. A mixed-bed ion exchanger [Amberlite[®] MB-6113, Merck KGaA] is added to suspensions to remove stray ions in order to maximise the Debye screening length λ_D . Employing the afore mentioned ALV setup (cf. section 3.4) the scattered intensity is detected in the range $25^\circ \leq \vartheta \leq 150^\circ$ at 128 equidistant Q for 60 s each. To access an ensemble average in short time, the sample cell is continuously rotated during the static light scattering experiment. The particle form factor $P(Q)$ is determined in an identical experiment using a dilute suspension (cf. 2.3.1), prepared as described in section 3.4.1. According to (2.7) the structure factor $S(Q)$ is obtained by normalising the average scattered intensity of an ordered system to $P(Q)$. A graphical example for this is shown in figure 3.3.

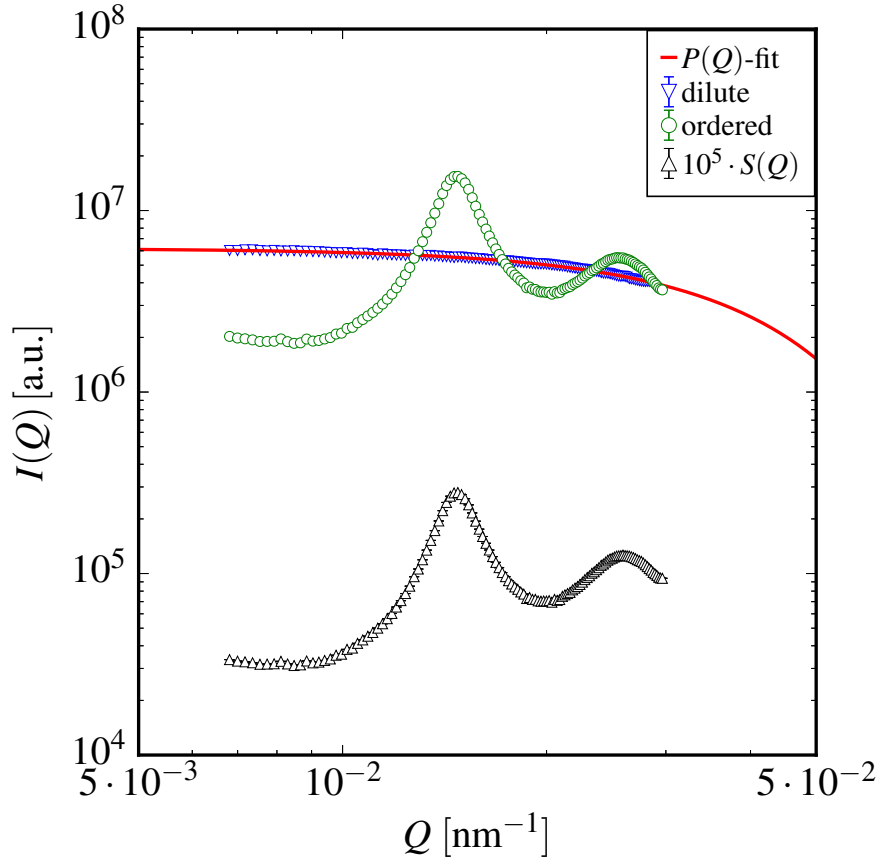


Fig. 3.3: Illustration of the experimental determination of the static structure factor $S(Q)$ by static light scattering. The scattering function of an ordered sample is normalised to the form factor $P(Q)$, obtained by a fit to the scattering function of a dilute, disordered sample resulting from a separate light scattering experiment. Simultaneously normalising the scattering functions to the number densities of the corresponding samples, leads to $S(Q)$, here multiplied by 10^5 for reasons of display.

3.4.3 Investigation of collective diffusion

The collective diffusion of less diluted, ordered colloidal dispersions is investigated by means of DLS. To investigate structure-dynamics relations of identical ensembles, DLS experiments are conducted directly subsequent to the corresponding SLS experiments (cf. 3.4.2) with the identical samples and cuvette position. In the range $25^\circ \leq \vartheta \leq 150^\circ$ at 64 equidistant Q the scattered intensity is detected for 900 s each. The cuvette is stationary during DLS experiments. The evaluation of the fluctuations of the scattered intensity is performed according to section 2.3.2, such that via (3.8) in analogy to the self-diffusion coefficient for diluted systems, $D_{\text{eff}}(Q)$ can be determined for interacting systems. For liquid-like ordered colloidal systems the collective short-time diffusion coefficient shows a damped oscillation with increasing Q , as described at the end of section 2.3.2.

3.5 Brownian Dynamics simulations

The Brownian Dynamics (BD) simulations of colloidal dispersions in this work are performed according to the Ermak algorithm described by equation (2.5). A new position vector of the simulated, charged particle is computed in dependence on its previous position, an electrostatic force resulting from the surface charges of the particles and on a random displacement according to Brownian motion. Thus, hydrodynamic interactions mediated by the molecules of the continuous phase of the colloidal dispersion are neglected. There are, however, algorithms which include hydrodynamic contributions to particle trajectories employing available approximations of the diffusion tensor \mathbf{D}_{ij} [100]. Due to the numerical demands posed by such algorithms, the inclusion of hydrodynamics is only realisable for small systems.

As a compromise between numerical effort and statistical accuracy systems consisting of several thousand Brownian particles are simulated in this work. To avoid surface effects and maintain comparability to real colloidal dispersions with much larger particle numbers, periodic boundary conditions are employed. Virtually, the simulated, cubic box is 3D-periodically replicated. With respect to the calculated pair potential, a cut-off radius $R_c = L/2$ is defined, by which only particle interdistances of half the cubic box length L or less are considered [60]. In general, simulations are initiated employing cubic crystalline start configurations (fcc or bcc) and performed until equilibrium, which is identified when the pair distribution functions $g^{(2)}(r)$ of several subsequent time steps do not differ. The time step size for the BD simulations in this work is adjusted to $\Delta t = 2 \times 10^{-6}$ s, where for shorter simulations every 10th and for longer simulations every 100th step the coordinates of particles are saved to data files for subsequent analysis of trajectories. Thus, the temporal resolution is reduced by the corresponding factor. Unless otherwise stated, in this work standard values are employed in simulations for the temperature $T = 293.15$ K, the dynamic viscosity $\eta = 1.002 \times 10^{-3}$ Pa · s, and relative permittivity $\epsilon_r = 78.3$ of an aqueous dispersion medium.

Since the Fourier equivalent $S(Q)$ of the pair distribution function is accessible via light scattering experiments, the simulated $g^{(2)}(r)$ is transformed into a structure factor, if BD simulation and scattering experiment are compared. This is performed by means of a Fourier-Bessel transform, as shown in equation (2.9). To avoid artefacts at small Q due to truncation effects, a least-squares fit of an heuristic, damped oscillating function [16, 101]

$$f(r) = 1 + A_1 \exp(A_2(r - A_3)) \cos(A_4(r - A_3)) \quad (3.11)$$

is performed to extrapolate the simulated data to distances $r > R_c$ with the parameters $A_1 \cdots A_4$. This procedure is exemplified by figure 3.4 for a typical equilibrium pair distribution function of a liquid-like ordered colloid.

The coordinates of a particle after each simulation step define this particle's simulated trajectory of diffusion. Knowing the position vectors of each particle at each time step the self-dynamic observable in terms of the mean squared displacement (MSD) $\langle r^2 \rangle$ is accessible (cf. eq. (2.4) and section 2.3.2). The time dependency of the self-diffusion coefficient $D_S(t)$ is thus obtainable via a Verlet algorithm [102, 103]

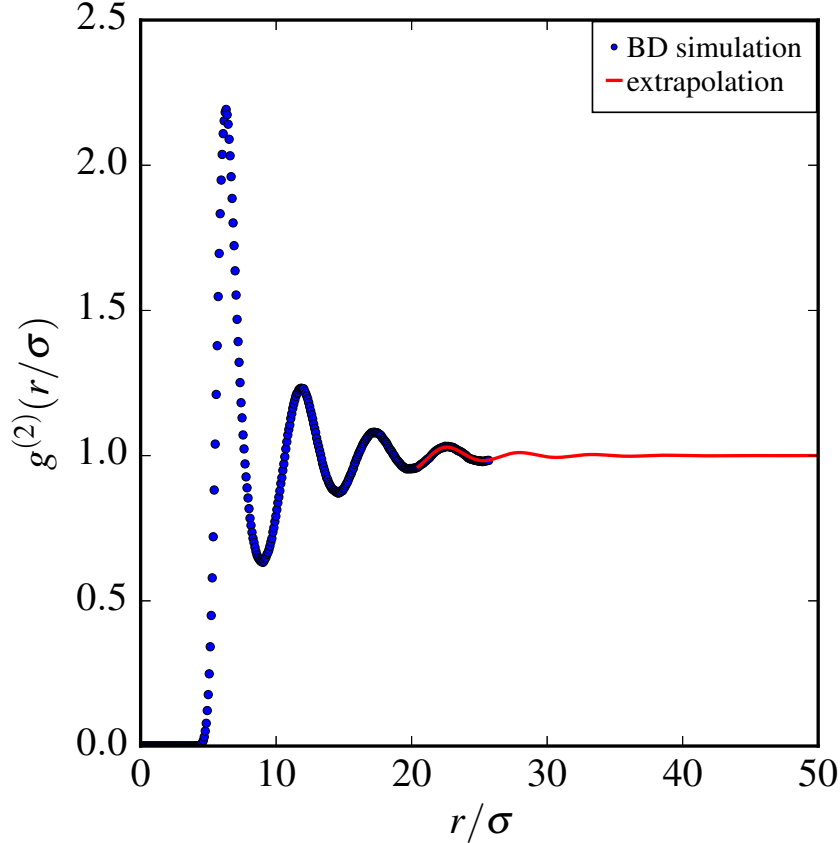


Fig. 3.4: The pair distribution function $g^{(2)}(r/\sigma)$, in dependence on the normalised distance r/σ with the particle diameter σ , as gained by BD simulations, is restricted to $r = R_c$. $g^{(2)}(r/\sigma)$ is extrapolated by a damped oscillating function according to (3.11) fit to the simulated data. Hereby artefacts due to truncation effects after Fourier-Bessel transform to obtain the static structure factor $S(Q\sigma)$ are avoided.

$$D_S(t) = \frac{\langle r^2 \rangle(t + \Delta t) - \langle r^2 \rangle(t - \Delta t)}{2\Delta t}, \quad (3.12)$$

which is employed in this work for investigations of tracer particle dynamics in mixtures.

Beyond self-dynamics, the knowledge of the particle trajectories also allows for the determination of collective diffusion phenomena in simulations of more concentrated mixtures of colloidal dispersions. During this work a sophisticated algorithm has been developed, that correlates the positions of two different particles at each simulated time step. Via this computationally demanding approach the partial, distinct space-time pair distribution functions $g_{ij}^{(2)}(r, t)$ are determined for correlations between different particles of the same particle class and different particle classes. Spatial Fourier-Bessel transforms (cf. eq. (2.9)) of the $g_{ij}^{(2)}(r, t)$ result in the partial intermediate scattering functions $S_{ij}(Q, t)$, which comprise the collective diffusion behaviour in concentrated mixtures of colloidal dispersions.

In the following, further details of BD simulations performed in this work are compiled.

3.5.1 Simulation of homo-colloidal systems

Homo-colloidal systems, consisting of one particle species, are simulated to clarify the numbers of effective surface charges Z_{eff} of the prepared colloidal particles. As described in section 2.3.1, RMSA evaluation of SLS data overestimates Z_{eff} . By adjusting the number of charges in BD simulations until the resulting simulated structure factor well agrees with the corresponding experimental $S(Q)$, a more realistic value of Z_{eff} is determined. The particle size and number density are set according to previous DLS experiments and RMSA evaluation of SLS data. In this kind of simulation, 2048 particles of the respective colloid are modelled starting at a fcc crystalline configuration until the structural equilibrium is reached.

3.5.2 Simulation of binary mixtures

BD simulations of binary colloidal mixtures are performed in this work, in particular for the comparison with light scattering results. The main focus is directed onto dynamical properties in terms of the self-diffusion coefficient of tracer particles in a homo-colloidal matrix and the collective dynamics in mixtures with similar number densities of both components. The results of previous characterisation of the prepared colloidal dispersions by means of light scattering serve as input parameters, such as particle size and number density. The numbers of effective charges are set according to the findings from simulations of homo-colloidal systems. Parameters characterising the dispersion medium, such as the dynamic viscosity η and the relative permittivity ϵ_r , are adjusted to the corresponding experimental medium. For better statistical accuracy, in these simulations 8192 particles are simulated starting from a bcc lattice until equilibrium. Subsequently, a longer simulation run is performed to investigate dynamic properties. In case of diluted tracer particles the dynamics over 200 ms is simulated. For the collective diffusion of real binary mixtures in more viscous dispersion media, runs over simulated times up to 1.2 s are performed.

3.5.3 Simulation of ternary mixtures

Mixtures of three dispersed species, i. e., one tracer component in a matrix consisting of two colloidal species, are simulated in this work detached from experimental systems. Particles, medium and potential parameters in these simulations are adjusted as to describe a realistic aqueous system. The mixtures are simulated with 8192 particles starting from a bcc lattice. After reaching the equilibrium, dynamic runs of simulated times of 200 ms are performed. Particle sizes, surface charges, ionic strength of the dispersion medium and particle number density are systematically varied in relation to a fixed reference system. The parameters of the three components of this reference system are compiled in table 3.1. The total particle number density is set to ${}^1\rho_{\text{total}} = 5.0 \mu\text{m}^{-3}$.

Table 3.1: Particle diameters σ , relative number densities ${}^1\rho_i/{}^1\rho_{\text{total}}$, and surface charges Z_{eff} defined for the reference system in BD simulations of ternary mixtures.

Component	σ [nm]	${}^1\rho_i/{}^1\rho_{\text{total}}$	Z_{eff}
Tracer	100	0.050	200
Matrix A	100	0.475	200
Matrix B	100	0.475	200

4 Preparation and characterisation of colloidal model systems

4.1 Synthesis of fluorinated alkyl acrylates

The fluorinated alkyl acrylates TFEA and OFPA are synthesised as precursors for the preparation of fluorinated polymer colloid dispersions, following the instructions described in section 3.1. The purified monomers are obtained with yields of 56 % and 76 % for TFEA and OFPA, respectively. The spectra obtained from ^1H , $^{13}\text{C}\{^1\text{H}\}$ and $^{19}\text{F}\{^1\text{H}\}$ NMR experiments for identification of the desired products are attached in appendix A. Comparison with literature data of Boutevin et al. [87] and database entries of the Spectral Database of Organic Compounds (SDBS) organised by the National Institute of Advanced Industrial Science and Technology (AIST), Japan, accessed on November 24 2016 [104, 105], verifies the identity of the fluorinated monomers.

4.2 Preparation of colloidal polymer particles

Colloidal model systems are prepared from BA, TFEA and OFPA via emulsion polymerisation as described in section 3.2. Homopolymer colloids of OFPA and BA have been synthesised and well-characterised before [16, 90, 106]. TFEA is a well-known component in the preparation of copolymer colloids [107], while polymers consisting solely of this fluorinated acrylate have not been studied extensively before. In this work, beyond the homopolymers poly(2,2,2-trifluoroethyl acrylate) (pTFEA) and poly(1H,1H,5H-octafluoropentyl acrylate) (pOFPA), mixtures of TFEA and BA as well as TFEA and OFPA in different compositions are copolymerised to result in novel classes of highly defined colloidal copolymer dispersions. These are designated as poly(TFEA-co-BA) (pTcB) and poly(TFEA-co-OFPA) (pTcO), respectively. All 36 colloids, that are prepared in this work, are summarised in table 4.1, where also the amounts of water, monomer(s), catalysts and radical initiator chosen for the preparation of the respective system are compiled. The designation of the copolymer systems follows the scheme pAcB- xx , where A and B denote the two monomers employed in the copolymerisation and xx is the percentage molar ratio of B in the monomer mixture. The indication of the amount of monomer n_{Mono} for the copolymer systems follows $(n_{\text{A}} + n_{\text{B}})$.

Table 4.1: Compilation of the quantities of monomers, radical initiator, $K_2S_2O_8$, and redox catalyst system of $Na_2SO_3/(NH_4)_2Fe(SO_4)_2$ as well as topological parameters of the resulting colloidal polymer particles. The two digits in the copolymer sample names indicate the molar ratio of BA in the monomer mixture in percent. The molar quantities n_{mono} for the copolymers are displayed as $n_{\text{TFEA}} + n_i$, with i denoting BA or OFPA, respectively. For monomer amounts indicated by an asterisc, in addition 1 mmol of the crosslinker EGDMA is added to the monomer mixture. The refractive indices n_p are determined at ambient temperature for $\lambda = 532 \text{ nm}$. The Einstein self-diffusion coefficients D_0 are determined in aqueous dispersion containing $10^{-3} \text{ mol L}^{-1} \text{ KCl}$ at $T = 298 \text{ K}$.

Polymer system	ID	V_{H_2O} [mL]	n_{Mono} [mmol]	$m_{Na_2SO_3}$ [mg]	$m_{(NH_4)_2Fe(SO_4)_2}$ [mg]	$m_{K_2S_2O_8}$ [mg]	$R_{h,\text{max}}$ [nm]	p	$D_0/10^{-12}$ [m ² s ⁻¹]	n_p
pTFEA	I	250	33	104	3	30	37	0.110	5.64	1.402
	II	250	68	101	1	31	62	0.089	3.57	
	VI	125	25	48	1	16	56	0.180	4.46	
	VII	125	10	105	1	15	22	0.177	10.86	
	VIII	250	86	102	1	30	154	0.041	1.62	
	IX	250	40	101	1	30	67	0.091	3.51	
pOFPA	III	250	25	98	1	30	106	0.091	2.29	1.380
	IV	250	50	98	1	31	140	0.132		
	V	250	38	100	1	30	128	0.051		
pTcB-10	I	250	(45+5)	102	1	30	45	0.088	5.25	1.428
	II	250	(18+2)	101	1	30	35	0.098	7.06	
	III	250	(81+9)	106	1	30	135	0.132	1.80	
	IV	250	(63+7)	98	1	30	105	0.040	2.18	
	V	250	(45+5)	100	1	30	70	0.065	3.45	
	VI	500	(36+4)	200	1	60	55	0.051	4.37	
pTcB-30	I	250	(35+15)	100	1	30	54	0.196	4.39	1.430
	II	250	(34+15)*	101	1	30	50	0.108	4.65	
	III	500	(70+30)	200	1	60	68	0.141	3.54	
	IV	250	(35+15)	100	1	15	53	0.076	4.72	
	V	250	(53+23)	153	1	31	72	0.064	3.36	

pTcB-50	I	250	(25+25)	102	1	32	80	0.055	2.98	1.438
	II	250	(25+24)*	101	1	30	90	0.039	2.49	
	III	500	(50+50)	200	1	61	85	0.045	2.74	1.434
	IV	250	(25+25)	100	1	61	55	0.148	4.35	1.433
	V	250	(38+38)	152	1	46	67	0.217	3.56	1.439
pTcB-70	I	250	(15+35)	102	1	30	55	0.075	4.34	1.444
	II	250	(15+34)*	102	1	31	58	0.084	4.14	1.435
	III	500	(30+70)	200	1	61	53	0.135	4.51	1.445
	IV	250	(15+35)	101	1	16	62	0.073	3.83	1.446
	V	250	(23+53)	151	1	30	76	0.102	3.16	
pTcB-90	I	250	(5+45)	101	1	30	58	0.176	4.31	1.449
	II	250	(8+68)	153	1	30	54	0.141	4.57	
	III	250	(5+45)	100	1	15	67	0.052	3.63	
pTcO-30		250	(21+9)	103	1	31	36	0.090	6.60	
pTcO-50		250	(15+15)	101	1	30	32	0.413		
pTcO-90		250	(3+27)	100	1	30	77	0.169		
Polymer system	ID	$V_{\text{H}_2\text{O}}$ [mL]	n_{Mono} [mmol]	$m_{\text{Na}_2\text{SO}_3}$ [mg]	$m_{(\text{NH}_4)_2\text{Fe}(\text{SO}_4)_2}$ [mg]	$m_{\text{K}_2\text{S}_2\text{O}_8}$ [mg]	$R_{\text{h,max}}$ [nm]	p	$D_0/10^{-12}$ [m ² s ⁻¹]	n_{p}

4.3 Characterisation of particle-specific properties

The prepared (co)polymer colloids are characterised regarding their particle sizes by means of DLS as described in section 3.4.1. Data evaluation employing the CONTIN algorithm results in size distribution functions, exhibiting the probability density $P(R_h)$ of the hydrodynamic particle radii R_h . These experimental data are approximated by a Schulz-Flory distribution according to eq. (3.9), where the resulting parameter Z defines the polydispersity $p = (Z + 1)^{-1/2}$, thus providing a quantitative measure of the uniformity of the prepared colloidal particles (cf. 3.4.1). The distribution maximum represents the most probable hydrodynamic radius $R_{h,\max}$. For nearly symmetric distributions $R_{h,\max}$ coincides with the mean hydrodynamic radius $\langle R_h \rangle$ within experimental accuracy. This equivalence is met for most of the prepared polymer colloids, as is supported by the examples **(a)** to **(d)** of the chosen size distributions compiled in figure 4.1. The determined most probable hydrodynamic radii and polydispersities are presented in table 4.1.

In figure 4.1 size distribution functions of the six systems pTcB-50 III, pTFEA VIII, pTFEA VII, pTcO-90, pTcB-50 V and pTcO-50, consecutively labelled from **(a)** to **(f)**, are displayed as examples for all prepared colloidal dispersions. **(a)**, **(b)**, and **(c)** show very narrow distributions, that are quantified in low polydispersities of 0.045 for pTcB-50 III and 0.041 for pTFEA VIII. pTFEA VII exhibits a larger polydispersity of $p = 0.177$ despite its narrow distribution. It is a well known phenomenon that the polydispersity p increases for decreasing particle diameters, since even small absolute deviations of individual particle sizes from the mean size become progressively important relative to a smaller mean particle diameter. pTFEA VIII exhibits the largest most probable particle sizes with $R_{h,\max} = 154$ nm, whereas pTFEA VII with $R_{h,\max} = 22$ nm represents the system with the smallest particles of the prepared colloids. The size distribution of pTcO-50 III is a typical example for those dispersions with the most frequently appearing particle sizes in the range $50 \text{ nm} \leq R_{h,\max} \leq 100 \text{ nm}$ and low polydispersity. Fig. 4.1 **(d)** displays the size distribution function of pTcO-90 with $p = 0.169$, as an example for those colloidal systems with slightly elevated polydispersity.

Subplot **(e)** shows the most significant example for a skew size distribution function for the systems prepared in this work. The most probable hydrodynamic radius $R_{h,\max} = 67$ nm and the mean hydrodynamic radius $\langle R_h \rangle = 70$ nm differ by more than four percent. However, the majority of the prepared polymer colloids, in particular those investigated in mixtures later in this work, exhibit no difference between $R_{h,\max}$ and $\langle R_h \rangle$ within experimental accuracy.

The last example in Fig. 4.1 **(f)** shows a bimodal size distribution, that gives rise to a polydispersity of $p = 0.413$, due to the existence of particles more than three times the size of the most probable ones. As the capability of self-organisation is not to be expected for this dispersion, pTcO-50 is not further investigated in this work.

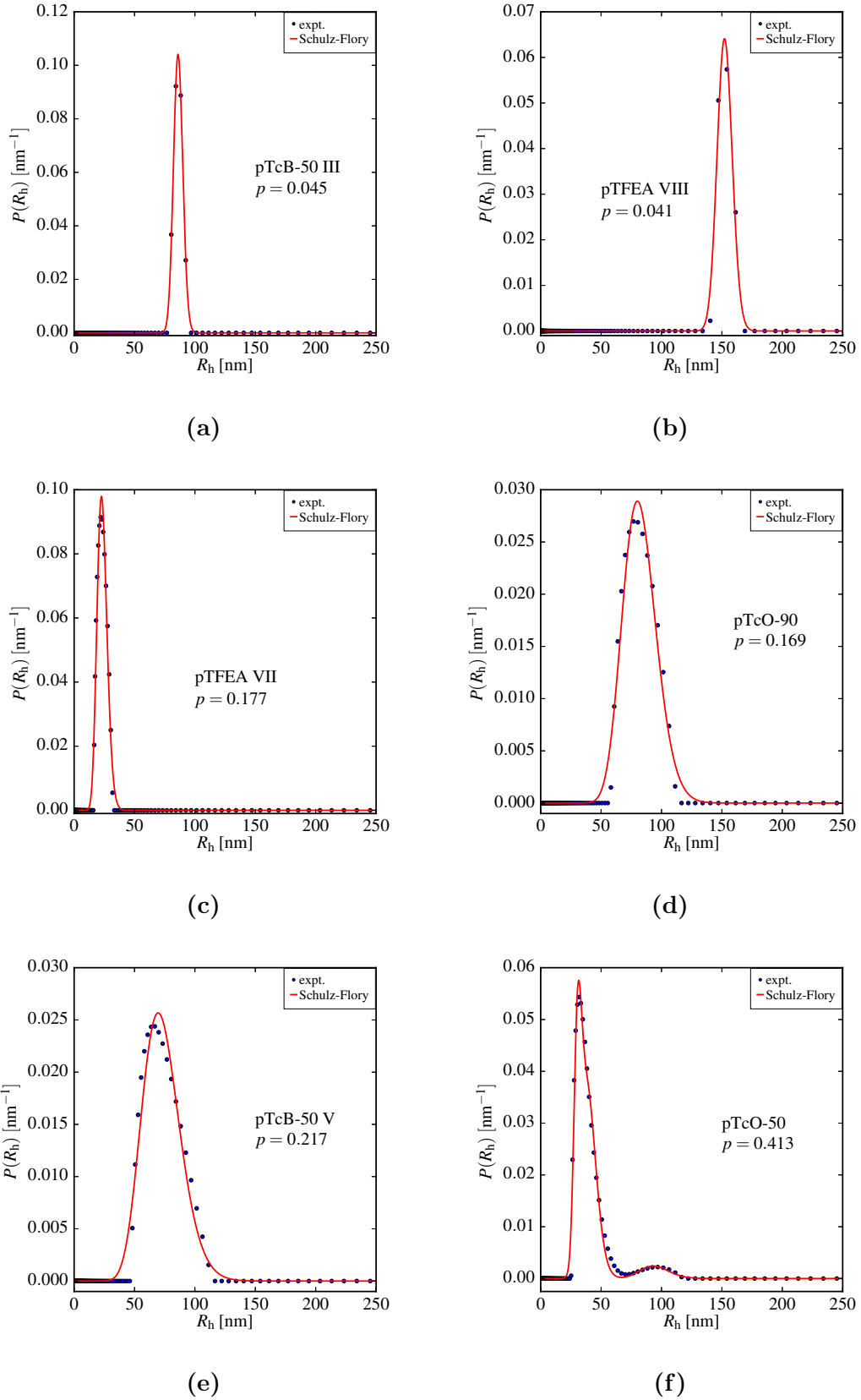


Fig. 4.1: Particle size distributions of six examples of the prepared polymer colloids obtained from DLS data via the CONTIN algorithm. Red curves represent fit functions according to a Schulz-Flory distribution, which are employed for determination of the polydispersity p .

From the initial slopes of field autocorrelation functions $g_1(Q, \tau)$ acquired from angle-dependent DLS experiments with the samples employed for the determination of the size distribution functions (cf. 3.4.1), relaxation rates $\Gamma(Q)$ are obtained. These relaxation rates are proportional to Q^2 indicating a free Gaussian diffusion of non-interacting particles. An example for the system pTFEA II is displayed on the left of Fig. 4.2. This clearly shows, that the dilution and electrostatic screening by stray ions are sufficient to suppress particle interactions, that would lead to non-Gaussian diffusion which would alter the size distribution functions determined using the CONTIN algorithm. The self-diffusion coefficients D_0 obtained from the Q -dependence of the relaxation rates described by the Landau-Placzek relation (2.16) are also compiled in table 4.1. As is displayed on the right of Fig. 4.2, these self-diffusion coefficients show an inversely proportional relation to the most probable hydrodynamic particle radii determined via the CONTIN algorithm, hence meeting the Stokes-Einstein relation (2.17). Slight deviations occur for the more polydisperse samples since only the first cumulant is used to determine the relaxation rates $\Gamma(Q)$, neglecting polydispersity and skewness of the size distribution functions.

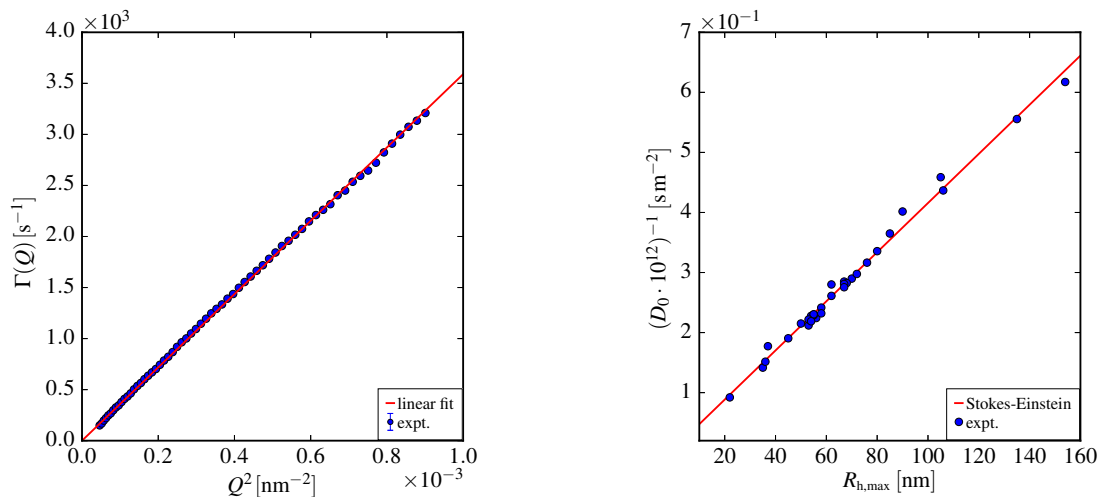


Fig. 4.2: Left: Relaxation rate $\Gamma(Q)$ acquired from initial slopes of $g_1(Q, \tau)$ determined by DLS for the example colloid pTFEA II. The linear dependence of $\Gamma(Q)$ on Q^2 verifies free Gaussian diffusion of the particles. According to (2.16) the slope gives the self-diffusion coefficient D_0 . Right: Illustration of the linear proportionality between D_0^{-1} and the most probable hydrodynamic particle radii $R_{h,\max}$ of the prepared colloids, meeting the Stokes-Einstein equation (2.17).

The particle refractive indices of the prepared colloidal dispersions are obtained by means of transmission experiments employing an UV/VIS spectrometer (cf. section 3.3). The weighted relative attenuation of the transmission $\Phi(n_m)$ (cf. (3.7)) depends on the squared difference $(n_p - n_m)^2$ of the refractive index of the particles, n_p , and the dispersion medium, n_m . Hence, the minimum of a plot of $\Phi(n_m)$ versus n_m indicates the refractive index of the probed colloidal particles with $n_m = n_p$. Figure 4.3 shows such a plot for the example pTcB-50 IV. The refractive index of these particles is determined to $n_p = 1.433$. The remaining attenuation, given by $\Phi(n_m) \approx 0.2$ in the example figure, can be ascribed to absorption processes inside the colloidal particles, which are independent from n_m .

In table 4.1 the obtained refractive indices of the other colloidal particles are compiled. In an ideal case, particles prepared from the same monomers or monomer mixtures with

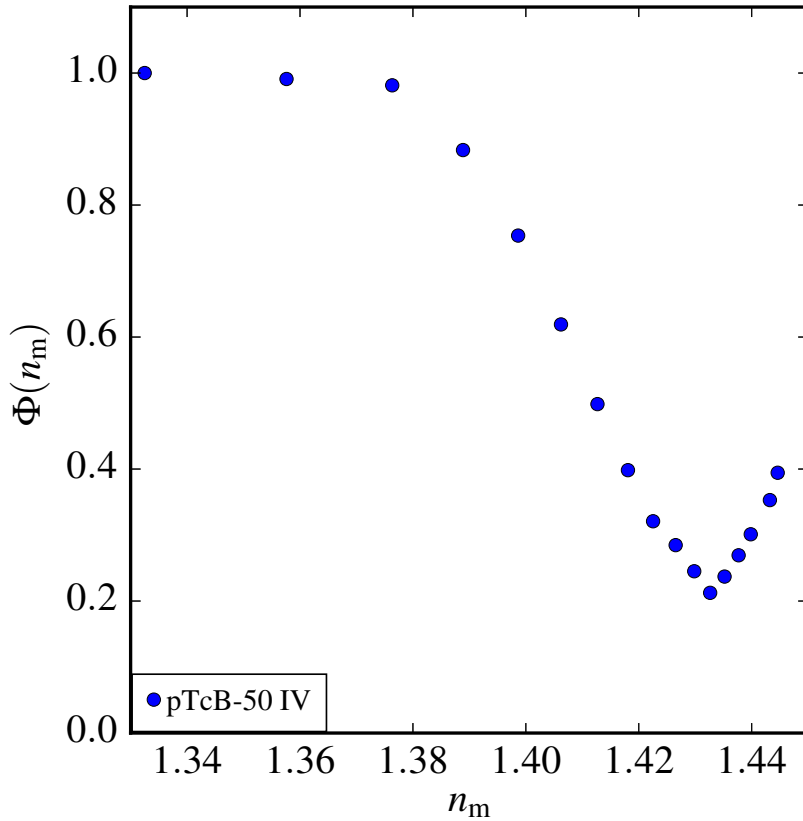


Fig. 4.3: Dependency of the weighted relative attenuation $\Phi(n_m)$ on the refractive index of the dispersion medium n_m , measured for the system pTcB-50 IV in a photometric transmission experiment with a wavelength $\lambda = 532$ nm. The vertex of the expected minimum indicates the index-matching point, where $n_p = n_m$, thus revealing the particle refractive index $n_p = 1.433$.

the same molar compositions should exhibit identical refractive indices. However, as is shown in table 4.1, there are small deviations of less than one percent, e. g., among the refractive indices of the different TFEA-co-BA copolymer particles with 30, 50 and 70 percent ratio of n-butyl acrylate. It can be hypothesised, that these discrepancies originate from deviations in the densities of the polymer chains inside the colloidal particles. A further resolution of this effect is not pursued at this point. Since these deviations among the refractive indices of the particles of the same copolymer systems are marginal, for most of the remaining system groups only one particle refractive index is determined, which serves as a benchmark, e. g., in case of the pTFEA systems.

In figure 4.4 the mean refractive indices $\langle n_p \rangle$ of prepared pTFEA and pTcB particles as well as the known refractive index of poly(n-butyl acrylate) (pBA) particles are displayed in dependence on the molar fraction of BA, x_{BA} , in the corresponding monomer mixtures. Obviously, the refractive index of pTcB copolymer particles relates proportionally to x_{BA} .

However, the homopolymers of the corresponding components significantly deviate from this linear behaviour, resulting in a lower refractive index for pTFEA and a higher one for pBA. The comparison with the refractive indices of water and glycerol in Fig. 4.4

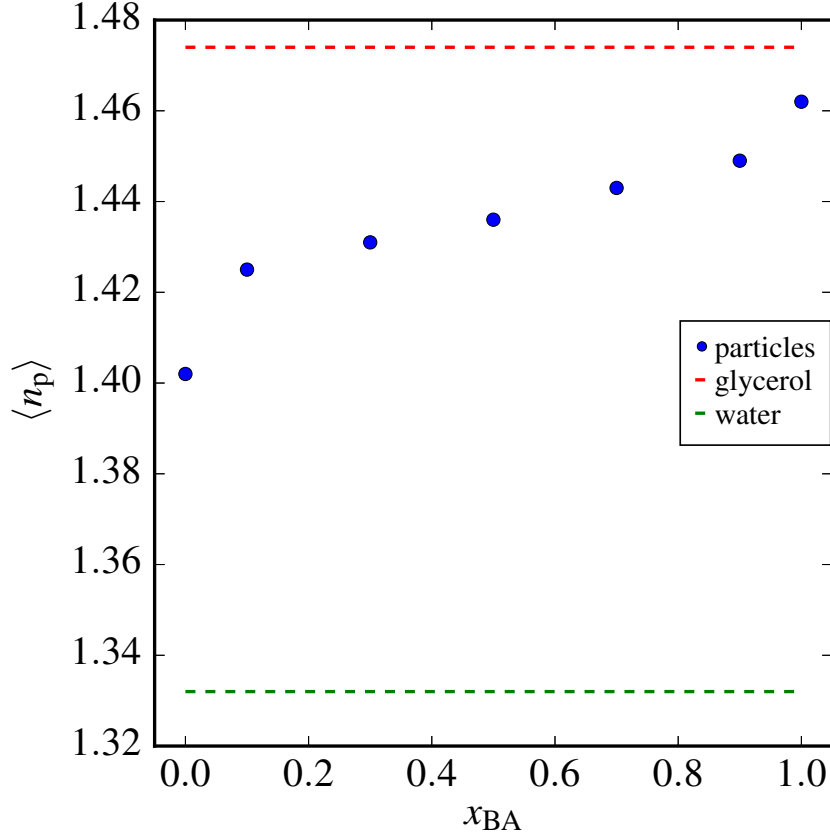


Fig. 4.4: Dependence of the mean refractive index $\langle n_p \rangle$ of pTFEA, pTcB, and pBA particles on the molar fraction of butyl acrylate, x_{BA} , in the corresponding monomer mixture. For copolymers a linear increase of $\langle n_p \rangle$ is observed proportional to x_{BA} . The homopolymers at $x_{BA} = 0$ (pTFEA) and $x_{BA} = 1$ (pBA) somewhat deviate from this linear behaviour. As indicated by dashed lines for refractive indices of water and glycerol, all displayed types of (co)polymer particles can be index-matched in water/glycerol mixtures.

exemplifies the possibility of index-matching any of the prepared colloidal dispersions in mixtures of both substances. Refractive indices of prepared pTcO particles are not explicitly determined in this work. However, the homopolymers pOFPA III and pTFEA VIII exhibit refractive indices of $n_p(\text{pOFPA}) = 1.380$ and $n_p(\text{pTFEA}) = 1.402$. Hence it is a plausible assumption that pTcO copolymers will have refractive indices in the range $1.380 < n_p(\text{pTcO}) < 1.402$.

4.4 Characterisation of self-organised single compound systems

Section 4.3 has provided evidence for the low polydispersities and tunability of refractive indices of the prepared copolymer particles in the range $1.380 \leq n_p \leq 1.449$ for possible particle sizes $22 \text{ nm} \leq R_{h,\text{max}} \leq 154 \text{ nm}$. In this section, liquid-like structures originating from the self-organisation of these colloidal particles are investigated by means of SLS. The evaluation of the resulting structure factors employing the RMSA closure relation for the Ornstein-Zernike equation, complemented by BD simulations in order to replicate experimental systems *in silico*, gives access to characteristic parameters in terms of the particle number density ${}^1\rho$ and the number of effective surface charges Z_{eff} .

Each of the 36 different colloidal dispersions are able to self-organise to ordered structures. However, in the scope of this work, 20 liquid-like samples of 16 different colloidal systems are characterised in order to exhibit the foundation for the investigations of binary and ternary mixtures later in this work. The static structure factors $S(Q)$ of the ordered samples are determined as described in section 3.4.2. For illustration figure 4.5 shows the SLS results for pTcB-70 I, which exhibits a particle refractive index of $n_p = 1.444$. To avoid multiple scattering from the less diluted, ordered sample, the refractive index of the dispersion medium is increased to $n_m = 1.381$ by addition of glycerol.

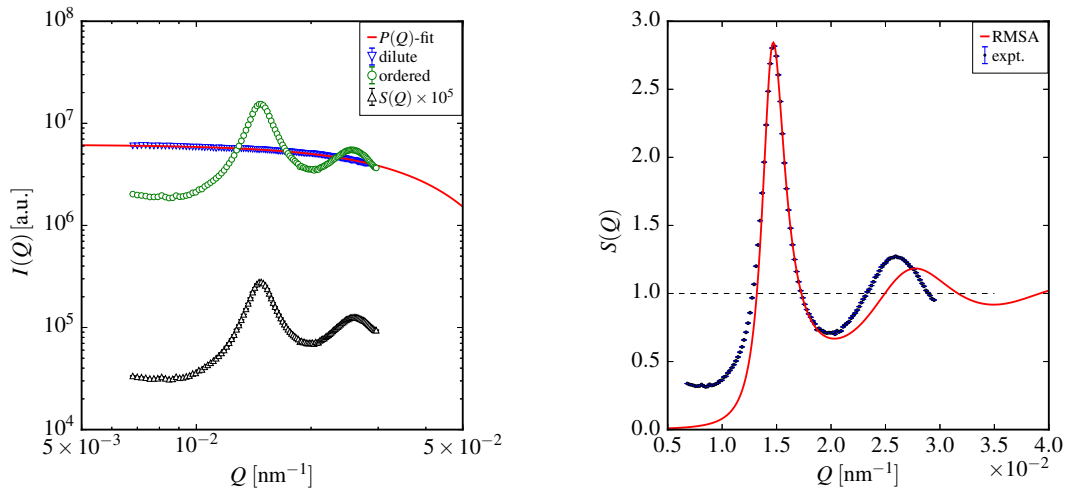


Fig. 4.5: Left: Determination of the static structure factor $S(Q)$ for the example system pTcB-70 I by SLS. Blue triangles show the scattering function of a dilute sample of pTcB-70 I, that contains 10^{-3} M KCl to avoid electrostatic particle interactions. The red curve is a fit to this function according to the theoretical form factor of Schulz-Flory distributed spheres $P(Q)$. Green circles mark the scattering function obtained for a concentrated sample of pTcB-70 I. Normalising the latter function to the $P(Q)$ -fit and taking into account the ratio of number densities of the investigated samples results in $S(Q)$, here multiplied by 10^5 for better display. Right: RMSA fit to the static structure factor determined for pTcB-70 I. Experimental data and fit show excellent agreement around the coordination maximum, which gives access to the particle number density ${}^1\rho$ and the number of surface charges Z_{eff} of the probed system. Further details are discussed in the text below.

On the left side of figure 4.5, the scattering functions of a dilute and the ordered sample

are displayed. The data points of the dilute sample are interpolated by a fit function according to a theoretical form factor of Schulz-Flory distributed spheres [90]. Normalising the scattering function of the ordered sample to this interpolation and taking into account the ratio of number densities of the investigated samples results in the experimental static structure factor $S(Q)$, that is here multiplied by 10^5 for better display. On the right side of figure 4.5, the fit of the experimental $S(Q)$ by RMSA is exemplified. The first maximum can be considered an order parameter as its amplitude, $S_{\max}(Q)$, increases with a more pronounced order of the system. In the displayed example $S_{\max}(Q) = 2.84$, which is very close to the Hansen-Verlet criterion of $S_{\text{HV}}(Q) = 2.85$ [75, 76]. Therefore, the probed liquid-like sample of pTcB-70 I is to be characterised as close to a freezing transition.

The Q -coordinate of the first maximum, Q_{\max} , is related to the most probable next neighbour distance via $d_{\max} \approx 2\pi/Q_{\max}$, which is why it is also referred to as coordination maximum. For pTcB-70 I next neighbour distances of $d_{\max} = 427$ nm are found. It can be seen, that experimental data and RMSA-fit very well agree around the first maximum, which is necessary for obtaining reliable values for the fit parameters Z_{eff} , the effective number of surface charges, and ${}^1\rho$, the particle number density. For the example system pTcB-70 I $Z_{\text{eff}} = 435$ and ${}^1\rho = 9.74 \times 10^{18} \text{ m}^{-3}$ are obtained.

Discrepancies between fit and experiment at larger Q are a known issue (cf. section 2.3.1) caused by the simplicity of RMSA as a closure relation leading to a linear integral equation. The deviations at small Q originate from the assumption of an ideally monodisperse system for the RMSA-fit. According to the fluctuation-dissipation theorem, the isothermal compressibility κ_T is connected to $S(Q)$ via $\lim_{Q \rightarrow 0} S(Q) = {}^1\rho k_B T \kappa_T$ [108]. Due to even a small polydispersity of a real, liquid-like colloidal system, the isothermal compressibility and thus the value of $S(Q \rightarrow 0)$ is increased.

For spherical particles, the number density ${}^1\rho$ is related to the volume fraction φ via $\varphi = 4\pi {}^1\rho R^3/3$, with R denoting the topological radius of the particles, which can very well be approximated by the hydrodynamic radius R_h for particle sizes found in the prepared dispersions. For pTcB-70 I, a volume fraction of $\varphi = 6.8 \times 10^{-3}$ results. Considering that the system is close to freezing, according to the amplitude of the structure factor, this unusually low volume fraction exhibits a remarkable result and underlines the potential of the colloidal systems prepared in this work for utilisation as model systems and investigations of the phase behaviour of condensed matter.

In table 4.2, all results characterising the coordination maximum, Z_{eff} and ${}^1\rho$ obtained for the investigated liquid-like ordered systems are compiled. Lower case characters at the end of the sample names indicate dilutions of the same colloidal dispersions. In most cases particles are dispersed in pure water, with a refractive index $n_m = 1.332$ and a permittivity $\varepsilon_r = 78.5$. Deviations from these characteristic values quantify the addition of glycerol to avoid multiple scattering.

Table 4.2: Compilation of results derived from static structure factors of liquid-like ordered dispersions employing RMSA. Lower case characters at the end of the sample names indicate dilutions of the same colloidal dispersion. Given are the most probable next neighbour distance d_{\max} , the amplitude of the coordination maximum $S_{\max}(Q)$, the number of effective particle surface charges Z_{eff} and the particle number density ${}^1\rho$. n_{m} is the refractive index and ϵ_{r} the relative permittivity of the dispersion medium.

Sample	d_{\max} [nm]	$S_{\max}(Q)$	Z_{eff}	${}^1\rho / 10^{18}$ [m^{-3}]	$\varphi \times 10^2$	n_{m}	ϵ_{r}
pTFEA I	410	2.66	415	11.21	0.26	1.332	78.5
pTFEA IIa	425	2.23	305	9.88	1.01	1.332	78.5
pTFEA IIb	537	2.13	310	5.39	0.55	1.332	78.5
pTFEA IIc	722	1.92	304	1.97	0.20	1.332	78.5
pTFEA VIa	318	2.17	257	23.74	1.75	1.332	78.5
pTFEA VIb	428	1.91	239	9.69	0.71	1.332	78.5
pTFEA IX	727	2.49	453	2.01	0.25	1.332	78.5
pOFPA III	771	1.83	280	1.70	0.85	1.332	78.5
pTcB-10 I	267	2.81	381	38.25	1.56	1.332	78.5
pTcB-10 IIa	400	2.68	419	12.12	0.22	1.332	78.5
pTcB-10 IIc	496	2.24	337	6.42	0.12	1.332	78.5
pTcB-10 VI	469	1.74	264	7.09	0.49	1.332	78.5
pTcB-30 I	509	1.47	158	5.44	0.37	1.332	78.5
pTcB-30 II	634	1.54	192	2.85	0.15	1.332	78.5
pTcB-30 IV	539	1.94	272	4.83	0.31	1.332	78.5
pTcB-50 III	463	2.22	305	7.66	2.04	1.411	58.5
pTcB-50 IV	610	1.31	128	2.96	0.22	1.332	78.5
pTcB-70 I	427	2.84	435	9.74	0.68	1.381	67.1
pTcB-70 II	365	2.25	277	15.67	1.28	1.381	67.1
pTcO-30	610	1.82	258	3.34	0.06	1.332	78.5

The spatial configuration at equilibrium, which is described by the parameters summarised in table 4.2, is governed by the electrostatic repulsion originating from the negative surface charges of the colloidal particles. Due to the repulsive character of interaction, next neighbour distances as large as possible are preferred between the particles for a given concentration. As a consequence, dilution leads to an increase of d_{\max} , which results in a decrease of electrostatic interaction. This is quantified in a decreasing amplitude of $S_{\max}(Q)$ indicating a loss of spatial correlation, which is supported by the results for the three dilutions of pTFEA II and the different concentrations of the systems pTFEA VI and pTcB-10 II.

Due to the long range electrostatic repulsion in charged colloids, liquid-like ordered structures evolve at particle volume fractions as low as several percent [109], which is a significantly smaller concentration than is found in hard body colloidal systems [17, 38] or molecular liquids. This is well established in the literature for charged homopolymer colloids and is also confirmed for the colloidal copolymer particle dispersions prepared and investigated in this work. In fact, table 4.2 gives evidence for the capability of these new systems to form even highly ordered liquid-like structures at volume fractions significantly smaller than one percent. This is particularly emphasised by pTFEA IIc ($\varphi = 2.0 \times 10^{-3}$, $S_{\max}(Q) = 1.92$), pTcB-10 IIc ($\varphi = 1.2 \times 10^{-3}$, $S_{\max}(Q) = 2.24$) and pTcO-30 ($\varphi = 0.6 \times 10^{-3}$, $S_{\max}(Q) = 1.82$). The corresponding static structure factors

are shown in figure 4.6.

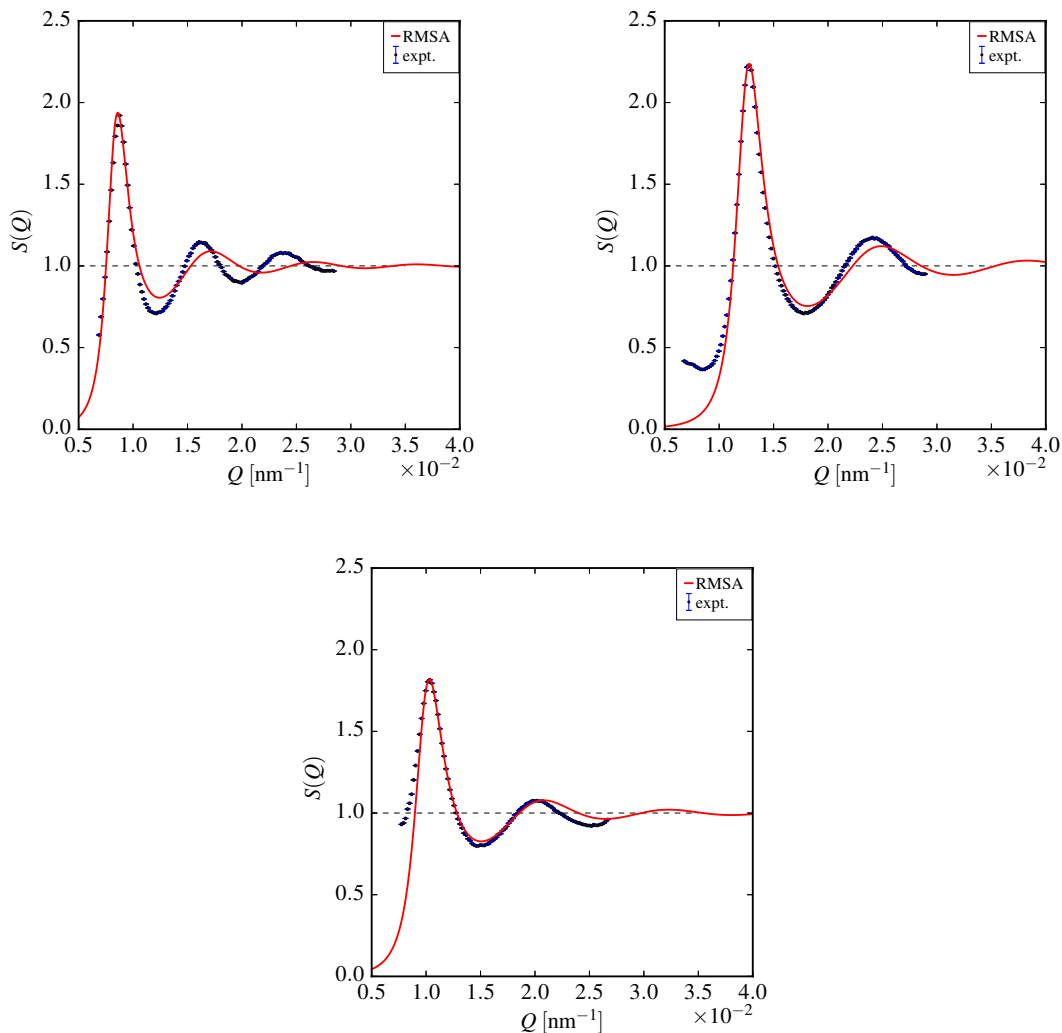


Fig. 4.6: Static structure factors and corresponding RMSA fits of colloidal dispersions with particularly low volume fractions φ : pTFEA IIc (upper left, $\varphi = 2.0 \times 10^{-3}$), pTcB-10 IIc (upper right, $\varphi = 1.2 \times 10^{-3}$), and pTcO-30 (lower centre, $\varphi = 0.6 \times 10^{-3}$). Despite these low volume fractions pronounced liquid-like structures are formed.

With pTcB-10 I there is a second investigated liquid-like ordered system besides pTcB-70 I that is close to a freezing transition with $S_{\max}(Q) = 2.81$, which confirms the applicability of these copolymer colloids as model systems for investigations of the phase behaviour of condensed matter. Due to the tunability of the particle refractive index by variation of the monomer composition of the prepared copolymers, light scattering experiments of mixtures selectively masking one component in presence of another are enabled by index-matching.

As mentioned before, RMSA is known to overestimate the number of effective surface charges. To quantify more realistic values for Z_{eff} , BD simulations for a selection of the prepared polymer colloid dispersions are performed exemplarily, as described in section 3.5.1. Due to the low polydispersities of the real dispersions compiled in table 4.1, an approximation of ideally monodisperse systems for simulation is deemed appropriate. In figure 4.7 the static structure factors obtained from BD simulations for different numbers

of surface charges are compared to the results from SLS experiments and the corresponding RMSA fit for the example pTcO-30. The structure factors are displayed as a function of the reduced scattering vector $Q\sigma$, with the particle diameter $\sigma = 72$ nm.

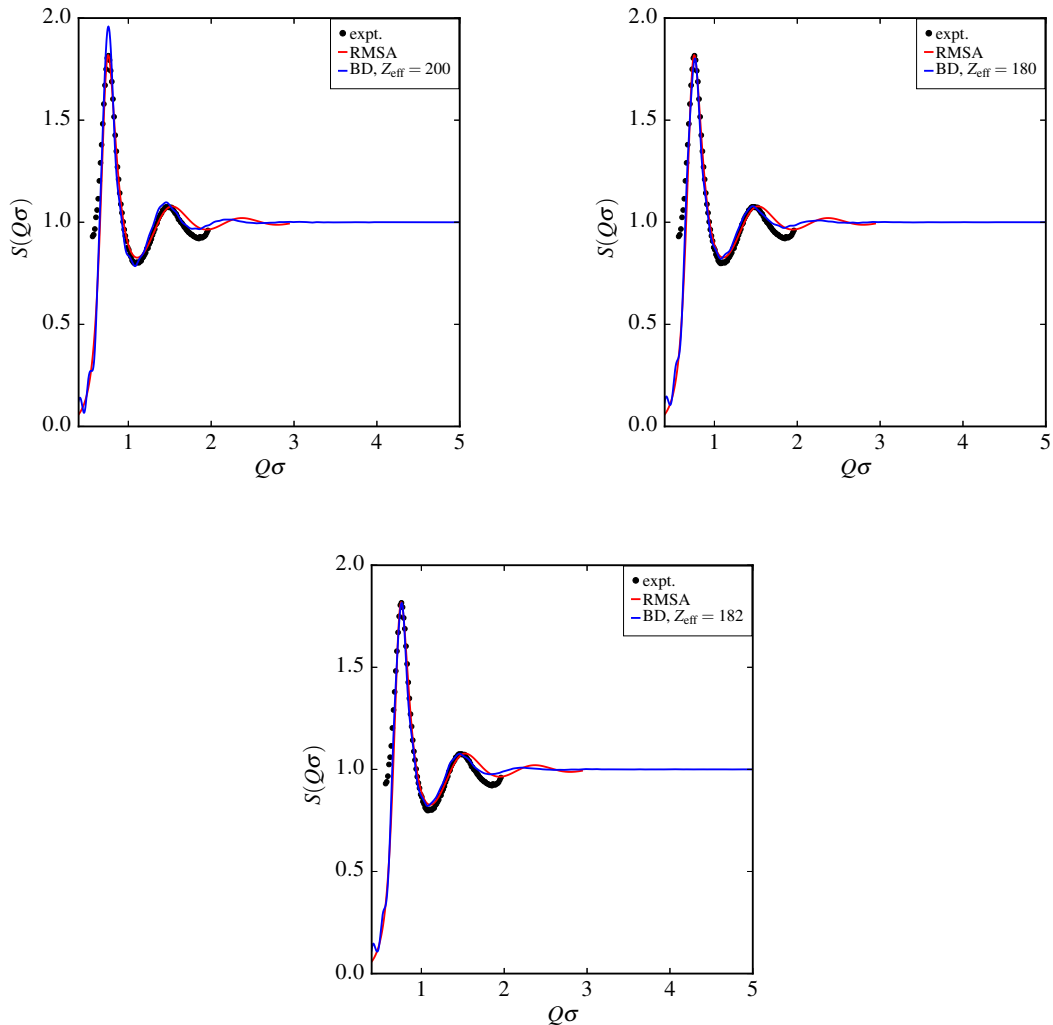


Fig. 4.7: Determination of the surface charge number Z_{eff} by comparison of the static structure factor $S(Q\sigma)$ obtained by SLS experiments and RMSA fit to $S(Q\sigma)$ resulting from BD simulations for the example system pTcO-30. The equilibrium structure at $Z_{\text{eff}} = 200$ (upper left) exhibits a structure factor, that is higher than the one determined by experiment. A simulation with $Z_{\text{eff}} = 180$ (upper right) delivers a $S(Q\sigma)$ which is slightly too small. The lower centre graphic corresponding to $Z_{\text{eff}} = 182$ shows a static structure factor obtained from BD in excellent agreement to the SLS result.

At first, the system is simulated for 10^5 time steps at $Z_{\text{eff}} = 200$ until equilibrium, resulting in a higher amplitude of the structure factor than obtained from SLS. Subsequently, the charge number is decreased to 180 and the system is re-equilibrated after another 5×10^4 steps. $S_{\text{max}}(Q)$ of the corresponding simulated structure factor is slightly smaller than the amplitude of the experimental $S(Q)$. After 3×10^4 further simulation steps at $Z_{\text{eff}} = 182$ the structure factor representing the simulated equilibrium configuration shows excellent agreement with the static structure factor obtained from light scattering experiments.

In this case, the deviation between the number of charges derived from RMSA and that determined via BD simulations is 92, representing an error of more than 50% based on the simulation result. In table 4.3 numbers of effective surface charges obtained by BD simulations in analogous manner are compiled for several other colloidal dispersions and compared to the corresponding Z_{eff} identified by RMSA fitting of SLS data.

Table 4.3: Compilation of numbers of effective surface charges Z_{eff} determined by RMSA-fit of SLS data and by BD simulations. Generally, BD delivers significantly smaller charge numbers, due to the known overestimation of Z_{eff} by RMSA. A rough tendency of growing discrepancy between Z_{eff} (BD) and Z_{eff} (RMSA) is identified with increasing charge number.

Sample	Z_{eff} (RMSA)	Z_{eff} (BD)	Z_{eff} (RMSA)/ Z_{eff} (BD)
pTFEA IIb	310	200	1.55
pTFEA IIc	304	210	1.45
pTFEA VIb	239	160	1.49
pTFEA IX	453	285	1.59
pOFPA III	280	212	1.32
pTcB-30 I	158	123	1.28
pTcB-30 II	192	145	1.32
pTcB-30 IV	272	185	1.47
pTcB-50 III	305	185	1.65
pTcB-50 IV	128	110	1.16
pTcB-70 I	428	245	1.75
pTcB-70 II	277	178	1.56
pTcO-30	274	182	1.51

RMSA is known to give an overestimation of the number of surface charges. Thus expectedly, the charge numbers determined by BD are generally smaller than those derived from RMSA. A rough tendency is recognised, that the relative discrepancy between the two values of Z_{eff} of one colloidal system, which is quantified by the ratio Z_{eff} (RMSA)/ Z_{eff} (BD), increases with rising charge number, as can be seen in table 4.3. However, there are exceptions to this rule, e. g., Z_{eff} (RMSA)/ Z_{eff} (BD) = 1.59 for pTFEA IX with Z_{eff} (RMSA) = 453 but for pTcB-50 III a larger ratio Z_{eff} (RMSA)/ Z_{eff} (BD) = 1.65 is determined although the charge number Z_{eff} (RMSA) = 305 is significantly smaller. Hence the observed rough tendency may serve as a rule of thumb but an accurate prediction of the differences between charge numbers determined by RMSA and BD on this basis is not advisable.

4.5 Influence of index-matching with glycerol on the number of surface charges

In chapters 5 and 6 components of colloidal mixtures are selectively index-matched using water/glycerol mixtures, such that in light scattering experiments these colloids do not contribute to the scattering signal. A reduced number of effective charges Z_{eff} resulting from the suppressed dissociation of sulfonic acid surface groups in less protic dispersion media with increased glycerol content, e. g., by index-matching, would change the structure and dynamics of colloidal dispersions. So far, a systematic investigation of how glycerol content may affect Z_{eff} of highly charged particles is not described in the literature.

Therefore, six samples of pTcB-70 I dispersed in defined mixtures of water and glycerol are prepared as described in section 3.4.2. To avoid multiple scattering due to the refractive index $n_p = 1.444$ of pTcB-70 I, a minimum mass content of 10 % glycerol is found to be necessary. The other five mixtures exhibit glycerol mass ratios of 15 %, 20 %, 30 %, 40 % and 50 % with identical particle number density of pTcB-70 I.

The static structure factors of the prepared, liquid-like ordered systems are determined as described in section 3.4.2 and as illustrated for several other systems of liquid-like order in section 4.4. Figure 4.8 gives an overview of the obtained static structure factors for the six samples of pTcB-70 I dispersed in different water/glycerol mixtures. Again, the evaluation of the experimental data is performed with RMSA to determine ${}^1\rho$ and Z_{eff} .

From figure 4.8 it is obvious, that the six probed samples exhibit very similar particle number densities, such that the preparation is considered successful in that respect. Quantitatively, a mean number density $\langle {}^1\rho \rangle = 1.01 \times 10^{19} \text{ m}^{-3}$ with a standard deviation of $3.78 \times 10^{17} \text{ m}^{-3}$ is obtained, which corresponds to a relative deviation of around 3.7 %. For the number of effective surface charges a mean value of $\langle Z_{\text{eff}} \rangle = 439$ with a standard deviation of 14 or a relative deviation of little more than 3 %, respectively, is determined. Note, that there is no distinct proportionality between the determined values for ${}^1\rho$ and the corresponding number of charges. With regard to the obtained relative deviations the number of effective charges in a liquid-like ordered system of charged colloidal spheres seems to be independent of the composition of a water/glycerol dispersion medium. Thus no such effects are expected to influence the experiments on mixtures reported in sections 5 and 6.

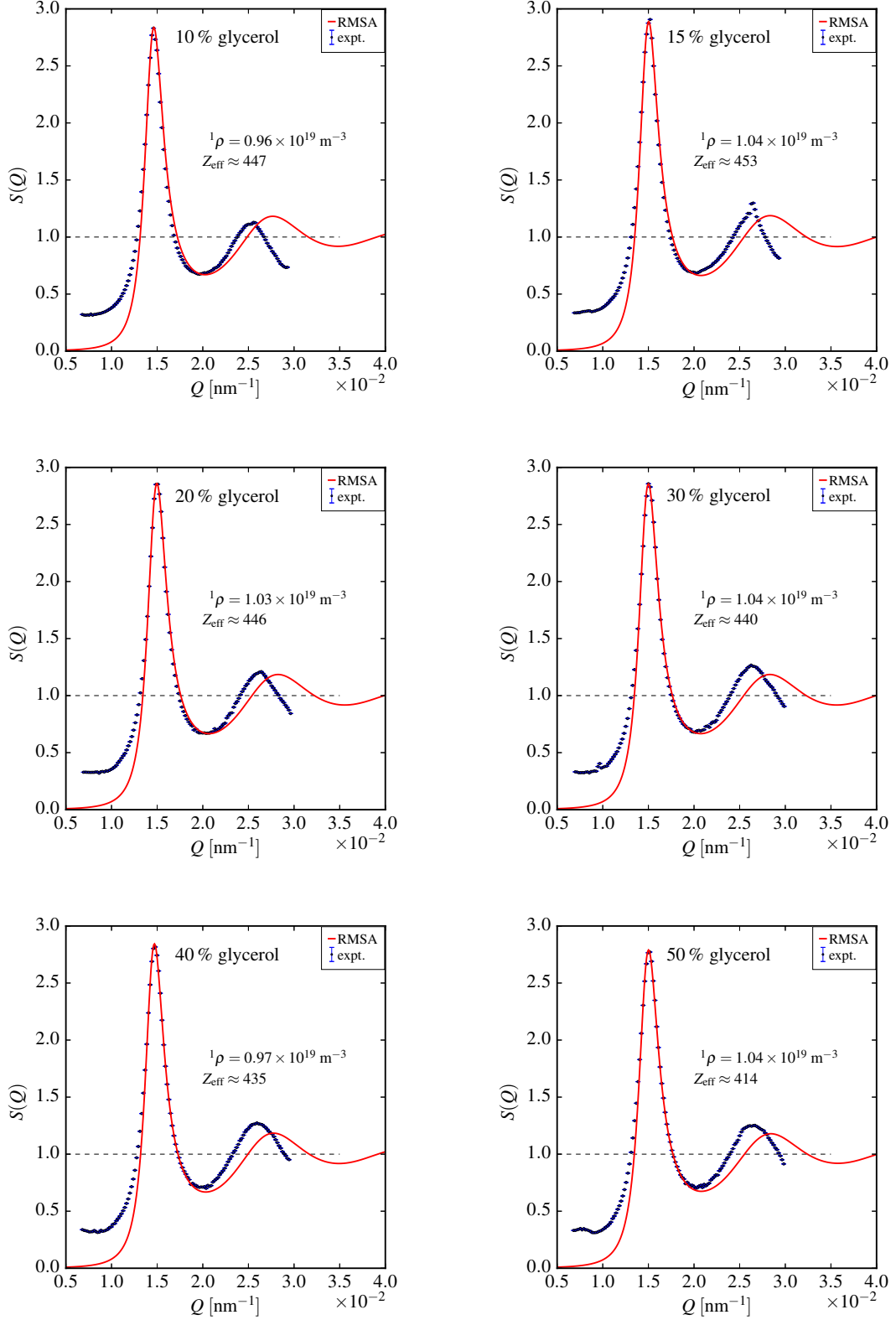


Fig. 4.8: Static structure factors of pTcB-70 I particles dispersed in water/glycerol media with six different glycerol mass ratios ω_{gly} in the range $10\% \leq \omega_{\text{gly}} \leq 50\%$. Within a small uncertainty the particle number ratios ${}^1\rho$ are identical. In good approximation the number of surface charges Z_{eff} is proven independent from the water/glycerol dispersion medium up to $\omega_{\text{gly}} = 50\%$.

5 Investigations of binary mixtures

In chapter 4 evidence is presented, that with the preparation of colloidal copolymer dispersions consisting of BA and TFEA or TFEA and OFPA in different compositions and under different reaction conditions systems with defined particle sizes, number densities and refractive indices are available. This gives access to the preparation of binary mixtures of colloidal dispersions, the characterisation of which is facilitated exploiting the possibility of selectively index-matching one component in light scattering experiments using water/glycerol dispersion media.

In the first section of this chapter strongly scattering PS tracer particles are employed in a binary mixture with index-matched pTFEA VI for the investigation of tracer self-diffusion influenced by a homo-colloidal matrix by means of DLS and BD simulations. Only few other similar studies of tracer diffusion of charged spheres in a single component colloidal matrix interacting via an electrostatic potential are published so far [74, 110]. The results presented in 5.1 shall in part serve as a verification of the earlier findings of other groups and also give first evidence for the applicability of the newly prepared systems presented in this work for studying mixtures of charged colloidal dispersions.

The second section presents investigations of binary mixtures of charged colloidal dispersions with similar number densities. From these, exploiting index-matching with water/glycerol dispersion media, partial static structure factors ($S_{ij}(Q)$) are obtained by means of light scattering experiments and compared to results of BD simulations. This comparative study is complemented by comprehensive BD investigations of the influences of the components' number ratios, particle sizes, and effective numbers of surface charges as well as of the temperature of the system on the partial intermediate scattering functions $S_{ij}(Q, t)$.

5.1 Tracer particles in a homo-colloidal matrix

5.1.1 Light scattering investigations of tracer self-diffusion in a homo-colloidal matrix

Polystyrene (PS) is an organic polymer that is widely applied and as such very well characterised. Colloidal dispersions of PS exhibit relatively high refractive indices close to $n_{\text{PS}} \approx 1.58$ [111, 112]. Therefore, these strongly scattering particles are predestined for their application as tracers in a binary mixture with a colloidal system of less scattering power. Such mixtures can be composed of a small amount of large PS particles as tracers dispersed in a majority matrix of smaller PS spheres (cf. works by Krause, Nägele, Klein et al. [74, 113–115]). Härtl et al. investigated mixtures of small amounts of PS tracer particles in a colloidal suspension of low-refractive-index poly(1H-1H-heptafluorobutyl acrylate) [116] and poly(1H,1H,7H-dodecafluoro-1-heptyl methacrylate) particles [110]. However, these are the only systematic studies on tracer diffusion in binary mixtures of charged colloids. The newly developed systems with tunable refractive index prepared

in this work exploit an alternative approach to investigate tracer diffusion, i. e., index-matching a homo-colloidal matrix employing a water/glycerol dispersion medium in a binary mixture with trace amounts of PS. Dynamic light scattering experiments will then give access to tracer dynamics without disturbances caused by scattering contributions from matrix particles.

An adequate polystyrene dispersion for these tracer dynamics investigations is prepared according to the emulsion polymerisation procedure described earlier in this work (cf. section 3.2). 30 mmol of the monomer styrene are dispersed in 250 mL of water. 105 mg of Na_2SO_3 and 1 mg of $(\text{NH}_4)_2\text{Fe}(\text{SO}_4)_2$ are added as redox catalyst system. The polymerisation is performed at a temperature of 80°C and initiated by the addition of 31 mg of $\text{K}_2\text{S}_2\text{O}_8$. The third batch of colloidal PS (PS3) is identified most suitable for the performance of tracer dynamics investigations. The particle size distribution, characterised by a most probable hydrodynamic radius of $R_{h,\text{max}} = 106 \text{ nm}$, is determined by DLS according to section 3.4.1 and displayed on the left side of Fig. 5.1. A Schulz-Flory fit is used to quantify the polydispersity of the prepared polystyrene particles as $p = 0.130$. A transmission electron micrograph of PS3 spheres, taken at the Centre for Electron Microscopy of the Universitätsmedizin Rostock (EMZUniRo) and presented on the right side of Fig. 5.1, validates the mean particle size determined by DLS and likewise gives evidence for a slightly elevated polydispersity of the particles.

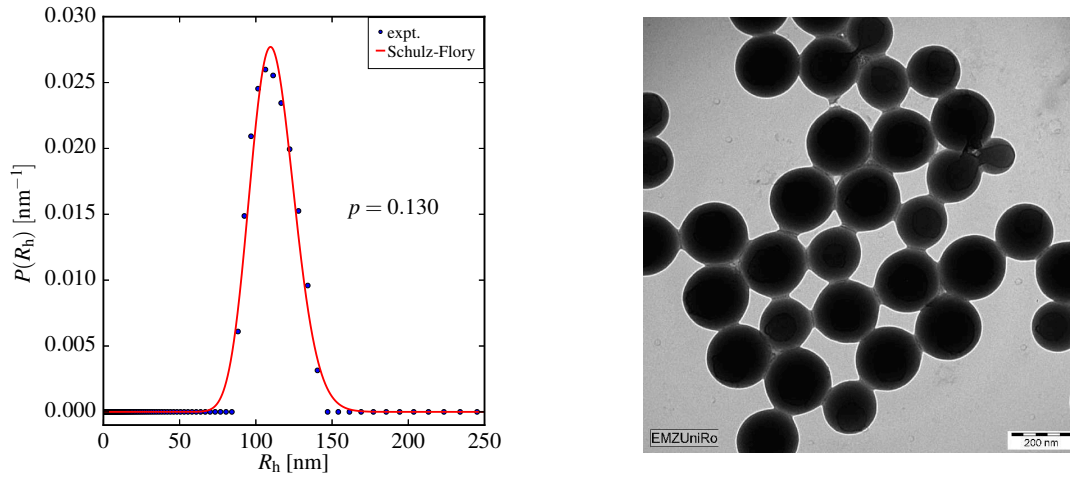


Fig. 5.1: Left: Particle size distribution for PS3 obtained by DLS employing the CONTIN algorithm, resulting in a most probable hydrodynamic radius $R_{h,\text{max}} = 106 \text{ nm}$. The polydispersity $p = 0.130$ is derived from a Schulz-Flory fit according to eq. (3.10). Right: Transmission electron micrograph of PS3 spheres, taken at the Centre for Electron Microscopy of the Universitätsmedizin Rostock (EMZUniRo).

In this work, a binary stock mixture consisting of trace amounts of PS3 mixed with roughly 200 times the number of pTFEA VI is prepared. The particle number ratios of the two components in this mixture are designated as ${}^1q_{\text{PS3},0}$ and ${}^1q_{\text{matrix},0}$. The refractive index of the dispersion medium water/glycerol in each of the samples prepared and investigated in this section is adjusted to $n_m = 1.3945$, which corresponds to a mass ratio of glycerol of about 47.5% [93]. This value is very close to the refractive index of pTFEA particles of $n_p = 1.402$ (cf. table 4.1), such that the scattering power of the matrix particles is drastically reduced and the scattered intensity in dynamic light scattering

experiments can be considered to originate solely from PS3 in good approximation. An experimental justification for this assumption follows below.

Finally, the short and long time tracer self-diffusion shall be investigated in dependence on ${}^1\varrho_{\text{PS3}}$ and ${}^1\varrho_{\text{matrix}}$. Therefore, two sets of samples are prepared. First, starting from the stock mixture of PS3 and pTFEA VI, the particle number density of the tracer component is successively decreased by dilution with a dispersion of pTFEA VI in water/glycerol, that exhibits the same relative concentration of pTFEA as the stock mixture and the same refractive index. Thus, the particle number density of the matrix component remains constant. ${}^1\varrho_{\text{PS3}}$ is reduced to 75 %, 67 %, 50 %, 33 % and 25 %, respectively, relative to ${}^1\varrho_{\text{PS3},0}$. This first sample set is represented by the middle row of the scheme displayed in Fig. 5.2.

Starting from the mixture with ${}^1\varrho_{\text{PS3}} = 0.50 {}^1\varrho_{\text{PS3},0}$, a second set of samples is prepared by successive dilution with a dispersion of PS3 in water/glycerol, that has the same relative concentration of polystyrene and the same refractive index. Thus, the particle number density of PS3 remains at $0.50 {}^1\varrho_{\text{PS3},0}$ and the particle number density of pTFEA VI is decreased to 95 %, 90 %, 80 %, 70 % and 60 %, respectively, relative to ${}^1\varrho_{\text{matrix},0}$. This second sample set is represented by the bottom row of the scheme in Fig. 5.2. A mixed-bed ion exchanger is added to all of the prepared mixtures, which are thoroughly shaken and then left for at least several days before continuing with light scattering experiments, to assure an equilibrium state of self-organisation of the pTFEA VI matrix.

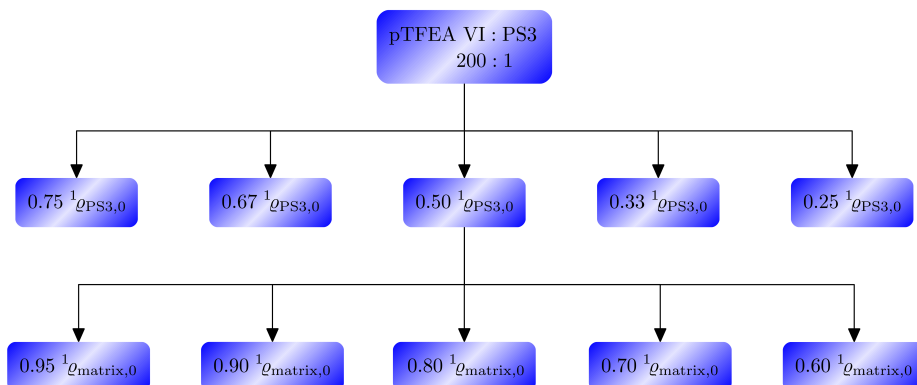


Fig. 5.2: Schematic illustration of the preparation of samples investigated in this section. Starting from the stock binary mixture consisting of pTFEA VI and PS3 in the ratio 200:1, a first set of samples with constant matrix number density ${}^1\varrho_{\text{matrix},0}$ and decreasing tracer number density ${}^1\varrho_{\text{PS3}}$ is prepared. Continuing from the sample with ${}^1\varrho_{\text{PS3}} = 0.50 {}^1\varrho_{\text{PS3},0}$ a second sample set with progressively reduced matrix number density ${}^1\varrho_{\text{matrix}}$ is prepared, while the tracer number density remains at ${}^1\varrho_{\text{PS3}} = 0.50 {}^1\varrho_{\text{PS3},0}$.

For a verification of successful index-matching, despite the small discrepancy between $n_{\text{m}} = 1.3945$ and $n_{\text{pTFEA}} = 1.402$, the scattering functions $I(Q)$ of all prepared binary mixtures of PS3 and pTFEA VI are determined by means of SLS according to the scheme described in section 3.4.2. In Fig. 5.3 these are compared to the form factor $P(Q)$ of pure PS3, that is obtained by a separate experiment using a sample of highly diluted PS3 dispersed in an aqueous solution of 10^{-3} M KCl. The scattering vectors are corrected for varying refractive indices of different water/glycerol compositions (cf. eq. (2.6)).

Due to the preparation of the binary stock mixture, the particle number density of pT-

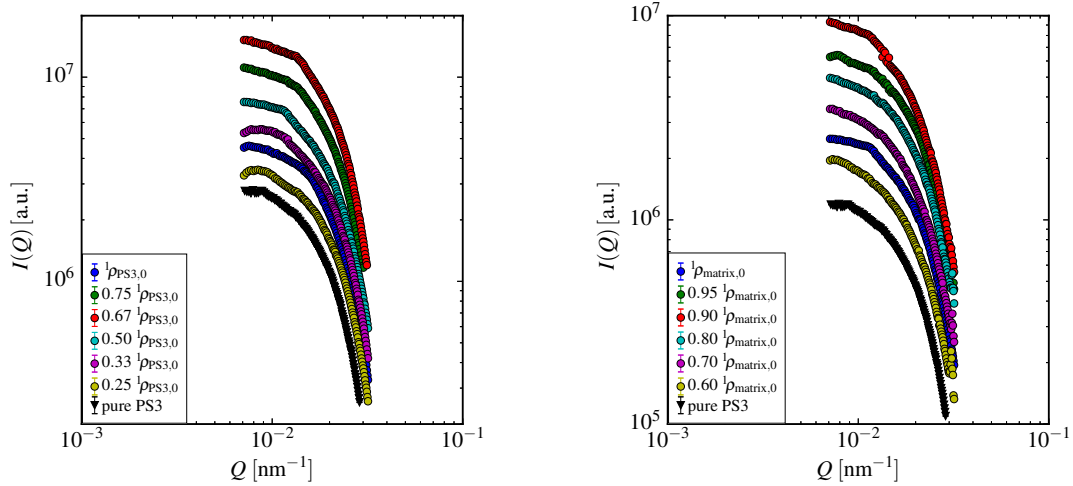


Fig. 5.3: Scattering functions $I(Q)$ of binary mixtures of PS3 tracers and pTFEA VI determined by SLS. On the left results for the first sample set with varying tracer number density are shown, while the graphic on the right presents $I(Q)$ for samples with varying matrix number density. In both pictures the scattering function of a highly diluted sample of pure PS3 containing 10^{-3} M KCl is included for comparison. Graphs obtained for the mixtures do not significantly differ from that of pure PS3.

FEA VI can be expected to be decreased by no more than a factor of two compared to the value for pTFEA VIa obtained from RMSA (cf. table 4.2). As the sample pTFEA VIb still exhibits a pronounced liquid-like structure at an even lower number density than $^1\varrho_{\text{matrix},0}$, the scattering functions of the binary stock mixture and the first set of diluted samples would show distinct oscillations, if the refractive index significantly differed from the matching point n_{pTFEA} . As can be seen on the left in Fig. 5.3, none of the scattering functions of the samples with the pTFEA number density $^1\varrho_{\text{matrix},0}$ is characterised by considerable deviations from $P(Q)$ of pure PS3. This becomes even clearer by the determination of the corresponding hypothetical static structure factor. Fig. 5.4 displays the hypothetical $S(Q)$ of the binary mixture with $^1\varrho_{\text{matrix}} = ^1\varrho_{\text{matrix},0}$ and $^1\varrho_{\text{PS3}} = 0.5 \ ^1\varrho_{\text{PS3},0}$. Clearly, $S(Q) \approx 1$ over the whole investigated Q -range, indicating the absence of any structural ordering. Thus, no significant influence of the pTFEA matrix on the scattering function is detected, due to successful index-matching. The scattering functions determined for the second set of samples with varying matrix number density and constant tracer number density are presented on the right side in Fig. 5.3. Similar to the first set of samples, marginal oscillations can be recognised in the scattering functions corresponding to higher matrix concentrations. With successive dilution of the matrix component, even these vanish as a consequence of weakened scattering power of pTFEA VI, such that the scattering functions relating to the least matrix number densities presented appear identical to the form factor of pure PS3.

Having verified, that the scattering signal of the prepared binary mixtures with index-matched matrix originates only from the polystyrene tracer particles in good approximation, the self-diffusion of highly charged tracer particles in presence of like-charged colloidal particles can be investigated. For this purpose, DLS experiments are performed on each of the samples presented in Fig. 5.2 according to the data acquisition procedure described in section 3.4.3. From the temporal fluctuations of the detected scattering

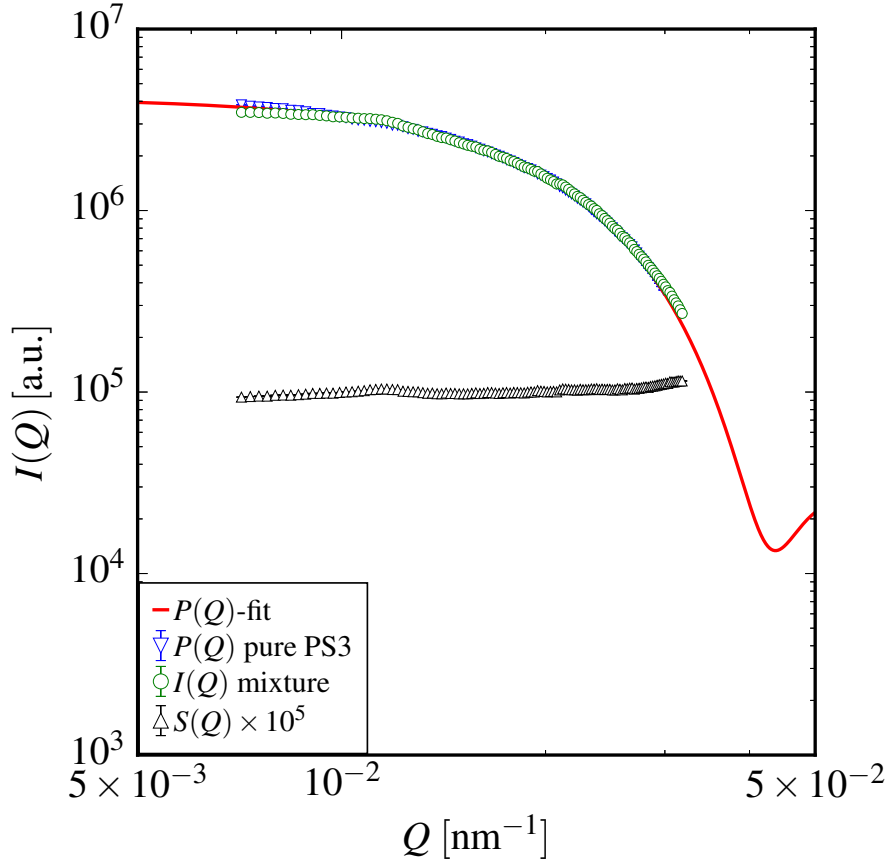


Fig. 5.4: Determination of a hypothetical static structure factor $S(Q)$ for the binary mixture with matrix number density ${}^1\rho_{\text{matrix},0}$ and tracer number density ${}^1\rho_{\text{PS3}} = 0.5 {}^1\rho_{\text{PS3},0}$. The scattering function $I(Q)$ of the mixture and the form factor $P(Q)$ of pure PS3 are identical within experimental accuracy, such that $S(Q) \approx 1$ over the observed Q -range, which proves successful index-matching of the pTFEA VI matrix.

intensities homodyne autocorrelation functions $g_2(Q, \tau)$ are computed in dependence on the observed scattering vector Q and the delay time τ , as stated in (2.11). As the prepared mixtures are ergodic systems and a diffusive motion of the tracer particles can be assumed, from which scattering mainly originates, the corresponding field autocorrelation functions $g_1(Q, \tau)$ can be obtained and approximated as single exponential functions (cf. eqs. (2.14), (2.15), (3.8)). From the initial slopes of these autocorrelation functions the relaxation rates $\Gamma(Q)$ for the short-time limit are determined as shown at the end of section 3.4.1. In the upper row of Fig. 5.5 an example for a typical field autocorrelation function, detected for one of the investigated binary mixtures, as well as an example linear fit to the corresponding function $\ln g_1(\tau)$ for determining the initial slope are presented. The so obtained short-time relaxation rates for both sets of prepared binary mixtures are compiled in comparison to $\Gamma(Q)$ for a dispersion of pure, highly diluted PS3 in an aqueous solution of 10^{-3} M KCl in the bottom row of Fig. 5.5.

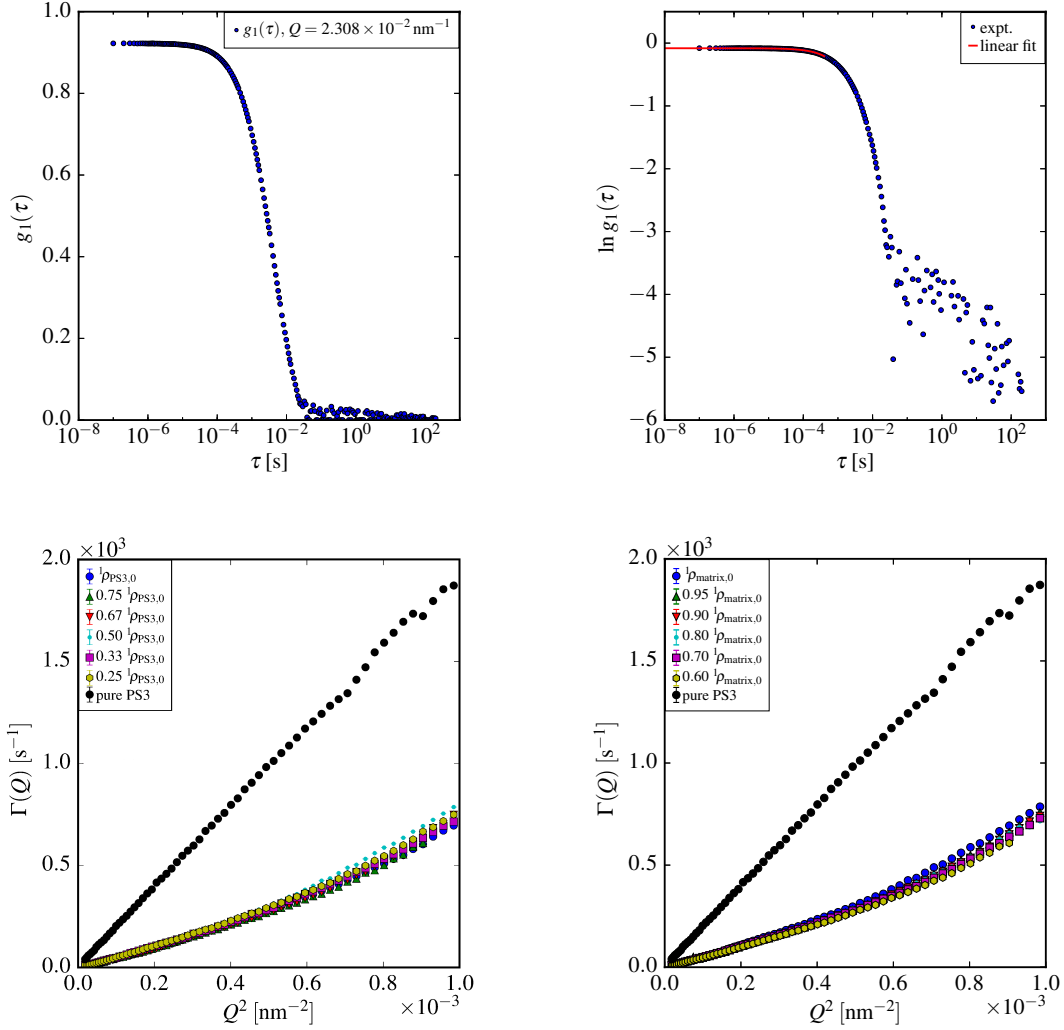


Fig. 5.5: Upper left: Example field autocorrelation function $g_1(\tau)$ at $Q = 2.308 \times 10^{-2} \text{ nm}^{-1}$ obtained by DLS with one of the binary mixtures employing the Siegert relation (2.14). Upper right: Example short-time fit of $g_1(\tau)$ to determine the initial slope, which is the negative relaxation rate $-\Gamma$. Bottom row: Plots of short-time $\Gamma(Q)$ vs. Q^2 for the first (left) and second (right) set of binary mixtures in comparison to $\Gamma(Q)$ for a sample of highly diluted, pure PS3 containing 10^{-3} M KCl .

At first glance, the short-time relaxation rates for all investigated mixtures are very similar. From the illustration in Fig. 5.5 no tendencies corresponding to the degree of dilution among the differently concentrated samples are discernible. A more quantitative discussion of this matter will follow below. Qualitatively, the tracer particles exhibit distinctly lower short-time self-diffusion coefficients in the observed binary mixtures than are observed for pure PS3 particles, as can be deduced from the much steeper slope of $\Gamma(Q)$ for the single-compound system. As expected, the diffusive motion of polystyrene tracer particles is slowed down in an ordered colloidal matrix. Due to the addition of highly charged pTFEA spheres with rather large number density, that occupy the space between PS spheres, the repulsive electrostatic force acting upon the tracer particles is largely increased. By matching the refractive index of the dispersion medium to the one of the matrix particles, effectively, the self-diffusion of the tracer species in a repulsive electrostatic field is observed. Thereby, the possible distance to be covered by the diffusing

particles is strongly decreased. This effect holds for short-time as well as for long-time diffusion.

Opposite to pure, diluted PS3 particles a deviation from the Landau-Placzek proportionality of the short-time relaxation rates $\Gamma(Q)$ to Q^2 is observed for PS3 tracers in an ordered colloidal matrix. At larger scattering vectors an increase of the slope is noted, as is shown in Fig. 5.5. Considering the relation $Q \approx 2\pi/d$ between the scattering vector and the distance in real space d , the studied tracer particles seem to move faster over small distances than over larger distances. This can be explained, again referring to the index-matched matrix particles with their repulsive, electrostatic field. The probability of a tracer particle being influenced by this field and the extent of this influence are much smaller, when observing its motion over small distances. Extending the view to larger distances, the particle trajectory is more likely to be influenced due to electrostatic deflection. This also means, that the particle might be directed back to its starting point, which is known as memory effect. Thus, while the diffusion over short paths is quasi-free, long diffusion paths are affected by electrostatic repulsion of the host particles.

Since the impact of the charged matrix particles on the self-diffusion of the polystyrene spheres is of special interest for the prepared mixtures, the short-time self diffusion coefficients D_S^S are determined from the slopes of the relaxation rates according to the Landau-Placzek relation (2.16) in the range $2 \times 10^{-5} \text{ nm}^{-2} \leq Q^2 \leq 4 \times 10^{-4} \text{ nm}^{-2}$. The obtained short-time self-diffusion coefficients for the two sample sets of binary mixtures are compiled in table 5.1 and table 5.2, respectively.

From the field autocorrelation functions employed to determine the short-time self-diffusion behaviour, also the long-time self-diffusion coefficients D_S^L are accessible. As described before in section 2.3.2, D_S^L is the limiting value of the time-dependent self-diffusion coefficient $D_S(t)$ for $t \rightarrow \infty$. Experimentally, a very good approximation for this time regime is available at delay times τ distinctly larger than the structural relaxation time τ_t . However, as $\lim_{\tau \gg \tau_t} (g_1(Q, \tau)) = 0$ for the here observed systems, noise superimposes the physical data. Thus, a compromise between excluding noise and observing sufficiently large delay times is necessary, in order to obtain reliable long-time self-diffusion coefficients. An example for such a long-time evaluation of a typical field autocorrelation function is presented in the upper right of Fig. 5.6. The long-time relaxation rates obtained in this way according to (2.16) for the two sets of binary mixtures are displayed in the bottom row of Fig. 5.6, together with the long-time relaxation rate for pure, highly diluted PS3 in an aqueous solution of 10^{-3} M KCl .

Obviously, the long-time relaxation rates do not proceed along Q^2 as smooth as their short-time analogues. This is due to increased statistical uncertainty within the long-time fitting procedure of the field autocorrelation function compared to the short-time fit, that is based on a larger number of experimental data points. Further it is apparent, that the long-time relaxation rate of PS3 is very similar to its short-time $\Gamma(Q)$ graph in Fig. 5.5. In agreement to this observation the obtainable long-time self-diffusion coefficient of PS3, $D_S^L = 2.18 \times 10^{-12} \text{ m}^2\text{s}^{-1}$, is nearly identical to the short-time self-diffusion coefficient, $D_S^S = 2.11 \times 10^{-12} \text{ m}^2\text{s}^{-1}$. As stated earlier in section 2.3.2, the relation $D_S^L \leq D_S^S$ holds universally. The slightly larger value for D_S^L most likely originates from the larger experimental uncertainty of the long-time relaxation rate mentioned above. Within experimental accuracy $D_S^L \approx D_S^S$ is fulfilled, as the investigated sample of pure PS3 is highly diluted and exhibits strong electrostatic screening of the charged macroions due to the addition of 10^{-3} M KCl .

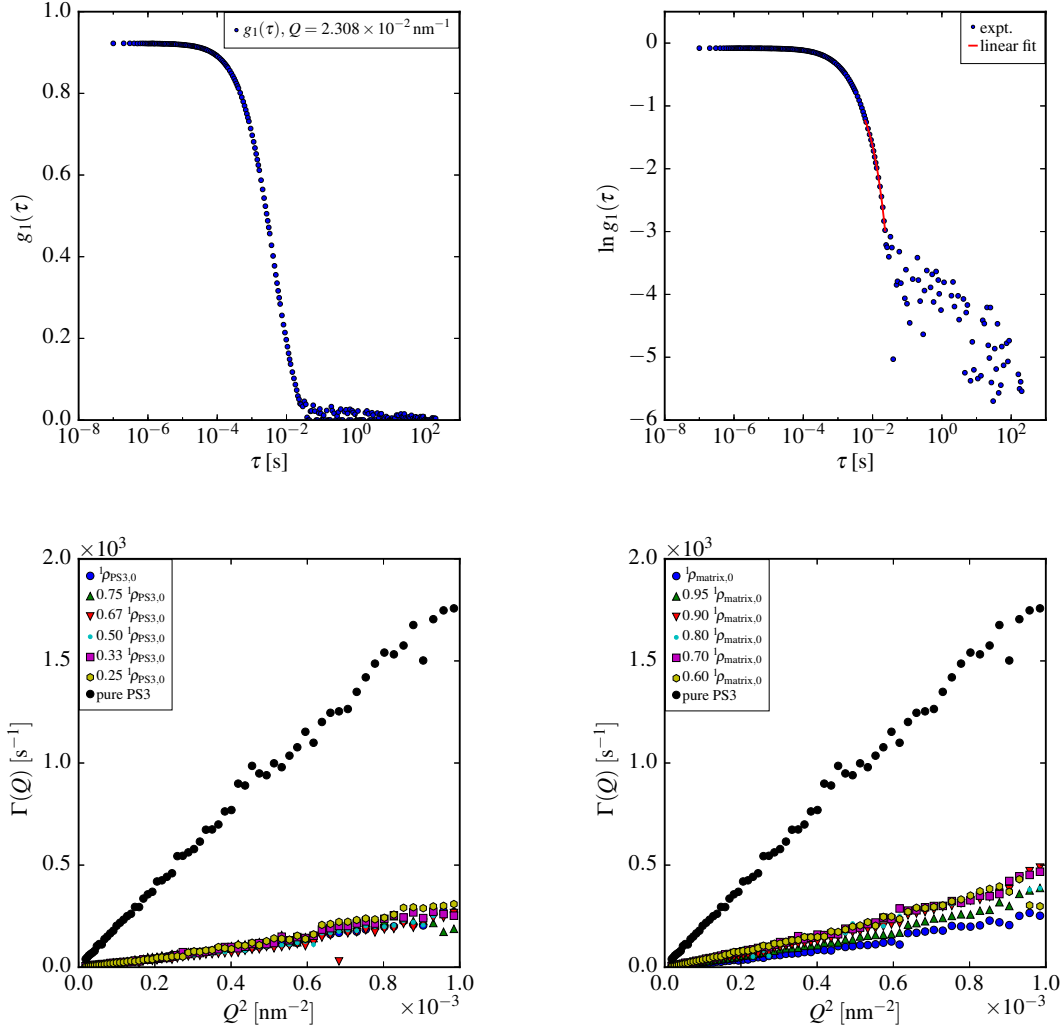


Fig. 5.6: Upper left: Example field autocorrelation function $g_1(\tau)$ at $Q = 2.308 \times 10^{-2} \text{ nm}^{-1}$ obtained by DLS with one of the binary mixtures employing the Siegert relation (2.14). Upper right: Example long-time fit of $g_1(\tau)$ to determine the slope, which is the negative relaxation rate $-\Gamma$. Bottom row: Plots of long-time $\Gamma(Q)$ vs. Q^2 for the first (left) and second (right) set of binary mixtures in comparison to $\Gamma(Q)$ for a sample of highly diluted, pure PS3 containing 10^{-3} M KCl .

Generally, the long-time relaxation rates of the binary mixtures versus Q^2 have smaller slopes than their short-time analogues, which is apparent when comparing the graphs presented in the bottom rows of Figs. 5.5 and 5.6. This indication of slower long-time diffusion compared to short-time diffusion is based on the behaviour of the colloidal particles on a mesoscopic scale, that is described already in section 2.3.2. For a quantification of this observation, the long-time self-diffusion coefficients of the PS3 particles in the investigated binary mixtures are determined from the slopes of the relaxation rates according to the Landau-Placzek relation (2.16). To maintain comparability to the short-time evaluation, the range $2 \times 10^{-5} \text{ nm}^{-2} \leq Q^2 \leq 4 \times 10^{-4} \text{ nm}^{-2}$ is taken as a basis. The obtained long-time self-diffusion coefficients for the two sample sets of binary mixtures are compiled in table 5.1 and table 5.2, respectively.

Table 5.1: Compilation of short-time (D_S^S) and long-time (D_S^L) self-diffusion coefficients of PS3 tracers determined for the first sample set with varying tracer number density.

${}^1\rho_{\text{PS3}}/{}^1\rho_{\text{PS3},0}$	$D_S^S/10^{-12}$ [m^2s^{-1}]	$D_S^L/10^{-12}$ [m^2s^{-1}]
1.00	0.53	0.24
0.75	0.53	0.25
0.67	0.55	0.19
0.50	0.59	0.20
0.33	0.55	0.24
0.25	0.57	0.25

Table 5.2: Compilation of short-time (D_S^S) and long-time (D_S^L) self-diffusion coefficients of PS3 tracers determined for the second sample set with varying matrix number density. Also the impact of adding 10^{-3} M KCl is shown.

${}^1\rho_{\text{matrix}}/{}^1\rho_{\text{matrix},0}$	$D_S^S/10^{-12}$ [m^2s^{-1}]	$D_S^L/10^{-12}$ [m^2s^{-1}]
1.00	0.59	0.20
0.95	0.55	0.29
0.90	0.55	0.33
0.80	0.56	0.38
0.80 + 10^{-3} M KCl	0.54	0.49
0.70	0.54	0.39
0.60	0.52	0.40

At first glance, the findings for D_S^S and D_S^L for tracer diffusion of PS3 particles in an index-matched matrix of pTFEA VI spheres agree with the universal relation $D_S^L \leq D_S^S$. Further, table 5.1 suggests, that neither short-time nor long-time self-diffusion are systematically influenced by a decrease in the particle number density of the tracer component up to a factor of four relative to the original number density. This is an expectable and reasonable result, as the binary stock mixture is composed of a number ratio of about 0.005 PS3 vs. 0.995 pTFEA VI, such that a dilution of PS3 by a factor four would not have a significant effect on this composition. The presentation of the ratio D_S^L/D_S^S clarifies, that there is no directed dependency of the self-diffusion behaviour of the tracer particles on the tracer particle number density in the investigated interval, as is presented on the left side of Fig. 5.7. Rather, the ratios seem to be distributed around a mean value of $\langle D_S^L/D_S^S \rangle = 0.41$. Presumably, the deviations from this mean value are subject to experimental accuracy.

Investigating the second set of samples, the influence of a decreasing number density of the matrix component on the long-time tracer diffusion is revealed. In the lower right of Fig. 5.6 an enhanced diffusive motion over long times is indicated by a successive increase of the slope of the relaxation rate $\Gamma(Q)$ vs. Q^2 with decreasing relative number density of the pTFEA VI matrix. This becomes even clearer by magnifying the lower Q^2 -region, which the linear fitting for obtaining the long-time self-diffusion coefficients is based on, as presented in Fig. 5.8.

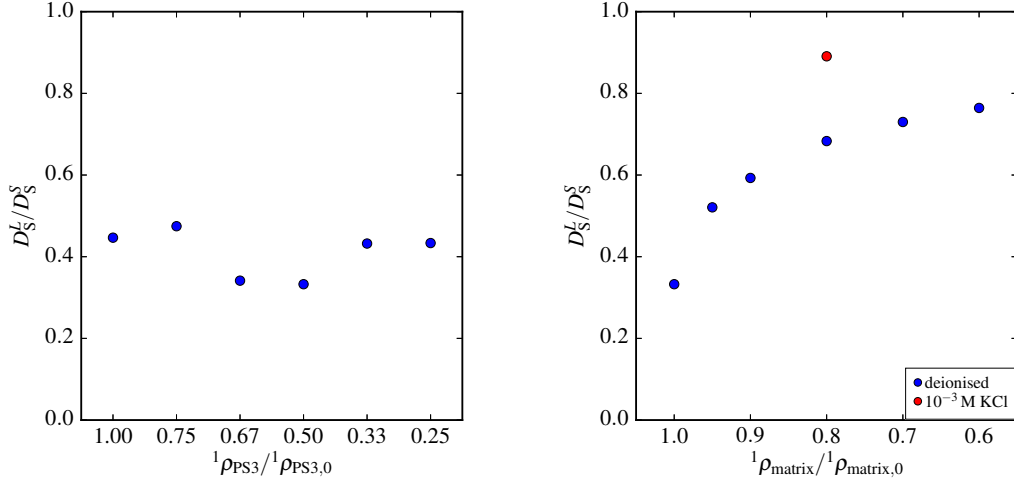


Fig. 5.7: Illustration of the ratio of long-time and short-time self-diffusion coefficients of tracer particles D_S^L/D_S^S determined for binary mixtures with varying tracer number density $^1\rho_{PS3}$ (left) and with varying matrix number density $^1\rho_{matrix}$ (right). A decrease of $^1\rho_{PS3}$ down to a fourth of the original density shows no significant influence on D_S^L/D_S^S , while a decline of $^1\rho_{matrix}$ leads to an increase of D_S^L/D_S^S , which is strong at first and becoming weaker with decreasing matrix number density. The addition of 10^{-3} M KCl largely enhances D_S^L/D_S^S .

This qualitative tendency is confirmed by the results for the long-time self-diffusion coefficients presented in table 5.2. There, D_S^L is increased from $0.20 \times 10^{-12} \text{ m}^2\text{s}^{-1}$, for the original matrix number density, by a factor of two to $0.40 \times 10^{-12} \text{ m}^2\text{s}^{-1}$ for the sample with 60 % of the original number density of pTFEA VI. Simultaneously, the short-time self-diffusion coefficient seems to be decreased by dilution of the matrix component. However, with a range from $0.59 \times 10^{-12} \text{ m}^2\text{s}^{-1}$ to $0.52 \times 10^{-12} \text{ m}^2\text{s}^{-1}$, this effect is much less pronounced.

A graphical illustration of the impact of matrix dilution on the dynamics of the tracer particles is presented on the right side of Fig. 5.7. The ratio D_S^L/D_S^S grows quickly first, then successively slower, with decreasing matrix number density. At very low number densities of the matrix, in the order of magnitude of $^1\rho_{PS3,0}$, this ratio is expected to reach the value 1, as there the diffusive behaviour of the tracer component should be similar to the one of the investigated sample of pure, highly diluted PS3, such that $D_S^L \approx D_S^S$. This case, however, is not reviewed here. Instead, the effect of electrostatic screening by stray ions is illustrated for a sample with 80 % of the original matrix number density, that contains 10^{-3} M KCl. D_S^S and D_S^L of this sample are also presented in table 5.2. It is obvious, that the short-time diffusion is only little influenced related to the sample with the same matrix number density without stray ions. The long-time self-diffusion coefficient, however, is strongly increased due to electrostatic screening. Thus, by the presence of stray ions, D_S^L/D_S^S is elevated by a third of its value without added KCl.

With regard to the dynamical freezing criterion, that is introduced in section 2.3.2, the tracer component in all systems investigated in this section is characterised as distinctly apart from any freezing transition, as $D_S^L/D_S^S \gg 0.098$ holds for the self-diffusion of PS3 in each mixture under investigation.

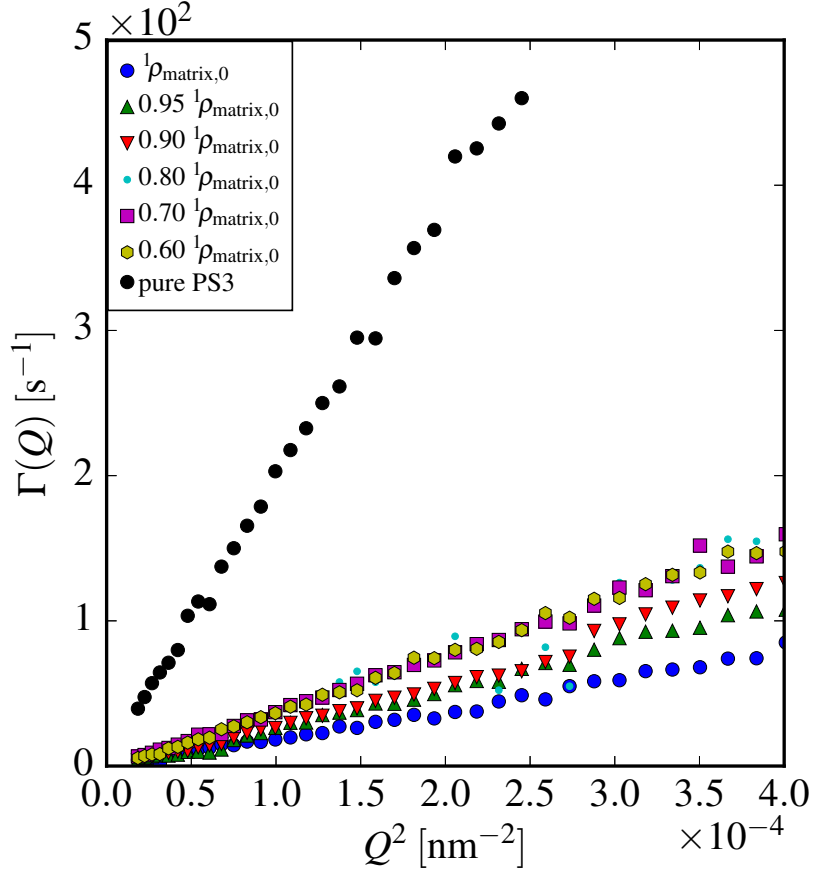


Fig. 5.8: Magnification of the low Q region of the lower right graphic of Fig. 5.6, presenting the long-time relaxation rates $\Gamma(Q)$ determined for binary mixtures with varying matrix number density ${}^1\rho_{\text{matrix},0}$. A tendency of an increased slope with decreasing ${}^1\rho_{\text{matrix}}$ is apparent, indicating an enhanced long-time self-diffusion of the tracer particles.

5.1.2 Brownian Dynamics simulations of tracer self-diffusion in a homo-colloidal matrix

Two assumptions are essential for the experimental investigations of tracer self-diffusion in the prepared mixtures of PS3 and pTFEA VI in section 5.1.1. First, the scattered intensity in the performed light scattering experiments must originate only from the tracer particles. Scattering functions obtained from SLS experiments provide evidence, that this condition is well fulfilled by the prepared binary mixtures. Secondly, the regime in the delay time τ , that is used as the basis for the investigation of long-time diffusion, has to be sufficiently larger than the structural relaxation time and must not be governed by noise. To enable a verification of the experimental results for self-diffusion of tracer particles in a binary mixture with a homo-colloidal matrix, Brownian Dynamics simulations are performed.

The methodical basics are described in section 3.5. Since a limited number of 8192 particles is simulated in order to restrict the computational effort to a reasonable extent, the experimental ratio of number densities of 1:200 of PS3 and pTFEA VI particles is not exactly realisable in the performed simulations to assure appropriate statistical certainty

for the tracer component. Instead, three different compositions of 10:90, 5:95 and 1:99 are modelled as approximations, keeping in mind the discrepancy to the experimental ratio of tracer and matrix component.

Table 5.3 summarises the parameters different from or complementing the standard simulation parameters mentioned in section 3.5, the subscripts A indicating polystyrene and B indicating pTFEA VI properties. The particle number density ratios of PS3 and pTFEA VI are adjusted according to the three different simulation compositions above. $Z_{\text{eff},B}$ represents an approximative value referring to the charge number of the investigated single component system of pTFEA VIb (cf. table 4.3). $Z_{\text{eff},A}$ is adjusted as a compromise between realising a similar surface charge density for PS3 as for the matrix particles and restricting $Z_{\text{eff},A}$ to a value known to be adequate for charged particles.

Table 5.3: Particle diameters σ_i , numbers of surface charges $Z_{\text{eff},i}$ and total colloidal number density ${}^1\rho_{\text{total}}$ for BD simulation of PS3 tracers in a pTFEA VI matrix. Dynamic viscosity η and permittivity ε_r are adjusted for a water/glycerol dispersion medium with a refractive index $n_m = 1.3945$, corresponding to a glycerol mass ratio of 47.5 %. Subscripts A and B denote properties of PS3 and pTFEA VI, respectively.

σ_A [nm]	σ_B [nm]	$Z_{\text{eff},A}$	$Z_{\text{eff},B}$	${}^1\rho_{\text{total}}/10^{18}$ [m ⁻³]	η [Pa·s]	ε_r
212	112	400	160	13.99	0.0053	66.41

The total colloidal particle number density ${}^1\rho_{\text{total}}$ is a calculated value corresponding to dilution of the aqueous pTFEA VI dispersion with a glycerol mass ratio of 47.5 %, that is realised in the experimental mixtures, starting from the number density of pTFEA VIa (cf. table 4.2) and also taking into account the addition of PS3. The dynamic viscosity η and relative permittivity ε_r are adjusted to represent the experimental water/glycerol dispersion medium as well.

As described in section 3.5.2, the three independent simulations are initiated from a bcc lattice and are first modelled until the structural equilibrium is reached, i. e., pair distribution functions of several subsequent simulation runs do not differ significantly. For the performed simulations this stage is reached after 1.5×10^5 to 1.8×10^5 simulation steps, which corresponds to simulated timespans between 300 ms and 360 ms. Subsequently, the equilibrium dynamics is simulated by a single run of 10^5 steps, i. e., a simulated time of 200 ms. From the particle trajectories the mean squared displacement (MSD) of each particle class over this timespan is calculated. Fig. 5.9 presents a compilation of these MSDs. The designation in that figure follows "TracerXX" and "MatrixYY", respectively, where "XX" and "YY" give the percentage molar ratios of the components.

For a better display of the data for tracer and matrix components, a half-logarithmic presentation is chosen. It can be easily recognised, that the mean squared displacements of the tracer particles are roughly a factor 2 smaller than those of the corresponding matrix particles, as expected from the ratio of Stokes-Einstein diffusion coefficients $D_{0,i}$ for the given particle sizes. The short-time behaviour of each displayed MSD trivially describes the respective $D_{0,i}$. However, in the long-time limit, the presented MSDs enable an evaluation of the tracer self-diffusion without disturbances by noise at even higher delay times than field autocorrelation functions from DLS (cf. Fig. 5.6). According to eq. (2.20), D_S^L can be obtained in a given time interval. For the example $g_1(\tau)$ -function displayed in Fig. 5.6 the fitting interval ranges $6 \text{ ms} \leq \tau \leq 23 \text{ ms}$, which is not automatically the same for all autocorrelation functions at different Q , as the intervals are

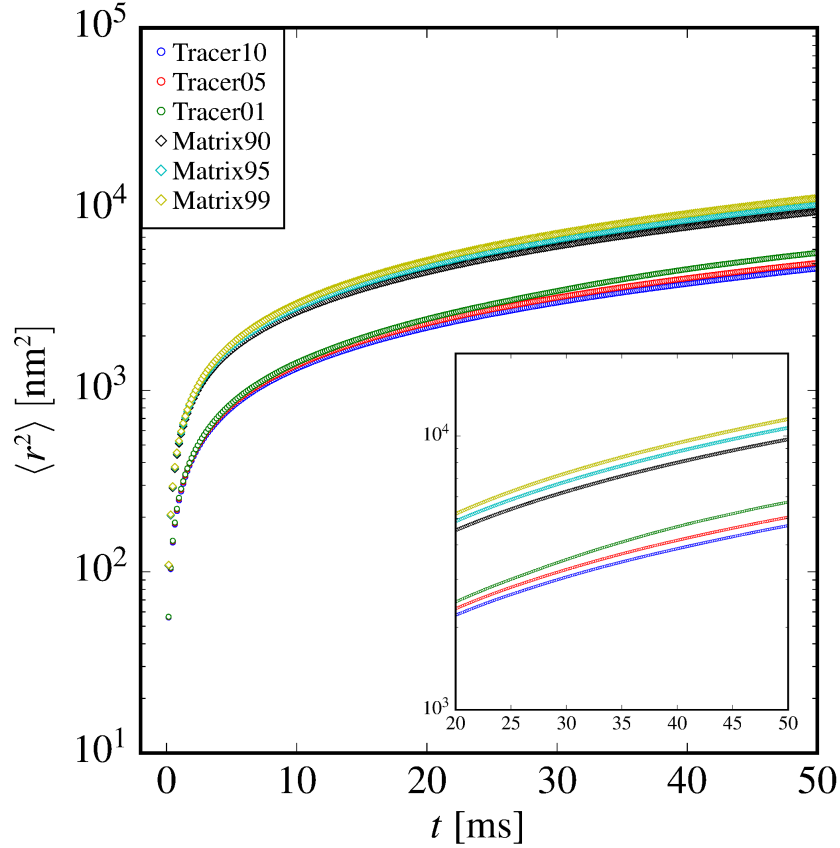


Fig. 5.9: Mean squared displacements $\langle r^2 \rangle$ of tracer and matrix particles determined from trajectories obtained by BD simulations of binary mixtures with three different compositions. Graphs are labelled with "TracerXX" and "MatrixYY", where "XX" and "YY" give the percentage molar ratios of the respective component.

dynamically adjusted to circumvent noisy experimental data of the correlation functions. Nonetheless, this interval in the simulated time t shall serve as one benchmark for the investigation of long-time self-diffusion from BD simulation. As a comparison, the interval $6 \text{ ms} \leq t \leq 50 \text{ ms}$ is employed to examine, whether significant changes occur at a higher timespan. Table 5.4 gives an overview of the obtained results.

Table 5.4: Long-time self-diffusion coefficients of PS3 tracers obtained from BD simulations of binary mixtures with different compositions. $D_S^{L,23}$ and $D_S^{L,50}$ correspond to upper time limits of 23 ms and 50 ms, respectively, for the determination of the long-time self-diffusion coefficients.

Molar ratio of PS3	10 %	5 %	1 %
$D_S^{L,23}/10^{-13} [\text{m}^2\text{s}^{-1}]$	0.91	0.98	1.06
$D_S^{L,50}/10^{-13} [\text{m}^2\text{s}^{-1}]$	0.85	0.92	1.01

$D_S^{L,23}$ denotes the long-time self-diffusion coefficient of PS3 particles obtained from the interval $6 \text{ ms} \leq t \leq 23 \text{ ms}$, $D_S^{L,50}$ is its analogue for $6 \text{ ms} \leq t \leq 50 \text{ ms}$. Clearly, the shorter time interval delivers larger values for the long-time self-diffusion coefficient than the interval with an upper limit of 50 ms. Thus it must be deduced, that the upper time limit available for long-time evaluation of the experimental field autocorrelation functions does not exactly describe the time limit necessary for the determination of D_S^L . The relative discrepancies between the determined corresponding $D_S^{L,23}$ and $D_S^{L,50}$ amount to around five to seven percent. Hence, the experimental results for D_S^L from DLS can still be rated as a good approximation.

The remaining deviations between the long-time diffusion coefficients from simulation and experiment of less than half an order of magnitude presumably have to be ascribed to the a priori different compositions of the experimental and simulated binary mixtures. A clear tendency of accelerated long-time diffusion is recognised from table 5.4 with decreasing molar ratio of PS3. This effect is also identified for the matrix component from the corresponding MSDs presented in Fig. 5.9. The origin of this is explainable by the exchange of the larger PS3 particles, which also exhibit more than twice as much surface charges, with smaller and less charged pTFEA VI spheres. Hence, more space is available for quasi-free particle motion and less repulsion is realised, which causes a slight increase of D_S^L . Whether the reduction from 1% to about 0.5% molar content of the tracer component suffices to overcome half an order of magnitude in D_S^L is to be critically questioned. A further resolution of this matter, however, is beyond the scope of this work.

A very intuitive way of comparing the results obtained from DLS experiments and BD simulations is available in terms of the time-dependent self-diffusion coefficient $D_S(t)$. Thereby, not only the limiting cases of D_S^S and D_S^L , but the temporal development over intermediate times is presented as well. Employing the mean squared displacements calculated from the trajectories, that are determined for each particle throughout the simulations, a time dependency is readily obtainable via a Verlet algorithm as described by eq. (3.12) in section 3.5. The field autocorrelation function $g_1(Q, \tau)$ resulting from a dynamic light scattering experiment also comprises the time-dependency of the diffusive motion of the investigated colloidal particles. Hence, dividing the time domain, ranging from the first time increment up until the identified long-time limit, into several intervals and determining the slopes of the correlation function in these regions, a time-dependent relaxation rate $\Gamma(Q, t)$ and thus the time-dependent self-diffusion coefficient are accessible. Due to the reciprocal sensitivity of the scattering vector to sizes and distances in real space and the defined polydispersity of a real colloidal dispersion, results for $D_S(t)$ obtained in this way might exhibit deviations, depending on the scattering vector at which the correlation function is determined. As a preferably representative example, $g_1(\tau)$ for an intermediate scattering vector $Q = 2.308 \times 10^{-2} \text{ nm}^{-1}$ ($\vartheta \approx 89^\circ$) obtained from the binary stock mixture of PS3 and pTFEA VI with number densities ${}^1\rho_{\text{PS3},0}$ and ${}^1\rho_{\text{matrix},0}$ is selected. Fig. 5.10 displays the time-dependent tracer self-diffusion coefficients obtained for the three simulated compositions and the above mentioned experimental system in comparison.

The self-diffusion functions in Fig. 5.10 are displayed in the range $10^{-2} \text{ ms} \leq t \leq 2 \times 10^1 \text{ ms}$. This span is limited at short times due to the size of the simulation time step and at large times caused by noise in the field autocorrelation function. Each $D_S(t)$ is normalised to $D_S(0)$, which in this case denotes the value for the first argument of each dataset. Therefore, those values surpassing 1.0 for the experimental $D_S(t)$ are unphysical and most possibly originate from statistical uncertainties in the experimental data for the

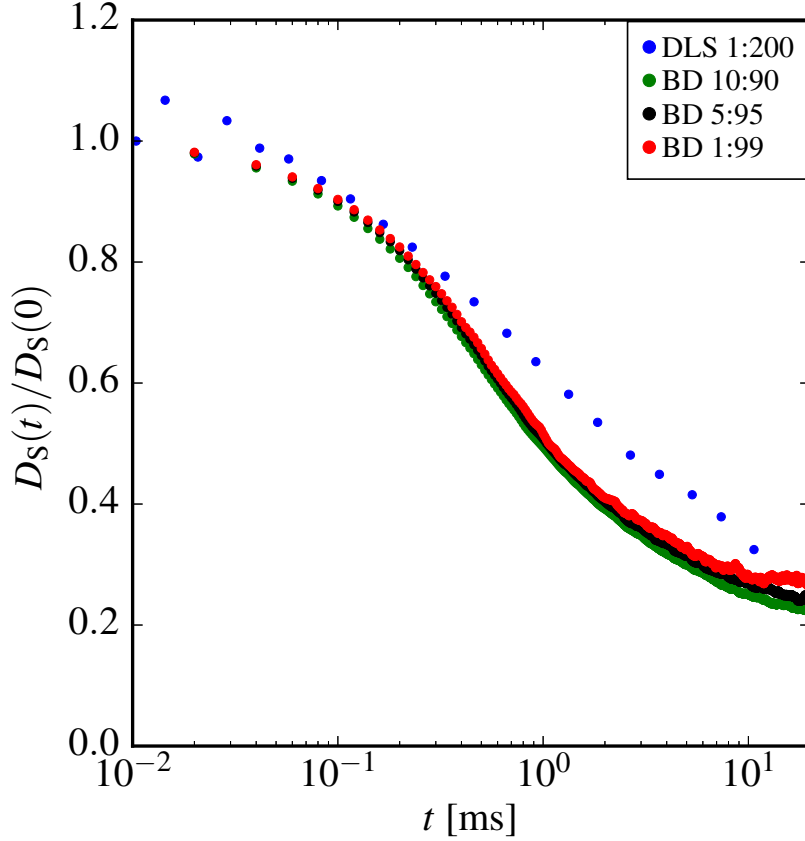


Fig. 5.10: Time-dependent self-diffusion coefficients $D_S(t)$ of PS3 tracers in a matrix of pT-FEA VI determined by DLS experiments and BD simulations. Each $D_S(t)$ is normalised to its starting value $D_S(0)$. The key gives the molar ratio of the components of the mixture as A : B, where A denotes the tracers and B the matrix.

field autocorrelation function obtained by DLS. Nonetheless, it can be generally acknowledged, that excellent agreement of the short-time diffusion behaviour is observed. In the long-time domain, successively better compliance is reached the closer the simulated molar composition becomes relative to the experimental ratio of 1:200. For the simulation set with the least tracer content of 1:99, $D_S(t)$ almost coincides with the DLS data for the experimental system at $t \geq 10^1$ ms. As shown before, absolute long-time self-diffusion exhibits deviations of less than half an order of magnitude between simulation and experiment. This leads to the conclusion, that the cause of these deviations is of systematic character and influences the diffusion behaviour over the whole time range, and as such is eliminated by a relative data treatment, e. g., the normalised presentation in Fig. 5.10. Despite this interesting observation, simulation and experiment show significant discrepancies in $D_S(t)$ at intermediate times, the origin of which is not further resolved in this work.

The approach of verification of the results for long-time self-diffusion of a tracer component in a homo-colloidal matrix determined by DLS experiments via BD simulations appears to be mainly successful, although some issues have to be left unanswered. Further studies employing other experimental techniques, such as fluorescence recovery after

photobleaching (FRAP) [110, 117] and pulsed field gradient NMR [16], or theoretical calculations [74] could be conducted to verify the results for the long-time self-diffusion behaviour investigated here. The application of such techniques, however, is beyond the scope of this work.

5.2 Binary mixtures with similar number densities

5.2.1 Intermediate scattering functions obtained by light scattering experiments and Brownian Dynamics simulations

In contrast to investigations of self-diffusion in binary mixtures of charged colloidal particles, the collective dynamics of interacting, charge-stabilised colloids in mixtures of two different components is not systematically studied, yet. This is because the partial dynamic structure factors $S_{ij}(Q, t)$ of such a mixture, also designated as partial intermediate scattering functions, are readily accessible neither by experiment nor by simulation. With the refractive index tunability of the colloidal copolymer systems prepared in this work, however, it is comparably easy to combine two colloidal species with defined particle sizes and interaction parameters as well as similar number densities and selectively match the refractive index of the dispersion medium to one of the colloidal particle species. The scattering power of that index-matched component then vanishes. If the refractive indices of the combined colloidal particle classes A and B are sufficiently apart, the partial intermediate scattering function $S_{AA}(Q, t)$, describing correlations between particles of class A, is available by means of DLS experiments at $n_m = n_B$ and $S_{BB}(Q, t)$ can be obtained analogously from a dispersion with $n_m = n_A$. Knowing $S_{AA}(Q, t)$ and $S_{BB}(Q, t)$, it is also possible to determine $S_{AB}(Q, t)$ from a third sample of the same mixture with $n_A \neq n_m \neq n_B$. This section shall give an impression of how the newly developed colloidal copolymer dispersions may facilitate experimental access to partial intermediate scattering functions of a colloidal binary mixture with similar number densities of the two components and also illustrate the critical importance of exact index-matching.

For this purpose, a binary mixture composed of pOFPA III and pTcB-30 II is prepared. Referring to table 4.1, pOFPA III exhibits particles of $\sigma_A = 212$ nm in diameter with a refractive index of $n_A = 1.380$, while pTcB-30 II consists of particles with $\sigma_B = 100$ nm and $n_B = 1.436$. The liquid-like order of homo-colloidal dispersions formed by self-organisation of both pure species is characterised in section 4.4. From table 4.2 it becomes clear, that the number densities of these two samples are slightly different and comparably low. For the preparation of the binary mixture, the particle concentration of both components is increased by evaporation of parts of the dispersion medium water, utilising a rotary evaporator. Subsequently, different amounts of the concentrated dispersions are combined, as to result in a binary mixture with very similar number densities of pOFPA III and pTcB-30 II. Glycerol is added to that mixture, until a refractive index $n_m = 1.377$ of the dispersion medium is adjusted, which corresponds to a glycerol mass ratio of 35 % [93]. A deliberate, slight mismatch of n_m and n_A is realised. In this way it is illustrated later on, that the appropriate attention in index-matching is crucial in order to obtain reliable results for the partial intermediate scattering functions by means of DLS. A mixed-bed ion exchanger is added to the sample, which is thoroughly shaken and left to stand for two weeks to assure minimisation of the ionic strength as well as structural and dynamical equilibration of the sample. A DLS experiment is performed using the equilibrated sample, following the protocol described in section 3.4.3. The result is a partial collective short-

time diffusion coefficient $D_{\text{eff, BB}}(Q)$ for the pTcB-30 II particles, which due to $n_m \approx n_A$ contains remaining contributions of AA and AB correlations. Normalisation of the short-time self-diffusion coefficient D_0 for pTcB-30 II, determined before (cf. table 4.1), to $D_{\text{eff, BB}}(Q)$ leads to the short-time limit of the partial intermediate scattering function $S_{\text{BB}}(Q, 0) = D_0/D_{\text{eff, BB}}(Q)$. The experimentally determined approximation $S_{\text{BB}}(Q, 0)$ is presented in Fig. 5.11.

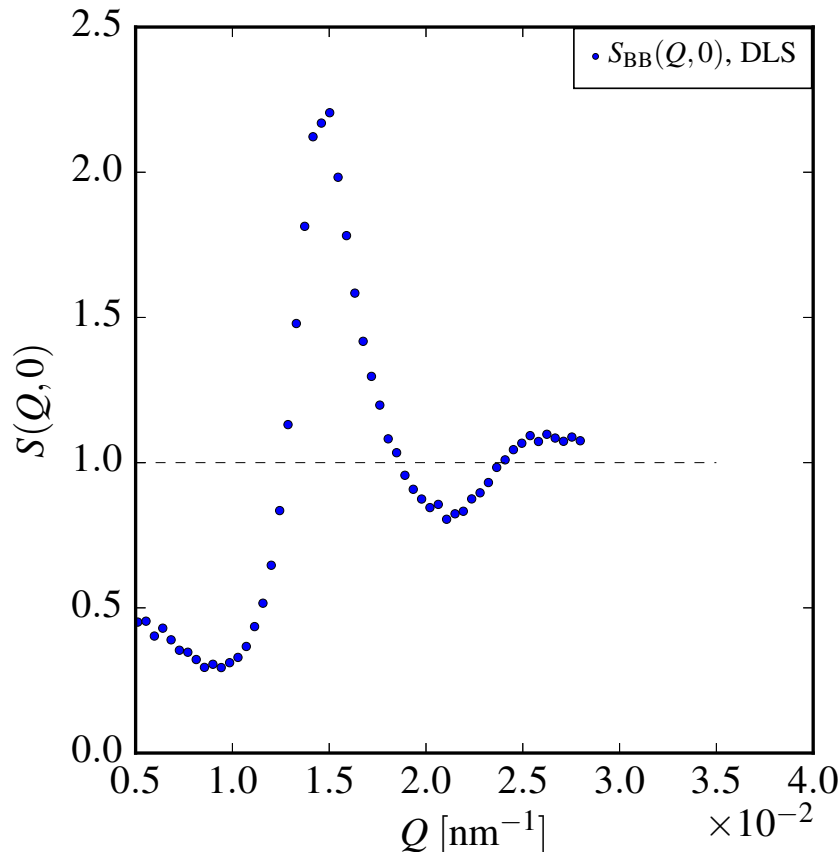


Fig. 5.11: Approximation of the short-time limit of the partial intermediate scattering function $S_{\text{BB}}(Q, 0)$ of pTcB-30 II particles in a binary mixture with pOFPA III particles. Due to a deliberate mismatch between refractive indices of the water/glycerol dispersion medium, $n_m = 1.377$, and of pOFPA III particles, $n_A = 1.380$, contributions of AA and AB correlations to the presented partial intermediate scattering function are assumed.

Because $t \rightarrow 0$, the partial intermediate scattering function equals the partial static structure factor of that correlation, such that $S_{\text{BB}}(Q, 0) = S_{\text{BB}}(Q)$. Thus, a pronounced liquid-like order of pTcB-30 II in the investigated binary mixture is indicated. However, as explained above, Fig. 5.11 displays only an approximation of $S_{\text{BB}}(Q, 0)$, additionally containing remaining contributions of AA and AB correlations, due to incomplete index-matching of pOFPA III. Because the number densities of both components are rather high, these contributions cannot be neglected. This distinguishes the present system from the binary mixture with trace amounts of PS3 investigated in section 5.1.1, where the disregard of matrix component influences on the scattering signal has been proven

legitimate despite a slight index-mismatch between dispersion medium and pTFEA VI matrix, due to the much larger scattering power of the tracer component polystyrene.

The average scattering intensity $I(Q)$ detected in a static scattering experiment on a binary mixture of two classes of spherical particles is generally defined as

$$I(Q) = {}^1\varrho_A V_A^2 P_A(Q) (n_m - n_A)^2 \cdot S_{AA}(Q) + {}^1\varrho_B V_B^2 P_B(Q) (n_m - n_B)^2 \cdot S_{BB}(Q) + \sqrt{{}^1\varrho_A {}^1\varrho_B V_A V_B} \sqrt{P_A(Q) P_B(Q)} (n_m - n_A) (n_m - n_B) \cdot S_{AB}(Q), \quad (5.1)$$

with the number densities ${}^1\varrho_i$, particle volumes V_i , form factors $P_i(Q)$ and refractive indices n_i for each of the two components A and B. n_m denotes the refractive index of the dispersion medium and $S_{ij}(Q)$ designate the static structure factors for each of the three possible particle correlations AA, BB and AB. Assuming $n_m = n_A$ for an experimental binary mixture, one would detect an intensity defined by only the second addend of (5.1). To obtain $S_{BB}(Q)$, $I(Q)$ would be normalised to the intensity $I'(Q) = {}^1\varrho'_B V_B^2 P_B(Q) (n'_m - n_B)^2$ detected from a dilute sample of component B.

The small mismatch between $n_m = 1.377$ and $n_A = 1.380$, in case of the experimental sample presented above, thus leads to additional contributions not originating from the BB correlation. The effective structure factor is then described by the normalised scattering function

$$\begin{aligned} \frac{I(Q)}{I'(Q)} &= \frac{{}^1\varrho_A V_A^2 P_A(Q) (n_m - n_A)^2 \cdot S_{AA}(Q)}{{}^1\varrho'_B V_B^2 P_B(Q) (n'_m - n_B)^2} + \frac{{}^1\varrho_B V_B^2 P_B(Q) (n_m - n_B)^2 \cdot S_{BB}(Q)}{{}^1\varrho'_B V_B^2 P_B(Q) (n'_m - n_B)^2} \\ &+ \frac{\sqrt{{}^1\varrho_A {}^1\varrho_B} V_A V_B \sqrt{P_A(Q) P_B(Q)} (n_m - n_A) (n_m - n_B) \cdot S_{AB}(Q)}{{}^1\varrho'_B V_B^2 P_B(Q) (n'_m - n_B)^2} \\ &= \frac{{}^1\varrho_A V_A^2 P_A(Q) (n_m - n_A)^2}{{}^1\varrho'_B V_B^2 P_B(Q) (n'_m - n_B)^2} \cdot S_{AA}(Q) + \frac{{}^1\varrho_B (n_m - n_B)^2}{{}^1\varrho'_B (n'_m - n_B)^2} \cdot S_{BB}(Q) \\ &+ \sqrt{\frac{{}^1\varrho_A P_A(Q)}{{}^1\varrho'_B P_B(Q)}} \cdot \frac{V_A}{V_B} \cdot \frac{(n_m - n_A) (n_m - n_B)}{(n'_m - n_B)^2} \cdot S_{AB}(Q). \end{aligned} \quad (5.2)$$

All information contained in eq. (5.2) regarding the particle number densities, particle volumes, refractive indices and form factors are known from chapter 4 and from the composition of the investigated binary mixture. The particle form factors of pOFPA III and pTcB-30 II are also known from SLS experiments on dilute samples of these systems, as they have been employed for the determination of static structure factors of corresponding liquid-like ordered single component systems in section 4.4. The contributions that are missing to fully comprehend the shape of the experimental approximation of $S_{BB}(Q, 0)$ in Fig. 5.11, are the partial static structure factors $S_{AA}(Q)$, $S_{BB}(Q)$, and $S_{AB}(Q)$. For the determination of these, the experimental binary mixture is modelled via BD simulations.

The simulation procedure is described in section 3.5.2. Particle diameters and numbers of effective surface charges are adjusted to the most probable particle sizes and the charge numbers determined for the single component systems of pOFPA III and pTcB-30 II (cf. tables 4.1 and 4.3). The overall particle number density ${}^1\varrho_{\text{total}} = 10.07 \times 10^{18} \text{ m}^{-3}$ is calculated in reference to the composition of the binary mixture investigated by DLS. This also leads to the number density ratios ${}^1\varrho_A / {}^1\varrho_{\text{total}} = 0.4895$ for pOFPA III and

${}^1Q_B/{}^1Q_{\text{total}} = 0.5105$ for pTcB-30 II. The water/glycerol dispersion medium is modelled via a dynamic viscosity $\eta = 2.7926 \times 10^{-3} \text{ Pa} \cdot \text{s}$ and a permittivity $\varepsilon_r = 70.8$. Starting from a bcc lattice the binary mixture is simulated, until after 4×10^5 steps, corresponding to a simulated time of 800 ms, the structural equilibrium is identified. The determined partial pair distribution functions $g_{ij}^{(2)}(r/\sigma)$ in dependence on the reduced distance r/σ , with $\sigma = \sigma_A$, are displayed on the left side in Fig. 5.12.

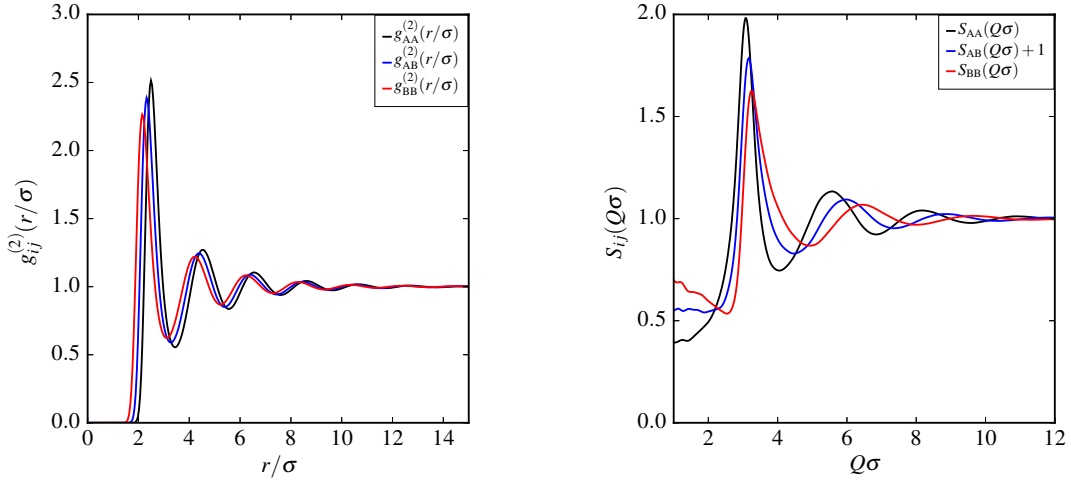


Fig. 5.12: Left: Partial pair distribution functions $g_{ij}^{(2)}(r/\sigma)$ obtained by BD simulations of a binary mixture corresponding to the experimentally investigated system. Right: Partial static structure factors $S_{ij}(Q\sigma)$ determined by Fourier-Bessel transform of $g_{ij}^{(2)}(r/\sigma)$. Here, $\sigma = \sigma_A$, i. e., the particle diameter of pOFPA III. For better display, the mixed correlation structure factor is presented as $S_{AB}(Q\sigma) + 1$.

Via Fourier-Bessel transform according to (2.9), the partial static structure factors $S_{ij}(Q\sigma)$, again with $\sigma = \sigma_A$, characterising the simulated binary mixture are obtained, as presented on the right side in Fig. 5.12. $S_{AB}(Q\sigma)$ would normally oscillate around 0, such that 1 is added to the structure factor of this correlation for better display. Conveniently, in this way all three possible correlations can be described separate from another, although by means of scattering experiments only a linear combination of $S_{AA}(Q\sigma)$, $S_{BB}(Q\sigma)$, and $S_{AB}(Q\sigma)$ is accessible. Obviously, $S_{BB}(Q\sigma)$ is significantly smaller than the approximate structure factor obtained by DLS.

Employing eq. (5.2) with the known experimentally determined quantities and the structure factors from BD, the effective structure factor $I(Q)/I'(Q)$ displayed in Fig. 5.13 results, where $S_{BB}(Q, 0)$ obtained by simulation is also presented for comparison.

Excellent agreement between the calculated linear combination and the data obtained from the DLS experiment is noted around the coordination maximum. Hence, the partial structure factor obtained from light scattering is verified to comprise significant contributions of AA and AB correlations due to incomplete index-matching of pOFPA III, i. e., component B, although the difference of $n_m = 1.377$ and $n_A = 1.380$ seems comparably small. In the limit $Q \rightarrow 0$ the approximation of $S_{BB}(Q, 0)$ from experiment is elevated, which is ascribed to the polydispersities $p_A = 0.091$ and $p_B = 0.108$ of pOFPA III and pTcB-30 II (cf. section 4.4), since polydispersity is a well known reason for rising compressibility as visible in $S(Q \rightarrow 0, 0)$. $I(Q)/I'(Q)$ is calculated assuming ideally uniform particles.

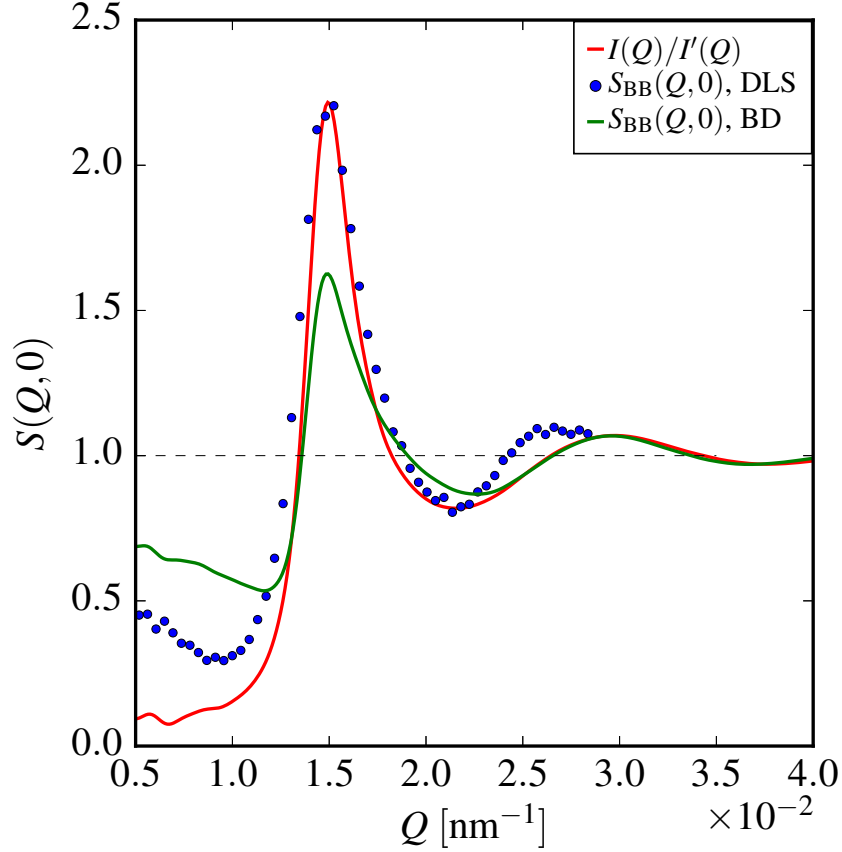


Fig. 5.13: Comparison of the static intermediate scattering functions $S_{BB}(Q,0)$ determined by DLS and BD simulation. Calculation of the effective structure factor $I(Q)/I'(Q)$ according to eq. (5.2) proves that, due to incomplete index-matching of pOFPA III, actually a linear combination of $S_{AA}(Q,0)$, $S_{AB}(Q,0)$, and $S_{BB}(Q,0)$ is detected by DLS. Hence the imperative of exact index-matching for the determination of partial scattering functions in mixtures is clarified.

These results indicate the potential of the novel colloidal (co)polymer dispersions with tunable refractive indices, which are prepared in this work, for investigations of colloidal mixtures with pronounced liquid-like order due to self-organisation. Simultaneously however, the imperative of exact index-matching one component for the determination of the sole partial scattering function of the other one is explicitly stressed.

Due to short-time fitting of the field autocorrelation functions obtained from DLS, until now only the spatial dependency of the intermediate scattering function has been discussed in this section, while temporal fluctuations are not considered in the static limit $t \rightarrow 0$. In addition to the time averaged structure, the information about is given by static structure factors $S_{ij}(Q) \equiv S_{ij}(Q,0)$, BD is capable to analyse the temporal dependency of the partial intermediate scattering functions $S_{ij}(Q,t)$.

Starting from the equilibrium structure reached after 4×10^5 simulation steps, a run of 3×10^5 time steps, i. e., a simulated time of 600 ms, is performed to serve as a basis for the investigation of the collective diffusion behaviour of the simulated mixture. As indicated in section 3.5, a sophisticated, highly parallel algorithm developed for this specific task is

employed to calculate the partial distinct space-time pair distribution functions $g_{ij}^{(2)}(r, t)$ for correlations between particles of the same particle class and different particle classes. Therein, the positions of two respective particles out of the ensemble of 8192 simulated particles are correlated at each of the 3×10^5 time steps. This is performed for each possible pair of particles corresponding to the respective correlation AA, BB, or AB. $g_{AA}^{(2)}(r, t)$, $g_{BB}^{(2)}(r, t)$, and $g_{AB}^{(2)}(r, t)$ then exhibit the canonical average of the corresponding space-time correlations over all particles and all time differences. In Fig. 5.14 a qualitative 3D presentation of such a space-time pair distribution function is displayed.

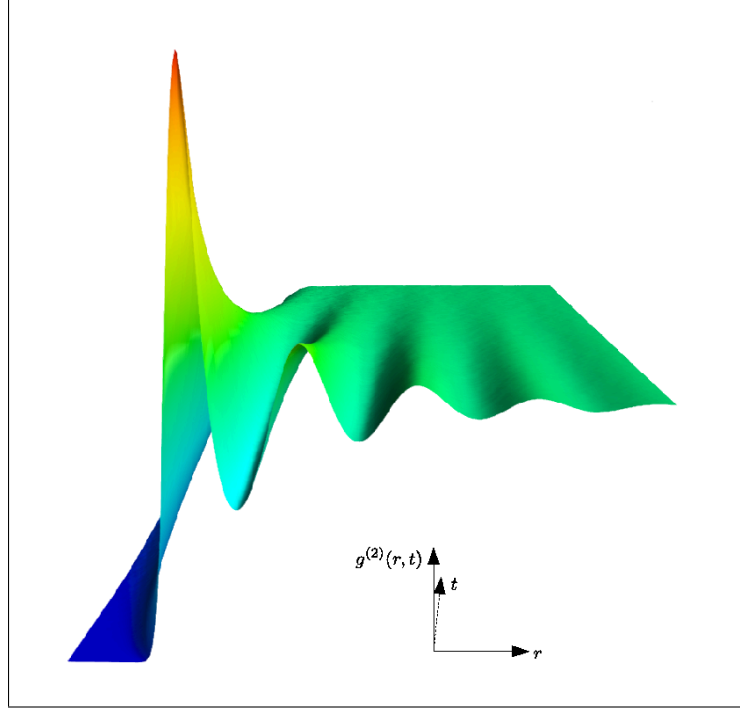


Fig. 5.14: Qualitative presentation of a typical space-time pair distribution function $g^{(2)}(r, t)$. The representation $g^{(2)}(r, t = 0)$ vs. r exhibits the damped oscillation known for the static pair distribution function of a liquid-like ordered system. In the representation $g^{(2)}(r, t)$ vs. t , a temporal decay indicates the progressive loss of correlation between two particles over time at a given particle distance r .

In the representation $g^{(2)}(r, t = 0)$ vs. r the typical damped oscillation of a static pair distribution function of a liquid structure is observed. At larger times minima and maxima of the distribution function are progressively washed out, indicating the loss of correlation between two particles over time. In the representation $g^{(2)}(r, t)$ vs. t , this temporal decay is noticed by a smooth damping, particularly well to be observed at the distance r_{\max} of the global maximum of the distribution. Spatial Fourier-Bessel transform of the $g_{ij}^{(2)}(r, t)$ results in the partial intermediate scattering functions $S_{ij}(Q, t)$. A quantitative view on the loss of correlation between the particles of the simulated binary mixture described by these functions is presented in Fig. 5.15, where $S_{ij}(Q\sigma, t)$ are displayed with $\sigma = \sigma_A = 212$ nm. Minor fluctuations at small $Q\sigma$ are unphysical artefacts due to slight truncation effects that could not be avoided during Fourier-Bessel transform.

As to be expected, the correlations between particles of the same class, AA and BB, show damped oscillations around 1 with increasing Q , due to the self contribution of the correlation remaining at large scattering vectors. In case of correlations between

different particle classes, AB, the intermediate scattering function reaches a value of 0 at large Q , since there is no self-part for AB correlations. As already noticeable from the static structure factors on the right in Fig. 5.13, which are identical to the intermediate scattering functions at $t = 0$, the heights of the coordination maxima of the intermediate scattering functions $S_{ij,\max}(Q\sigma, t)$ are not equal. Indeed, they exhibit a measure of the strength of the respective correlation. Considering this, it is a reasonable observation, that the maxima relative to their baseline relate to one another as $S_{AA,\max}(Q\sigma, t) - 1 = 0.98 > S_{AB,\max}(Q\sigma, t) = 0.79 > S_{BB,\max}(Q\sigma, t) - 1 = 0.63$, due to the larger number of surface charges defined in the simulation for pOFPA III ($Z_{\text{eff,A}} = 212$) vs. pTcB-30 II ($Z_{\text{eff,B}} = 145$).

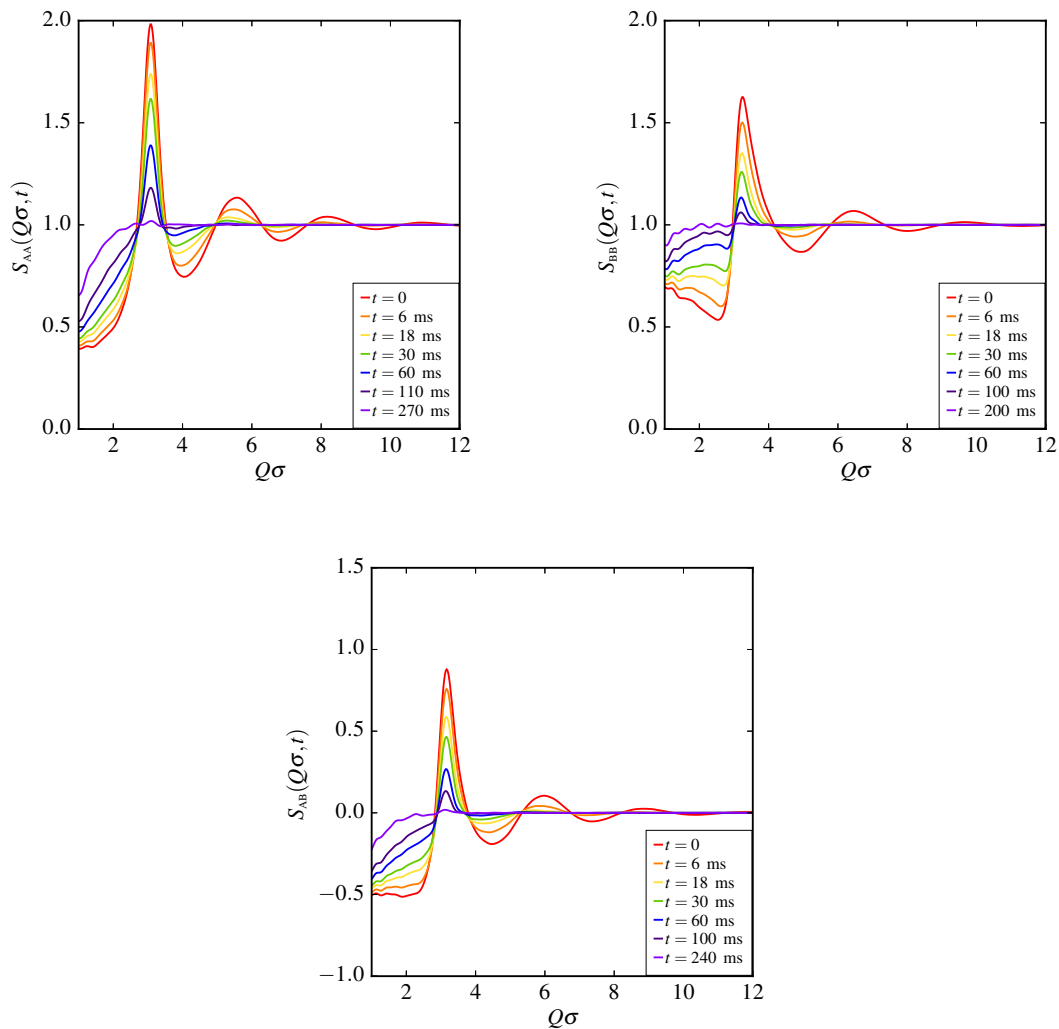


Fig. 5.15: Time-dependencies of the partial intermediate scattering functions $S_{ij}(Q\sigma, t)$. These result from Fourier-Bessel transform of partial space-time pair distribution functions $g_{ij}^{(2)}(r/\sigma, t)$ obtained by BD simulations of the experimental binary mixture of pOFPA III and pTcB-30 II. The reduced scattering vector $Q\sigma$ is displayed with $\sigma = \sigma_A = 212$ nm. Relaxation times of the intermediate scattering functions scale with the strength of correlation quantified by the global maxima of $S_{ij}(Q\sigma, t)$ relative to the corresponding baseline.

Similar to the effects discussed for the qualitative illustration of $g_{ij}^{(2)}(r, t)$ in Fig. 5.14,

for increasing correlation times t a progressive damping is observed for the intermediate scattering functions as well, indicating the loss of correlation between two particles over time. Due to the elevated viscosity $\eta = 2.7926 \times 10^{-3} \text{ Pa} \cdot \text{s}$ of the simulated water/glycerol dispersion medium, almost three times as large as for pure water, correlations are preserved for comparably long times. Interestingly, a complete relaxation is observed after significantly different times for the three partial intermediate scattering functions, with the corresponding relaxation times relating to each other as $t_{\text{rel.,AA}} = 270 \text{ ms} > t_{\text{rel.,AB}} = 240 \text{ ms} > t_{\text{rel.,BB}} = 200 \text{ ms}$. This sequence coincides both qualitatively and quantitatively with observations for the global maxima $S_{ij,\text{max}}(Q\sigma, t)$, such that it is assumed, that $t_{\text{rel.,ij}}$ scales with the strength of correlation, as expected according to the de Gennes relation (cf. eq. (2.21)).

Apparently, the intermediate scattering functions exhibit an increase in the limit $Q\sigma \rightarrow 0$ with rising correlation time, which is connected to the progressive loss of correlation, until in case of $S_{AA}(Q\sigma, t)$ and $S_{BB}(Q\sigma, t)$ only the self contribution of the correlation remains. For $S_{AB}(Q\sigma, t)$ there is no self contribution, such that the correlation function approaches 0 at large times.

Fig. 5.15 comprehensively describes the distinct space-time correlations in a binary mixture obtained by BD simulations on the basis of an experimental mixture of moderately concentrated dispersions of pOFPA III and pTcB-30 II. Simultaneously it is indicated by this section, that the newly developed colloidal (co)polymer systems readily provide access to structural as well as dynamical information in complex systems both by light scattering experiments and simulation techniques.

5.2.2 Systematic simulation study on influences of system parameters on the intermediate scattering function

The previous section has provided evidence, that BD simulations are a powerful and convenient tool for investigating mixtures of charged colloidal dispersions. Beyond the connection to structural and dynamical properties of such mixtures determined by means of light scattering experiments, simulations give a comparably easy access to much more systematic studies than would be possible with similar effort by experiment. In this section, the influences of the number density ratios, particle sizes and numbers of surface charges of the components in a realistic binary mixture of charged colloids as well as the influence of the temperature of the system on the partial intermediate scattering functions are systematically investigated.

First of all, a reference system is defined to serve as a benchmark for all further simulations. To assure the modelling of a realistic mixture, the relative number densities and particle sizes are adjusted according to the simulated mixture from the section before. However, the overall particle density is set to ${}^1\rho_{\text{total}} = 7.25 \times 10^{18} \text{ m}^{-3}$ and dynamic viscosity and relative permittivity are defined by the standard parameters according to section 3.5 for a dispersion medium of pure water. The numbers of surface charges of component A and B are somewhat increased, such that $Z_{\text{eff,A}} = 280$ and $Z_{\text{eff,B}} = 192$. Table 5.5 compiles the simulation parameters of the reference system for this section.

Table 5.5: Total colloidal number density ${}^1\rho_{\text{total}}$, relative number densities ${}^1\rho_i/{}^1\rho_{\text{total}}$, particle diameters σ_i and numbers of surface charges $Z_{\text{eff},i}$ defined for BD simulation of the reference system for systematic investigations of binary mixtures with similar number densities. Subscripts A and B denote properties of the corresponding component.

${}^1\rho_{\text{total}}/10^{18} [\text{m}^{-3}]$	${}^1\rho_{\text{A}}/{}^1\rho_{\text{total}}$	${}^1\rho_{\text{B}}/{}^1\rho_{\text{total}}$	$\sigma_{\text{A}} [\text{nm}]$	$\sigma_{\text{B}} [\text{nm}]$	$Z_{\text{eff,A}}$	$Z_{\text{eff,B}}$
7.25	0.4986	0.5014	212	100	280	192

18 simulations with variations of specific parameters, that can be divided into four sets, are performed with regard to this reference system. The four sets define changes in the number density ratio of the two components, the particle sizes, the numbers of surface charges, and the temperature of the surrounding and are correspondingly designated as Ratio{1...4}, Size{1...4}, Charge{1...4}, and Temp{1...6}. Changed parameters are compiled in tables 5.6 to 5.9, while remaining parameters for each respective simulation are left unchanged with regard to the reference system. Surface charges are adjusted with respect to the reasonable assumption, that the larger particles do not exhibit a smaller number of charges than the smaller particle species. Changes in temperature will influence the viscosity and permittivity of the dispersion medium, which is regarded for the corresponding simulations compiled in table 5.9.

Each of the 18 independent binary systems with varied parameters is simulated according to section 3.5.2 starting from a bcc lattice, until after 2.5×10^5 time steps the structural equilibrium is reached for each system. Subsequently, a dynamic simulation run is performed. For most of the simulations these runs exhibit 6×10^5 time steps, corresponding to a simulated time of 1.2 s. For some of the later dynamic runs the time step number has been reduced to 4×10^5 and even 10^5 , after results for the earlier dynamic runs revealed the velocity of collective dynamics in the simulated aqueous dispersion medium.

Table 5.6: Parameters of the first simulation set: variation of the number densities ${}^1\rho_A$ and ${}^1\rho_B$.

ID	${}^1\rho_A/{}^1\rho_{\text{total}}$	${}^1\rho_B/{}^1\rho_{\text{total}}$
Ratio1	0.2	0.8
Ratio2	0.4	0.6
Ratio3	0.6	0.4
Ratio4	0.8	0.2

Table 5.7: Parameters of the second simulation set: variation of particle diameters σ_A and σ_B .

ID	σ_A [nm]	σ_B [nm]
Size1	150	100
Size2	300	100
Size3	280	70
Size4	150	150

Table 5.8: Parameters of the third simulation set: variation of effective surface charges $Z_{\text{eff},A}$ and $Z_{\text{eff},B}$.

ID	$Z_{\text{eff},A}$	$Z_{\text{eff},B}$
Charge1	190	190
Charge2	300	150
Charge3	300	100
Charge4	320	80

Table 5.9: Parameters of the fourth simulation set: variation of temperature T , viscosity η and permittivity ϵ_r of the medium.

ID	T [K]	$\eta/10^{-3}$ [Pa·s]	ϵ_r
Temp1	303	0.7995	76.9
Temp2	323	0.5484	69.7
Temp3	348	0.3795	62.0
Temp4	368	0.2987	56.5
Temp5	278	1.5209	85.8
Temp6	283	1.3098	83.8

The partial, distinct space-time pair distribution functions $g_{ij}^{(2)}(r, t)$ are determined according to the algorithm introduced in the previous section and the partial intermediate scattering functions $S_{ij}(Q, t)$ are obtained by means of Fourier-Bessel transform. In all graphical illustrations of the partial intermediate scattering functions following in this section, the spatial dependency on the scattering vector Q is displayed as $Q\sigma$, where $\sigma = \sigma_A$ of the respective simulation.

Fig. 5.16 gives an overview of the intermediate scattering functions for the correlations AA, BB, and AB determined for the simulated reference system. Simultaneously, the temporal decay of the global maximum $S_{ij,\text{max}}(Q\sigma, t)$ is presented for the three correlations of the reference system as well.

Qualitatively, most information provided by the partial intermediate scattering functions of the reference system agree with what is found in case of the simulated $S_{ij}(Q, t)$ in section 5.2.1, Fig. 5.15. All three correlations presented in Fig. 5.16 exhibit intermediate scattering functions typical for liquid-like structures. The global maxima of the partial intermediate scattering functions relative to their baseline relate to one another as $S_{AA,\text{max}}(Q\sigma, t) - 1 = 0.88 > S_{AB,\text{max}}(Q\sigma, t) = 0.72 > S_{BB,\text{max}}(Q\sigma, t) - 1 = 0.53$. In contradiction to the simulations of the system in the previous section, the relaxation times do not relate to each other in the same sequence as the global maxima, but as $t_{\text{rel.},AB} = 100 \text{ ms} > t_{\text{rel.},AA} = 85 \text{ ms} > t_{\text{rel.},BB} = 75 \text{ ms}$. Interestingly, $t_{\text{rel.},AB} > t_{\text{rel.},AA}$ is found, although $S_{AA,\text{max}}(Q\sigma, t) - 1 > S_{AB,\text{max}}(Q\sigma, t)$. Thus, it is concluded, that in case of this reference system the loss of correlation over time depends not only on the strength of a specific correlation.

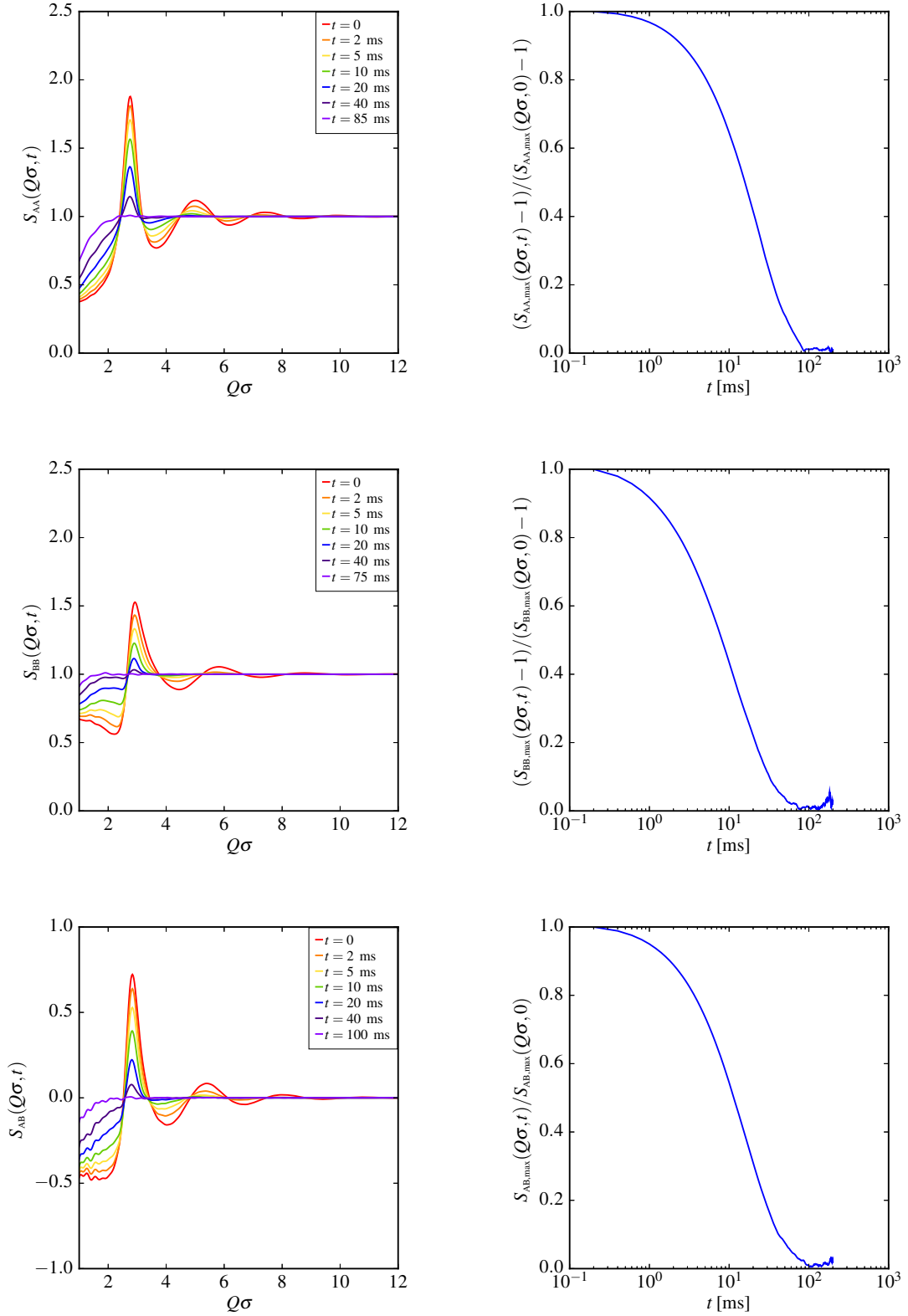


Fig. 5.16: Partial intermediate scattering functions $S_{ij}(Q\sigma, t)$ and normalised temporal relaxation functions characterising the reference system modelled by BD simulations. The reduced scattering vector $Q\sigma$ is displayed with $\sigma = \sigma_A = 212$ nm.

Structure of the simulated binary mixtures

The results of the intermediate scattering functions at $t = 0$ obtained for the 18 simulations with varied parameters are presented in Fig. 5.17, for correlations AA as an example. The corresponding intermediate scattering functions for BB and AB correlations are found in appendix B.

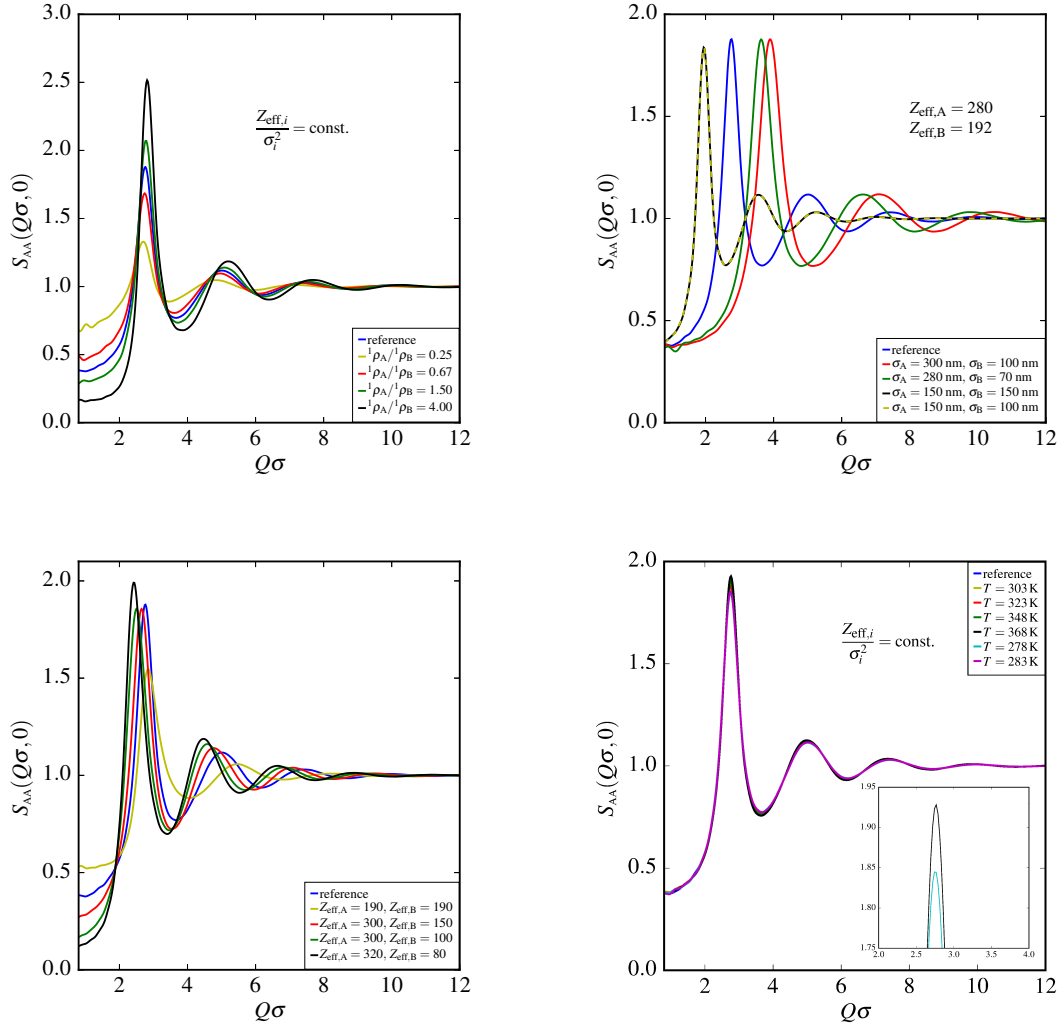


Fig. 5.17: Intermediate scattering functions $S_{AA}(Q, 0)$ at $t = 0$ of AA correlations obtained from BD simulations: under variation of the number density ratio ρ_A/ρ_B (upper left), with different effective surface charges $Z_{\text{eff},A}$ and $Z_{\text{eff},B}$ (lower left), varying the particle diameters σ_A and σ_B (upper right), and changing the temperature T of the system (lower right). The reduced scattering vector $Q\sigma$ is displayed with $\sigma = \sigma_A$.

In Fig. 5.17 there are four graphics. In the upper left, $S_{AA}(Q\sigma, 0)$ of the samples with variations in the number ratios of particle classes A and B are compared. The upper right graphic presents those static structure factors of samples with modified particle sizes. In the lower left, effects of changes in numbers of surface charges of the two components of the mixture on $S_{AA}(Q\sigma, 0)$ are displayed. The lower right graphic compiles intermediate scattering functions at $t = 0$ obtained for different temperatures of the simulated systems. In all four graphics $S_{AA}(Q\sigma, 0)$ of the reference system serves as a benchmark.

Number density dependence Obviously, an increase of the ratio ${}^1\rho_A/{}^1\rho_B$ leads to an enhancement of the AA correlation. While at ${}^1\rho_A/{}^1\rho_B = 0.25$ merely a weak liquid-like order with $S_{AA,\max}(Q\sigma, 0) = 1.33$ is observed for particles of class A, at ${}^1\rho_A/{}^1\rho_B = 4.00$ the particles of this class form a pronounced liquid-like structure with $S_{AA,\max}(Q\sigma, 0) = 2.52$. As becomes apparent when considering BB correlations for the same samples (cf. Fig. B.1 in appendix B), the observed effect scales with the strength of particle interaction, influenced by the number of charges. Thus, $S_{BB,\max}(Q\sigma, 0) = 1.86$ at ${}^1\rho_B/{}^1\rho_A = ({}^1\rho_A/{}^1\rho_B)^{-1} = 4.00$ exhibits a significantly weaker correlation of particles B than $S_{AA,\max}(Q\sigma, 0) = 2.52$ at ${}^1\rho_A/{}^1\rho_B = 4.00$, due to $Z_{\text{eff},A} = 280 > Z_{\text{eff},B} = 192$. For AB correlations (cf. Fig. B.2 in appendix B), at similar number ratios of classes A and B ($0.67 \leq {}^1\rho_A/{}^1\rho_B \leq 1.50$) no significant effect on the amplitude $S_{AB,\max}(Q\sigma, 0) \approx 1$ is observed with regard to the reference. However, with increasing difference between ${}^1\rho_A$ and ${}^1\rho_B$ the correlation becomes weaker, because the number of possible pair correlations between one particle of A and one particle of B is decreased. This effect grows slightly stronger the fewer particles of the class with larger charge number are present, indicated by $S_{AB,\max}(Q\sigma, 0) = 0.79$ at ${}^1\rho_A/{}^1\rho_B = 0.25$ and $S_{AB,\max}(Q\sigma, 0) = 0.84$ at ${}^1\rho_A/{}^1\rho_B = 4.00$.

For the four simulations with different number density ratios a slight shift of $S_{AA}(Q\sigma, 0)$ to larger $Q\sigma$ is observed with increasing ratio ${}^1\rho_A/{}^1\rho_B$. This originates from the enhancement of the number density of particles A with rising ${}^1\rho_A/{}^1\rho_B$, leading to sinking particle interdistances d , which trivially effects the observed shift to larger scattering vectors Q due to $Q \approx 2\pi/d$.

With increasing ratio ${}^1\rho_A/{}^1\rho_B$ the value of $S_{AA}(Q\sigma, 0)$ is reduced in the limit $Q \rightarrow 0$. As the number ratio of B is lowered, the system approaches the limit of a homo-colloidal dispersion with regard to the observed AA correlations, which leads to a sinking isothermal compressibility κ_T of the system. The proportionality of κ_T to the limiting value of the static intermediate scattering function for $Q \rightarrow 0$, according to the fluctuation-dissipation theorem [108], explains the decrease, which is noticed for $S_{AA}(Q\sigma, 0)$ at $Q \rightarrow 0$ for increasing ${}^1\rho_A/{}^1\rho_B$. In case of AB correlations a more complex interplay of surface charges and number ratios leads to a sequence of $S_{AB}(Q\sigma, 0)$ at $Q \rightarrow 0$ not quite straightforward, which is why this matter is not resolved in detail here. A thermodynamically sound connection between the microscopic circumstances, described for example by partial static structure factors of colloidal mixtures, and macroscopic properties, such as the isothermal compressibility, is given by Kirkwood and Buff's theory of solutions [118]. Originally derived for a system of solute and solvent in terms of statistical mechanics, this theory has proved valid not only for simple solutions but has been shown applicable to alloys [119], biological systems [120] and charged colloidal particles [121], as the ones simulated by BD in this section. Generally, for a system consisting of two components 1 and 2, the isothermal compressibility κ_T can be expressed in dependence on the Kirkwood-Buff factors G_{ij} [118]

$$\kappa_T = \frac{1}{k_B T} \cdot \frac{1 + \varrho_1 G_{11} + \varrho_2 G_{22} + \varrho_1 \varrho_2 (G_{11} G_{22} - G_{12})^2}{\varrho_1 + \varrho_2 + \varrho_1 \varrho_2 (G_{11} + G_{22} - 2G_{12})}, \quad (5.3)$$

where ϱ_1 and ϱ_2 denote the number densities of the two components and $k_B T$ is the thermal energy. The Kirkwood-Buff factors are defined in terms of the total pair correlation function $h(r) = g_{ij}^{(2)}(r) - \delta_{ij}$

$$G_{ij} = 4\pi \int_0^{\infty} h(r)r^2 dr, \quad (5.4)$$

which are also referred to as Kirkwood-Buff integrals. With the definition of the structure factor $S(Q)$ for spherical particles as the Fourier-Bessel transform of the pair distribution function (cf. eq. 2.9), the partial structure factors

$$S_{ij}(0) - \delta_{ij} = (\rho_i \rho_j)^{1/2} \cdot G_{ij}, \quad (5.5)$$

are connected to the Kirkwood-Buff factors in the limit $Q \rightarrow 0$. In this way, a formal description of the contributions of the static intermediate scattering functions $S_{ij}(Q, 0)$ to the isothermal compressibility κ_T of a binary mixture according to (5.3) is given at $Q \rightarrow 0$.

Dependence on number of effective charges Considering the static intermediate scattering functions of simulations with different numbers of surface charges, two tendencies can be identified for correlations AA and BB (cf. lower left graphics in Figs. 5.17 and B.1). First, $S_{ij,\max}(Q\sigma, 0)$ is enhanced with increasing Z_{eff} of the component relevant for the respective correlation, which originates from the strengthening of particle interactions due to the higher number of charges of the correlated particles. Secondly, with decreasing charge number of the respective other component, not directly involved in the observed correlation, e. g., $Z_{\text{eff,B}}$ for AA correlation, $S_{ij}(Q\sigma, 0)$ is shifted to smaller scattering vectors Q , corresponding to a larger mean distance between correlated particles of class A. This can, for example, be well observed for the green and red curves in the lower left graphic of Fig. 5.17, where $Z_{\text{eff,A}} = 300$ is equal in both corresponding simulations while $Z_{\text{eff,B}}$ varies from 150 to 100. A decreased number of surface charges of particles B leads to a diminished localisation of these particles, e. g., around a central particle of class A. As an illustration, the distinct pair distribution functions $g_{AB}^{(2)}(r/\sigma, 0)$ at $t = 0$ obtained from the two afore mentioned examples of BD simulations are displayed in Fig. 5.18. The reduced distance r/σ is displayed with $\sigma = \sigma_A$.

Apparently, a decreased particle localisation leads to the possibility of coordinating particles B being slightly closer to a central particle A at $Z_{\text{eff,B}} = 100$ compared to the structure determined for the system with $Z_{\text{eff,B}} = 150$. As this holds for all particles A, the distance d between two particles A is effectively increased due to electrostatic repulsion. With $Q \approx 2\pi/d$ the shift of static intermediate scattering functions $S_{AA}(Q, 0)$ to smaller scattering vectors Q at constant $Z_{\text{eff,A}}$ and decreasing $Z_{\text{eff,B}}$ is explained.

Considering the results for $S_{BB}(Q\sigma, 0)$ in the lower left graphic of Fig. B.1 in appendix B, similar effects can be observed for BB correlations vice versa with decreasing surface charge number of particles A. Further it is to be stated that for $Z_{\text{eff,B}} \leq 100$ almost no detectable liquid-like order is observed for BB correlations, indicated by amplitudes of $S_{BB,\max}(Q\sigma, 0) \leq 1.1$.

In case of AB correlations determined for simulations with varying charge numbers the static intermediate scattering functions $S_{AB}(Q\sigma, 0)$ are expectedly influenced by an interplay of the effects observed for AA and BB correlations. Apparently, as long as $Z_{\text{eff,B}} \geq 150$, $S_{AB,\max}(Q\sigma, 0)$ roughly diminishes with decreasing overall charge number

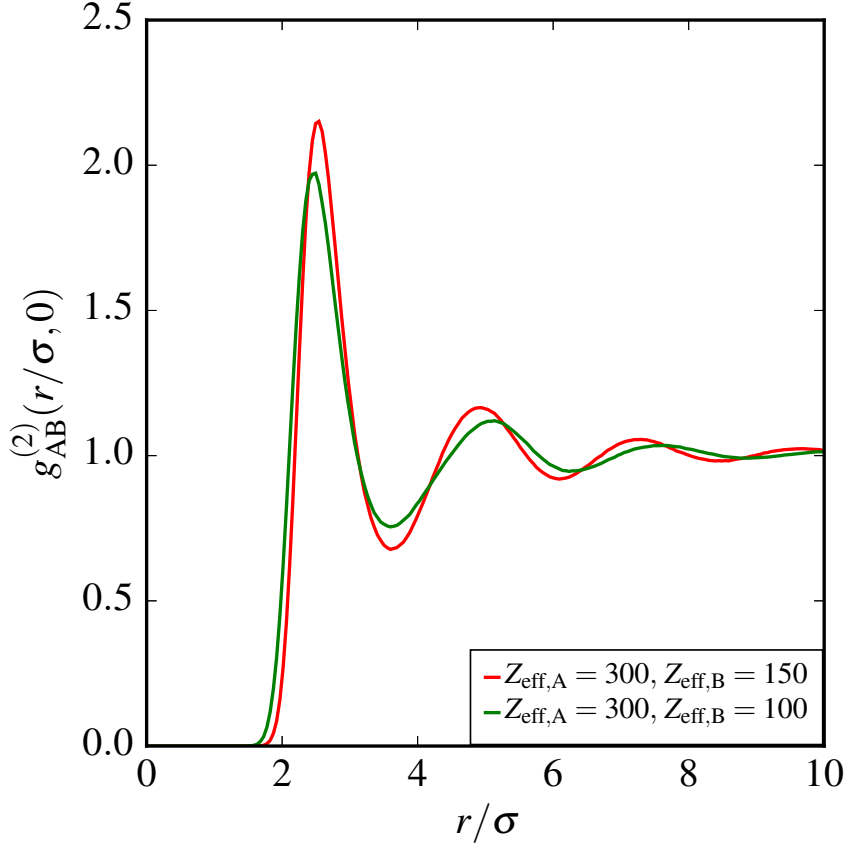


Fig. 5.18: Distinct pair distribution functions $g_{AB}^{(2)}(r/\sigma, t)$ at $t = 0$ obtained by BD simulations with varied numbers of surface charges $Z_{\text{eff,A}} = 300, Z_{\text{eff,B}} = 150$ and $Z_{\text{eff,A}} = 300, Z_{\text{eff,B}} = 100$. The reduced distance r/σ is displayed with $\sigma = \sigma_A$. It can be seen, that for a lower charge number $Z_{\text{eff,B}}$ particles B may be located slightly closer to a central particle A than for a larger charge number $Z_{\text{eff,B}}$.

$Z_{\text{total}} = Z_{\text{eff,A}} + Z_{\text{eff,B}}$. For $Z_{\text{eff,B}} \leq 100$, however, $S_{AB,\text{max}}(Q\sigma, 0)$ is significantly reduced, although Z_{total} remains comparable to those simulations with stronger ordering. It seems that the lack of surface charges of particles B, leading to almost no order in BB correlations, also effects a decline of correlations between particles of A and B, although $Z_{\text{eff,A}} \geq 300$.

Results for all three correlation types AA, BB, and AB obtained from simulations with varying numbers of surface charges indicate an increase of $S_{ij}(Q\sigma, 0)$ at $Q \rightarrow 0$ with decreasing amplitude $S_{ij,\text{max}}(Q\sigma, 0)$. This observation can be well understood considering that for the structure of an ideal gas $S(Q) \equiv 1$, or in case of a mixed correlation $S(Q) \equiv 0$. As such, keeping in mind that a weighted sum of all $S_{ij}(Q\sigma \rightarrow 0, 0)$ is proportional to κ_T , the observed effects point to an increase of the isothermal compressibility, while the structure of the correlated particles approaches the limit of an ideal gas, where κ_T at a given temperature T solely depends on the number density with $\kappa_T = p^{-1} = (\rho k_B T)^{-1}$.

Particle size dependence The upper right graphic in Fig. 5.17 compiles the results obtained for $S_{AA}(Q\sigma, 0)$ by BD simulations of mixtures with varying particle sizes σ_A and

σ_B . The corresponding intermediate scattering functions for BB and AB correlations are found in appendix B. From the results for all three correlation types it is apparent, that the shape of the obtained intermediate scattering functions in principal is not influenced by a variation of any of the two particle sizes. However, a marginal decrease of the amplitude $S_{ij,\max}(Q\sigma, 0)$ is found for AA and AB correlations with a smaller diameter of $\sigma_A = 150$ nm. The observable shift of $S_{ij}(Q\sigma, 0)$ along $Q\sigma$ merely originates from the displayed dependence on $\sigma = \sigma_A$.

Temperature dependence The fourth graphic on the lower right in Fig. 5.17 exemplarily presents the effect of different temperatures in the range $278 \text{ K} \leq T \leq 368 \text{ K}$ on the static intermediate scattering function $S_{AA}(Q\sigma, 0)$. In agreement with tendencies found for BB and AB correlations in appendix B as well, a successive, slight enhancement of the liquid-like order is observed for increasing temperatures. On the one hand a progressive decrease of the relative permittivity ε_r of the dispersion medium leads to a more repulsive, electrostatic potential V_{ij} between charged particles and hence to a more pronounced order. On the other hand, an increasing temperature leads to a rising thermal energy $k_B T$, effecting a decrease of the liquid-like order. As can be seen by the inset magnifications in the lower right graphics in Figs. 5.17, B.1, and B.2, including the amplitudes of static structure factors at 278 K and 368 K, the result of the interplay of the described effects is a comparably weak enhancement of the formed liquid-like order despite a temperature difference of 90 K. E. g., in case of the AA correlation the amplitude is merely increased from $S_{AA,\max}(Q\sigma, 0) \approx 1.85$ at 278 K to $S_{AA,\max}(Q\sigma, 0) \approx 1.93$ at 368 K. Obviously, in the interplay $V_{ij}/k_B T$ the rising electrostatic repulsion slightly overcompensates the simultaneous increase of the thermal energy. In summary it can be stated, that temperature does not exhibit a significant influence on structure formation in binary mixtures of colloidal particles in a region of thermal stability.

Collective dynamics of the simulated binary mixtures

The temporal dependency of the maxima of intermediate scattering functions resulting from the performed BD simulations with differing parameters is exemplarily summarised for AA correlations in Fig. 5.19. The relaxation functions for BB and AB correlation results are found in appendix C.

Number density dependence First, the upper left graphic in Fig. 5.19 is considered, wherein time decays of $S_{AA,\max}(Q\sigma, t)$ obtained for mixtures with varying number density ratio ${}^1\rho_A/{}^1\rho_B$ are presented. As can be clearly seen, for AA correlations the sequence of increased relaxation times follows an enhancing ratio ${}^1\rho_A/{}^1\rho_B$. Due to a larger overall charge number within the system by the presence of more particles of class A, as $Z_{\text{eff},A} > Z_{\text{eff},B}$, the electrostatic particle interaction is increased, which causes a preservation of the dynamic correlation of particles over longer times. In this way, the time of complete relaxation, defined as the time when the normalised correlation function is relaxed to 0.01, increases from $t_{\text{rel.,AA}} \approx 80$ ms for ${}^1\rho_A/{}^1\rho_B = 0.25$ to $t_{\text{rel.,AA}} \approx 150$ ms for ${}^1\rho_A/{}^1\rho_B = 4.00$. Similar trends are observed for AB and BB correlations as well, whereby for a given ratio ${}^1\rho_A/{}^1\rho_B$ the relaxation times found for the three correlations in general relate to each other as $t_{\text{rel.,AA}} > t_{\text{rel.,AB}} > t_{\text{rel.,BB}}$. This sequence is ascribed to the interaction between correlated particles, which scales with the number of surface charges, where $Z_{\text{eff},A} > Z_{\text{eff},B}$.

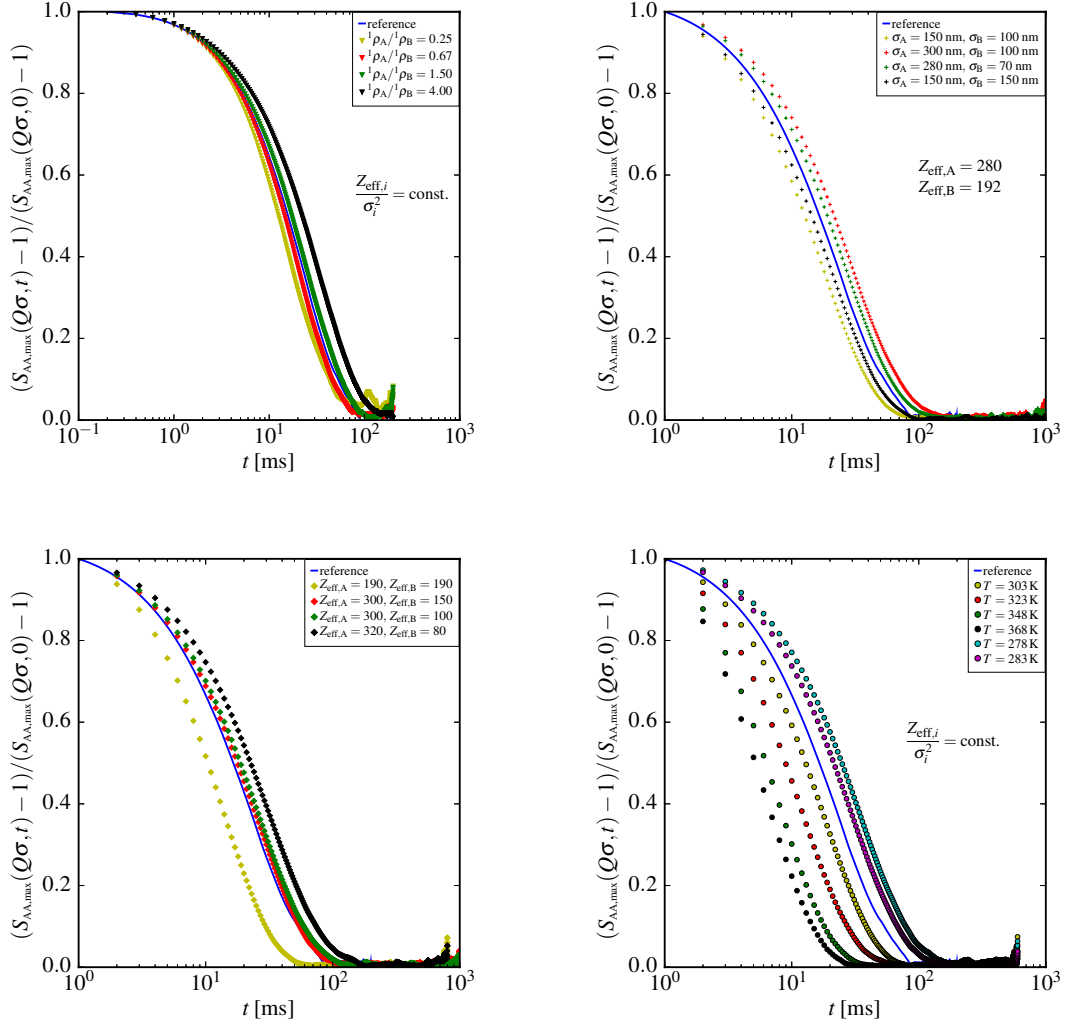


Fig. 5.19: Normalised relaxation of the global maxima of partial intermediate scattering functions $S_{AA,\max}(Q\sigma, t)$ obtained by BD simulations under variation of: the number density ratio ${}^1\rho_A/{}^1\rho_B$ (upper left), effective surface charges $Z_{\text{eff},A}$ and $Z_{\text{eff},B}$ (lower left), particle diameters σ_A and σ_B (upper right), and the system temperature T (lower right). The reduced scattering vector $Q\sigma$ is displayed with $\sigma = \sigma_A$.

Dependence on number of effective charges The lower left graphic in Fig. 5.19 displays the temporal relaxation behaviour of $S_{AA,\max}(Q\sigma, t)$ determined by simulations with varying numbers of effective surface charges. Generally, the relaxation time increases with enhancing charge number $Z_{\text{eff},A}$ caused by a stronger order as indicated by the corresponding static scattering functions $S_{AA}(Q\sigma, 0)$ (cf. lower left in Fig. 5.17). In case of equal $Z_{\text{eff},A}$ for those simulations indicated by red and green markers, the relaxation functions indeed nearly coincide. Marginal deviations that can be identified between these relaxation functions are ascribed to the difference of 50 charges in $Z_{\text{eff},B}$ indirectly influencing pair correlations of particles A. As discussed for static intermediate scattering functions of the corresponding simulations, a smaller $Z_{\text{eff},B}$ effects a larger distance between particles A. Due to this a larger relaxation time of the AA correlation is observed. A combination of both effects results in an increase of the relaxation time of AA correlations observed for simulations with varying surface charges from $t_{\text{rel.,AA}} \approx 50$ ms for $Z_{\text{eff},A} = Z_{\text{eff},B} = 190$

to $t_{\text{rel.,AA}} \approx 150$ ms for $Z_{\text{eff,A}} = 320$ and $Z_{\text{eff,B}} = 80$.

In case of BB correlations (cf. lower left in Fig. C.1) two domains are to be distinguished. For $Z_{\text{eff,B}} \leq 100$, almost no liquid-like structure is observable, which leads to very short relaxation times $t_{\text{rel.,BB}} \approx 5$ ms. Irregular progression of the BB time correlation functions for $Z_{\text{eff,B}} = 100$ and $Z_{\text{eff,B}} = 80$ is subject to noisy data for $S_{\text{BB}}(Q\sigma, t)$ in regions of larger times due to weak ordering. For those simulations with $Z_{\text{eff,B}} \geq 150$ a rough tendency of increasing relaxation time is noticed with a growing charge number $Z_{\text{eff,A}}$, which interestingly contradicts what is found vice versa for AA correlations. Hence the interplay of comparably small charge numbers of class B, causing only moderate liquid-like order in BB correlations, and comparably large charge numbers of A must lead to the observed dynamic behaviour, which cannot be resolved in detail at this stage.

As can be deduced from AB time correlation functions (cf. lower left in Fig. C.2), the time dependency of $S_{\text{AB,max}}(Q\sigma, t)$ is dominated by particles of class A. For the simulation with a small charge number of $Z_{\text{eff,A}} = 190$ a comparably short relaxation time of $t_{\text{rel.,AB}} \approx 50$ ms is found. For simulations with larger charge numbers $Z_{\text{eff,A}}$ between 280 and 320, higher relaxation times of $t_{\text{rel.,AB}} \approx 100$ ms are identified, which is ascribed to stronger particle correlation due to the larger charge number of particles A. This effect seems to be independent from the charge number of particles B, that varies from 192 to 80 for the observed simulations. Generally, as long as $\sigma_A > \sigma_B$ and $Z_{\text{eff,A}} > Z_{\text{eff,B}}$, the relaxation times of the corresponding correlations relate to each other as $t_{\text{rel.,AA}} > t_{\text{rel.,AB}} > t_{\text{rel.,BB}}$, as observed in case of simulations with varying number ratios.

Particle size dependence As described above, from Fig. 5.17 it is obvious, that the liquid-like order formed by correlating particles of class A is not influenced by the particle sizes σ_A and σ_B . However, the presentation of the time decay of $S_{\text{AA,max}}(Q\sigma, t)$ in the upper right graphic in Fig. 5.19 shows, that varying particle diameters do affect the time correlation of two particles A in the simulated mixtures. Apparently, the relaxation time increases with a growing sum of diameters $\sum \sigma_i = \sigma_A + \sigma_B$. Fig. 5.20 displays the same relaxation functions for AA correlations renormalised in time to the corresponding diameters σ_A , whereby slight deviations between the presented relaxation functions remain. However, renormalising the same functions to the corresponding sum of particle diameters $\sum \sigma_i$ leads to all presented relaxation functions coinciding. Hence, the differences observed for temporal relaxation of partial intermediate scattering functions in dependence on varying particle sizes appear to be not solely caused by the trivial influences of the corresponding diameters σ_i on the Stokes-Einstein self-diffusion coefficients $D_{0,i} \propto \sigma_i^{-1}$, which affect particle displacement in the employed Ermak algorithm (cf. eq. (2.5)). Interestingly, fluctuations of the sub-systems formed by the two components of the simulated binary mixture seem to have an influence on the temporal relaxation of the partial intermediate scattering functions, which can well be also assumed for relaxations of BB and AB correlations displayed in upper right graphics of Figs. C.1 and C.2.

Temperature dependence The lower right in Fig. 5.19 presents the temperature dependency of the temporal decay of $S_{\text{AA,max}}(Q\sigma, t)$. Clearly, the observed relaxation times increase with decreasing temperature. Hence, the marginally enhanced structure, as identified for static intermediate scattering functions in the lower right graphic of Fig. 5.17, is overcompensated by the simultaneously decreasing dynamic viscosity η of the dispersion medium. The latter strongly increases the Stokes-Einstein diffusion coefficient which contributes to particle displacement in the employed Ermak algorithm (cf. eq. (2.5))

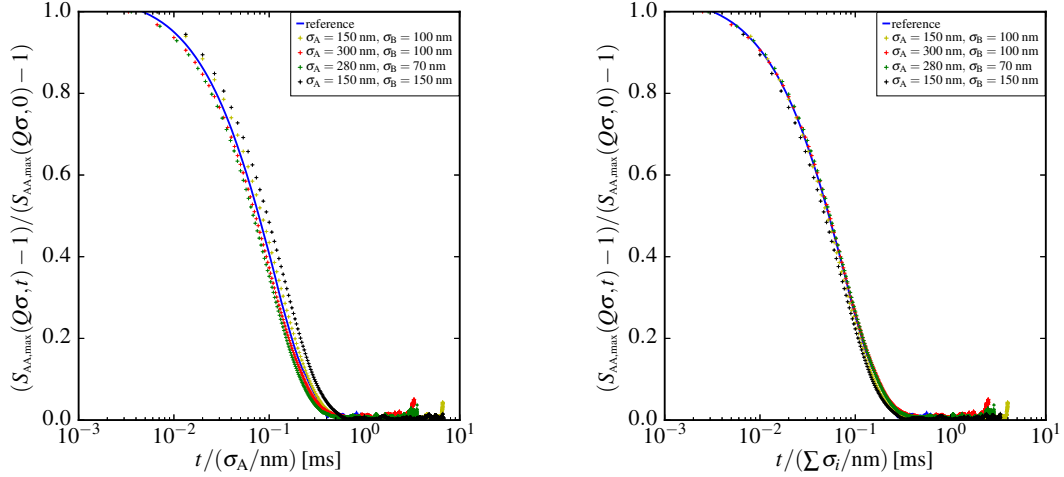


Fig. 5.20: Normalised temporal relaxation functions of $S_{AA,\max}(Q\sigma, t)$ determined for BD simulations with differing particle diameters σ_A and σ_B . Renormalisation of the delay time t to the respective diameter σ_A (left) leads to slight deviations remaining between the presented relaxation functions, while renormalisation of the delay time t to the corresponding sum of particle diameters $\sum \sigma_i = \sigma_A + \sigma_B$ (right) leads to identity of all presented relaxation functions.

and thus leads to a decrease of the relaxation time $t_{\text{rel.,AA}} \approx 170$ ms of AA correlations at $T = 278$ K to $t_{\text{rel.,AA}} \approx 20$ ms at $T = 368$ K. Similar tendencies are also observed for AB and BB correlations. Again, the sequence of relaxation times compared between the different types of correlations at a given temperature follows $t_{\text{rel.,AA}} > t_{\text{rel.,AB}} > t_{\text{rel.,BB}}$, while $\sigma_A > \sigma_B$ and $Z_{\text{eff,A}} > Z_{\text{eff,B}}$.

Examples for collective diffusion coefficients

In case of self-diffusion it is known, that short-time diffusion coefficients D_S^S can be obtained, that may differ significantly from long-time diffusion coefficients D_S^L (cf. section 2.3.2). For selected examples of the time correlations discussed before, it shall be illustrated, that such distinct diffusive regions in the limits of short and long times are also identified for collective diffusion in the simulated binary mixtures and may be quantified in terms of collective diffusion coefficients D^L and D^S . In Fig. 5.21 the temporal decays of the maxima of the partial intermediate scattering functions for the simulated reference system are displayed. The time dependency of the intermediate scattering function is identical to the field autocorrelation function $g_1(\tau)$, obtainable from light scattering experiments. As such, the slopes of the functions presented in Fig. 5.21 in the short-time and in the long-time limit are determined by a single exponential fit to these functions at short times as well as at long times. This can also be seen in the example graphics in Fig. 5.21.

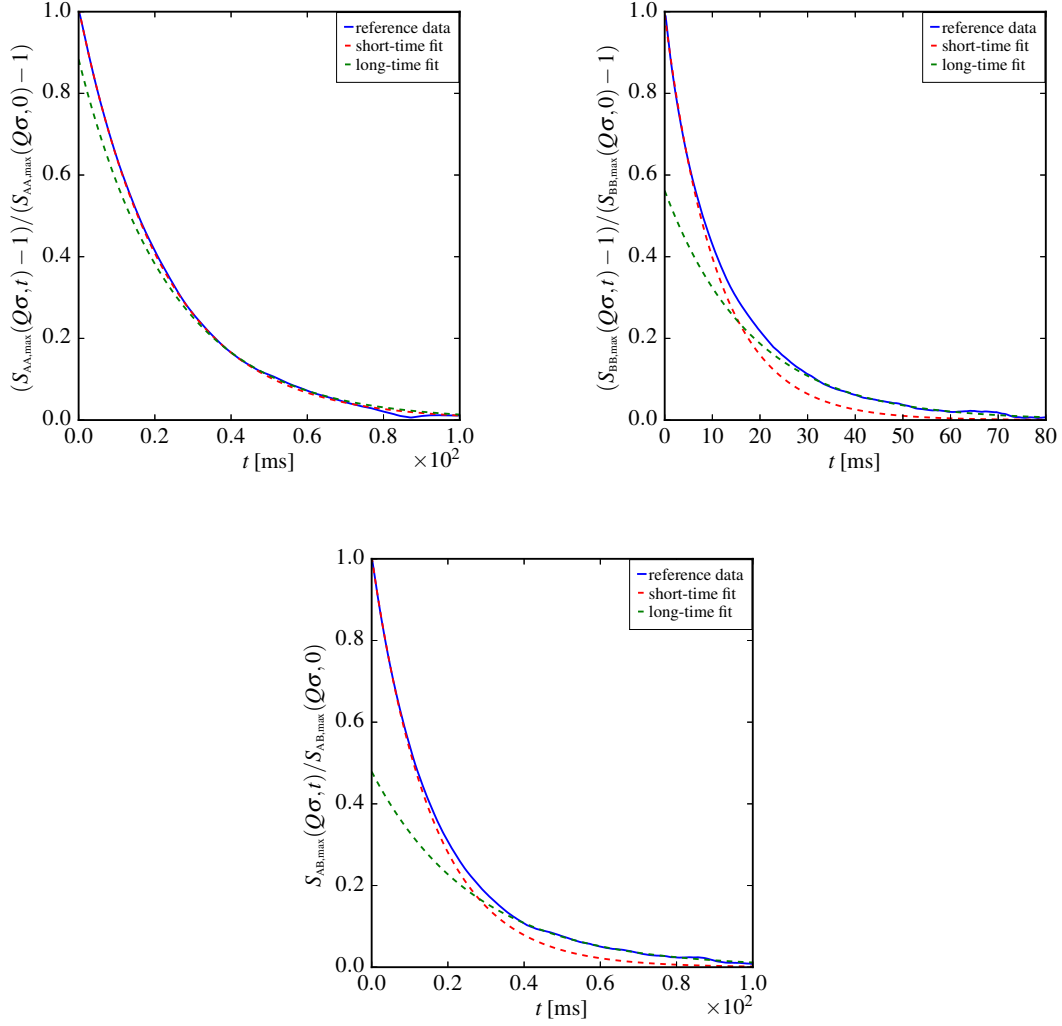


Fig. 5.21: Time relaxation functions for the maxima of the partial intermediate scattering functions $S_{ij,\max}(Q\sigma, t)$ with $\sigma = \sigma_A = 212$ nm obtained for the simulated reference system. Respectively fitting a single exponential function to short-time and long-time data, identifies two different diffusive regions, for which corresponding collective short-time and long-time diffusion coefficients can be determined. In between the two limits, a sub-diffusive region is recognised, in which collective diffusion is time-dependent.

As expected, different slopes are identified in the short-time and the long-time limits. Especially in cases of the BB and AB correlation sub-diffusive areas in between the two limiting time domains are recognisable, where the collective diffusion is time-dependent, while the short-time and long-time diffusion behaviour observable for the AA correlation are only slightly different. Employing the Landau-Placzek relation, knowing the scattering vector of each $S_{ij,\max}(Q\sigma, t)$, the corresponding collective long-time and short-time diffusion coefficients D^L and D^S for AA, BB, and AB correlations are determined. Table 5.10 compiles the such obtained results for the simulated reference binary mixture and two examples chosen from the 18 binary mixtures simulated with varying parameters. As a reminder of the meaning of the simulation IDs the reader is referred to tables 5.7-5.9.

Table 5.10: Compilation of collective short-time (D^S) and long-time (D^L) diffusion coefficients for the simulated binary reference system and two chosen examples of simulations with varied parameters. For all three presented simulations diffusion coefficients are determined at the global maxima of the corresponding intermediate scattering functions with the scattering vectors: $Q_{AA} = 1.30 \times 10^{-2} \text{ nm}^{-1}$, $Q_{AB} = 1.34 \times 10^{-2} \text{ nm}^{-1}$, and $Q_{BB} = 1.38 \times 10^{-2} \text{ nm}^{-1}$. The short-time self-diffusion coefficients of particles A ($D_{S,A}^S$) and B ($D_{S,B}^S$) are calculated for comparison according to the Stokes-Einstein relation.

ID	Correlation	$D^L/10^{-12}$ [m ² s ⁻¹]	$D^S/10^{-12}$ [m ² s ⁻¹]	D^L/D^S	$D_{S,A}^S/10^{-12}$ [m ² s ⁻¹]	$D_{S,B}^S/10^{-12}$ [m ² s ⁻¹]
reference	AA	0.25	0.26	0.96	2.02	4.28
	AB	0.21	0.35	0.60		
	BB	0.29	0.48	0.60		
Temp6	AA	0.18	0.19	0.95	1.49	3.16
	AB	0.20	0.26	0.77		
	BB	0.27	0.36	0.75		
Size2	AA	0.17	0.20	0.85	1.43	4.28
	AB	0.23	0.28	0.82		
	BB	0.25	0.44	0.57		

As can be expected, the relation $D^L \leq D^S$ holds for all collective diffusion coefficients of a given correlation contained in table 5.10. With respect to the reference, the diffusion coefficients for simulation Temp6 are generally decreased, due to the temperature $T = 283 \text{ K}$ which is 10 K lower than for the reference system. For simulation Size2, D^L is decreased even more relative to the reference, caused by the larger diameter of particles A slowing down diffusion. In agreement with the findings for the relaxation times of the maxima of the partial intermediate scattering functions discussed above (cf. Fig. 5.19), the diffusion coefficients found for the three correlations of one simulated mixture appear to relate to one another as $D(\text{AA}) < D(\text{AB}) < D(\text{BB})$, while $\sigma_A > \sigma_B$ and $Z_{\text{eff},A} > Z_{\text{eff},B}$. An exception to this rule is found for the long-time diffusion coefficients of the reference simulation, where $D^L(\text{AB}) < D^L(\text{AA}) < D^L(\text{BB})$. This might be an indication either for further influences on the diffusion behaviour, that cannot be resolved at this point, or for erroneous data at the long-time limit of the AB correlation function, which might be caused by effects of statistical uncertainty. Expectedly, with regard to the self-diffusion coefficients of particles A and B calculated according to the Stokes-Einstein equation (cf. eq. (2.17)), a significant decreasing of collective diffusion is noticed, due to enhanced particle interactions at distances corresponding to the here investigated coordination maxima of the intermediate scattering functions.

The systematic studies of the structure and dynamics of binary colloidal mixtures with Brownian Dynamics simulations exhibit valuable results regarding influences of a variety of different parameters on the partial intermediate scattering functions $S_{ij}(Q, t)$ characterising the simulated systems. It is also indicated, that by BD simulations collective diffusion coefficients of such binary colloidal mixtures can be quantified in the short-time and the long-time limit. As such, the results compiled in this work may form the basis for further in-depth simulations and for deliberate experimental investigations of liquid-like ordered binary colloidal mixtures. Well-suited model systems for such experiments are provided by the colloidal (co)polymer dispersions prepared in this work.

6 Investigations of ternary mixtures

The comprehensive possibilities provided by the newly developed colloidal copolymer dispersions, combining a defined particle size with any desired refractive index in the range $1.38 \leq n_p \leq 1.45$, give access to investigations of even more complex systems than binary mixtures. In this chapter, the self-diffusion of strongly scattering tracers in a binary matrix of charged colloids with nearly identical refractive index but different particle sizes and numbers of surface charges shall be investigated. Systematic BD simulations are performed to obtain extensive information about influences of several parameters of such a complex ternary system on the self-diffusion behaviour of the tracer particles.

First, a reference system is defined. The simulation parameters of this reference, in terms of particle diameters σ , particle number densities ${}^1\rho$ and numbers of surface charges Z_{eff} , are already given in table 3.1 of section 3.5.3. The dispersion medium water is modelled with a dynamic viscosity of $\eta = 1.002 \times 10^{-3} \text{ Pa} \cdot \text{s}$ and a relative permittivity of $\varepsilon_r = 78.3$ at a reference temperature of $T = 293.15 \text{ K}$. The parameters of the tracer component remain constant throughout all simulations carried out within this chapter. The parameters corresponding to the components of the binary colloidal matrix are denoted by subscripts A and B.

In eight different simulation sets the parameters characterising the matrix components are systematically varied. Table 6.1 compiles these properties for the first simulation set, simply referred to by integer identifiers (ID) from 1 to 6. The particle diameter of matrix component A is successively decreased from 100 nm in the reference system down to 50 nm, while simultaneously the size of matrix particles B is increased from 100 nm to 150 nm. As given in table 6.1, the numbers of effective particle surface charges for both components are adjusted to preserve a constant surface charge density.

By variation of σ and Z_{eff} at constant number ratios of the matrix components, however, the overall charge number of the matrix increases with rising size of particles B, which alters the interaction potential of the ternary system. To realise a constant total charge number, additional to the variations given by table 6.1, the number ratio of the less charged component, ${}^1\rho_A$, is successively increased, while ${}^1\rho_B$ of the other matrix component is reduced. This is presented in table 6.2 for the second simulation set denoted as ratio{1...6}.

The reference system is modelled with a moderate total colloidal particle density of ${}^1\rho_{\text{total}} = 5.0 \mu\text{m}^{-3}$ and an ionic strength solely originating from the autoprotolysis equilibrium of the dispersion medium water. Influences of variations in ${}^1\rho_{\text{total}}$, of the realisation of a given concentration of stray ions c_{stray} or a combination of both is investigated by six further sets of simulations, the remaining parameters of which are equal to those defined in tables 6.1 and 6.2. Table 6.3 gives an overview of the changes of total colloidal number density and stray ion concentration in these simulations.

Table 6.1: Adjusted particle sizes σ_i and effective surface charges $Z_{\text{eff},i}$ for matrix components A and B in the first simulation set of ternary mixtures. A constant surface charge density of the particles is maintained.

ID	σ_A [nm]	$Z_{\text{eff},A}$	σ_B [nm]	$Z_{\text{eff},B}$
1	90	162	110	242
2	80	128	120	288
3	70	98	130	338
4	60	72	140	392
5	50	50	150	450
6	75	113	125	313

Table 6.2: Number densities ${}^1\varrho_i$ of matrix components A and B defined for the second simulation set ensuring a constant total charge number. Matrix particle sizes and charge numbers are identical to the first simulation set.

ID	${}^1\varrho_A/{}^1\varrho_{\text{total}}$	${}^1\varrho_B/{}^1\varrho_{\text{total}}$
ratio1	0.498750	0.451250
ratio2	0.522500	0.427500
ratio3	0.546250	0.403750
ratio4	0.570000	0.380000
ratio5	0.593750	0.356250
ratio6	0.534375	0.415625

Table 6.3: Further simulation sets with modifications of the total colloidal number density ${}^1\varrho_{\text{total}}$ and addition of a given concentration of stray ions c_{stray} . Remaining simulation parameters are identical to those of the second simulation set defined in table 6.2.

ID	Parameter changes with regard to ratio{1...6}
dens{1...6}	${}^1\varrho_{\text{total}} = 15 \mu\text{m}^{-3}$
is1-{1...6}	$c_{\text{stray}} = 2 \times 10^{-3} \text{ M}$
is2-{1...6}	$c_{\text{stray}} = 2 \times 10^{-5} \text{ M}$
is3-{1...6}	$c_{\text{stray}} = 2 \times 10^{-4} \text{ M}$
dens+is-{1...6}	${}^1\varrho_{\text{total}} = 10 \mu\text{m}^{-3}, c_{\text{stray}} = 5 \times 10^{-5} \text{ M}$
dens+is2-{1...6}	${}^1\varrho_{\text{total}} = 10 \mu\text{m}^{-3}, c_{\text{stray}} = 5 \times 10^{-4} \text{ M}$

All 49 BD simulations defined above are initiated from a bcc start configuration. After 2.5×10^5 simulation steps the equilibrium structure is reached for each of the systems. Subsequently, a dynamic simulation run of 10^5 steps, i. e., a simulated time of 200 ms, is performed for every system. Analogously to the BD simulations of tracer particles in a homo-colloidal matrix in section 5.1.2, a Verlet-algorithm according to eq. (3.12) is employed to calculate the time-dependent self-diffusion coefficient $D_S(t)$ for the tracer particles from the corresponding mean squared displacements obtained for each simulation. In Figs. 6.1 and 6.2 the normalised time-dependent self-diffusion coefficients of the tracer particles $D_S(t)/D_S(0)$ are presented. In total, the two figures contain six graphics, each of which compiles the eight $D_S(t)/D_S(0)$ determined for one given size ratio of the matrix particles as well as the result of the reference simulation. The integer ratio following the simulation ID found in the key of each graphic indicates the size ratio of the matrix components in the form " $\sigma_A/\text{nm} : \sigma_B/\text{nm}$ ". The upper time limit of the displayed graphics is set to $t_{\text{max}} = 20$ ms, as for most of the time-dependent self-diffusion coefficients data at higher times become increasingly dominated by noise.

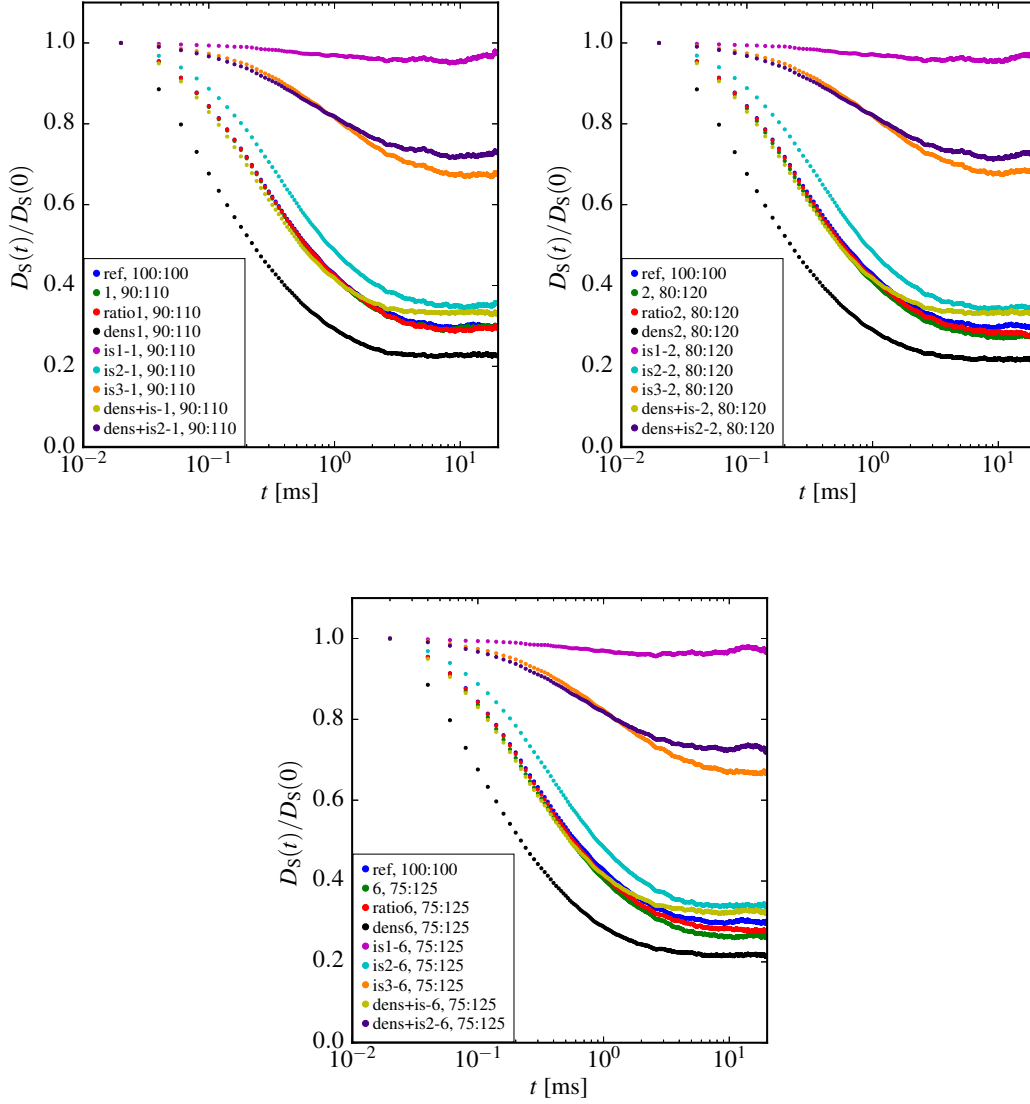


Fig. 6.1: Time dependency of the normalised tracer self-diffusion coefficients $D_S(t)/D_S(0)$ determined for the eight simulation sets of ternary mixtures investigated. Displayed are results for the first three ratios of matrix particle diameters σ_A and σ_B . Integers in the keys designate these ratios as: " $\sigma_A/nm : \sigma_B/nm$ ". The tracer self-diffusion coefficient obtained for the reference simulations is provided for comparison.

Influences of number density and ionic strength

From Figs. 6.1 and 6.2 several qualitative tendencies regarding effects of the simulation parameters on the tracer self-diffusion can be recognised. With regard to the reference, an increase of the total colloidal number density ${}^1q_{\text{total}}$ effects a significant decrease of $D_S(t)$, as is apparent from results for the simulation set dens $\{1 \dots 6\}$ (black circles). This originates from an effective enhancement of the repulsive potential between the matrix and tracer particles, caused by a reduction of the particle interdistance. The realisation of a given stray ion concentration c_{stray} increases the ionic strength I of the dispersion medium, which leads to a reduction of the Debye screening length λ_D and therefore to

a stronger screening of the repulsive Coulomb potential between two colloidal macroions (cf. eqs. (2.2), (2.3)). Hence, a successive increase of c_{stray} leads to a larger self-diffusion coefficient of tracer particles $D_S(t)$ with respect to the reference, as can be seen in Figs. 6.1 and 6.2 for the three simulation sets with varied stray ion concentration (magenta, cyan, and orange circles). In a combination of both, an increased colloidal number density and an enhanced ionic strength of the dispersion medium, the afore mentioned effects partially compensate each other, as can be observed for results of the two corresponding simulation sets in Figs. 6.1 and 6.2 (yellow and purple circles).

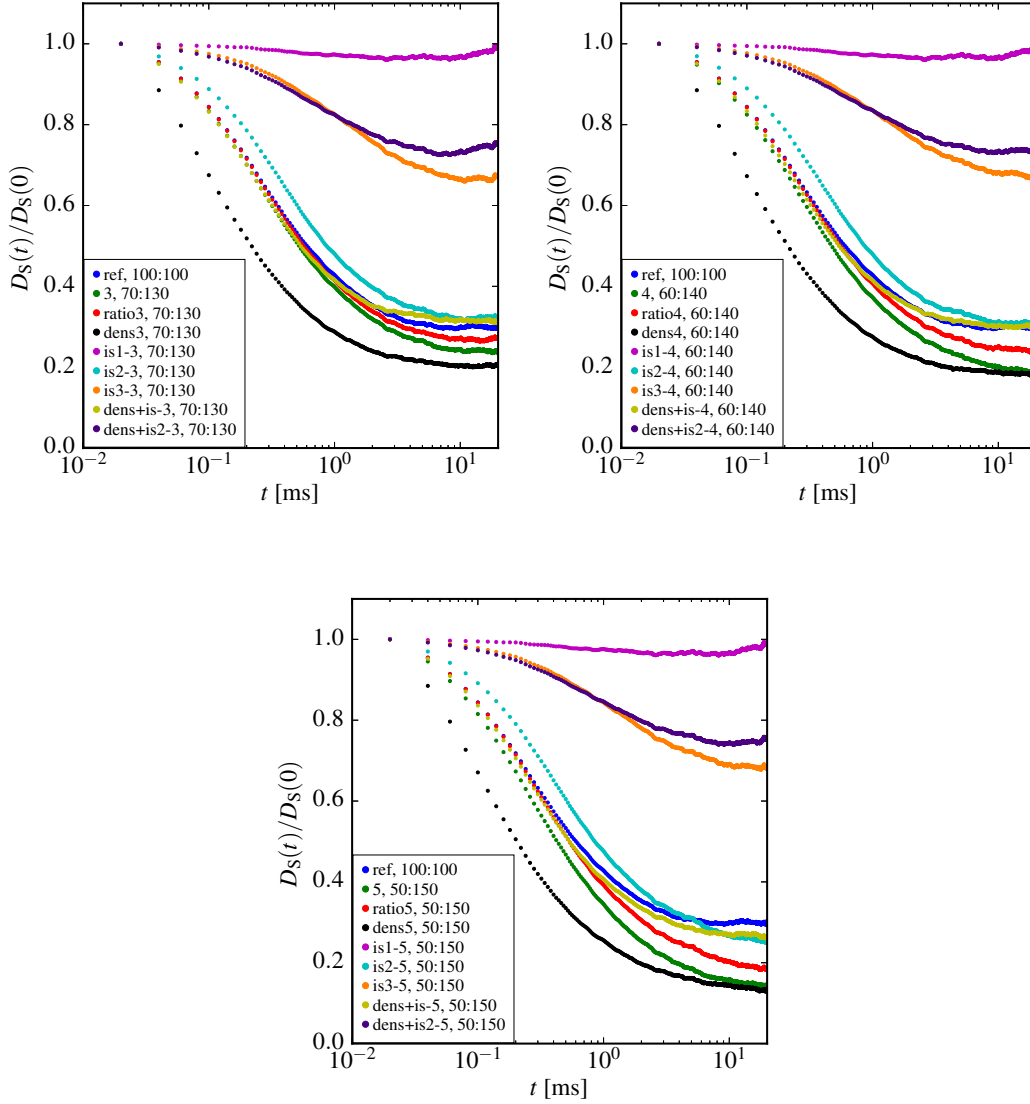


Fig. 6.2: Time dependency of the normalised tracer self-diffusion coefficients $D_S(t)/D_S(0)$ determined for the eight simulation sets of ternary mixtures investigated. Displayed are results for the remaining three ratios of matrix particle diameters σ_A and σ_B . Integers in the keys designate these ratios as: " $\sigma_A/\text{nm} : \sigma_B/\text{nm}$ ". The tracer self-diffusion coefficient obtained for the reference simulations is provided for comparison.

Within a more quantitative view on the long-time self-diffusion behaviour of tracer particles influenced by the variation of simulation parameters, two main cases are to be

distinguished. First, the diffusive motion of tracer particles over longer times may be slowed-down by an increased size and charge asymmetry of the two classes of matrix particles. In the second case, the long-time diffusion of tracers appears to be rather independent from the matrix particle asymmetry under the observed conditions. The origins of these two different phenomena are discussed in more detail in the following.

Decreased long-time tracer self-diffusion

In Fig. 6.3 the normalised self-diffusion coefficient $D_S(t = x)/D_S(0)$ of the simulated tracer particles in dependence on the diameter ratio of matrix particles σ_B/σ_A is presented for five of eight simulation sets. Here, x is a time in the range $10 \text{ ms} \leq x \leq 20 \text{ ms}$, at which a long-time limit of the tracer self-diffusion is reached. The normalised self-diffusion coefficient of tracers obtained for the reference simulation at the given time x serves as a benchmark. It is obvious from Fig. 6.3, that for simulations presented there $D_S(t = x)/D_S(0)$ is significantly decreased with increasing asymmetry of matrix particles.

In case of the here investigated ternary mixtures, long-time tracer self-diffusion is decreased if at least one of the two matrix components exhibits a pronounced liquid-like order. The number of surface charges has an essential influence on self-organisation of charged colloidal particles, as is well known and has been explicitly proven in section 5.2.2, where binary colloidal mixtures have been investigated which are very similar to the binary matrix comprised in the here observed ternary mixture.

Fig. 6.4 compares the partial pair distribution functions $g_{AA}^{(2)}(r/\sigma)$ and $g_{BB}^{(2)}(r/\sigma)$ of matrix particles A and B obtained for selected simulations, exemplarily for systems for which a decreased long-time tracer self-diffusion is encountered, to the corresponding pair distribution functions resulting from the reference simulation. $\sigma = 212 \text{ nm}$ here denotes the diameter of the tracer particles.

From Fig. 6.4 it is obvious, that the ordering of particles A is progressively reduced from a pronounced liquid-like order for ratio1 ($\sigma_A = 90 \text{ nm}$, $Z_{\text{eff},A} = 162$) to a moderate liquid-like order for ratio5 ($\sigma_A = 50 \text{ nm}$, $Z_{\text{eff},A} = 50$). Particles B also exhibit a pronounced liquid-like order for ratio1 ($\sigma_B = 110 \text{ nm}$, $Z_{\text{eff},B} = 242$), which in contrast to particles A is even strongly enhanced for ratio5 ($\sigma_B = 150 \text{ nm}$, $Z_{\text{eff},B} = 450$). The reasons for the observed influences of surface charges on particle self-organisation are discussed in detail for binary mixtures in section 5.2.2. The rigid ordering leads to a decreased fluctuation of matrix particles, which results in an enhanced importance of memory effects due to long-living coordination cages slowing down tracer self-diffusion in the long-time domain. Hence even though the liquid-like order of particles A is somewhat reduced, the pronounced ordering of particles B causes the decline of $D_S(t = x)/D_S(0)$ observed for tracers in Fig. 6.3 with increasing size and charge asymmetry of matrix particles.

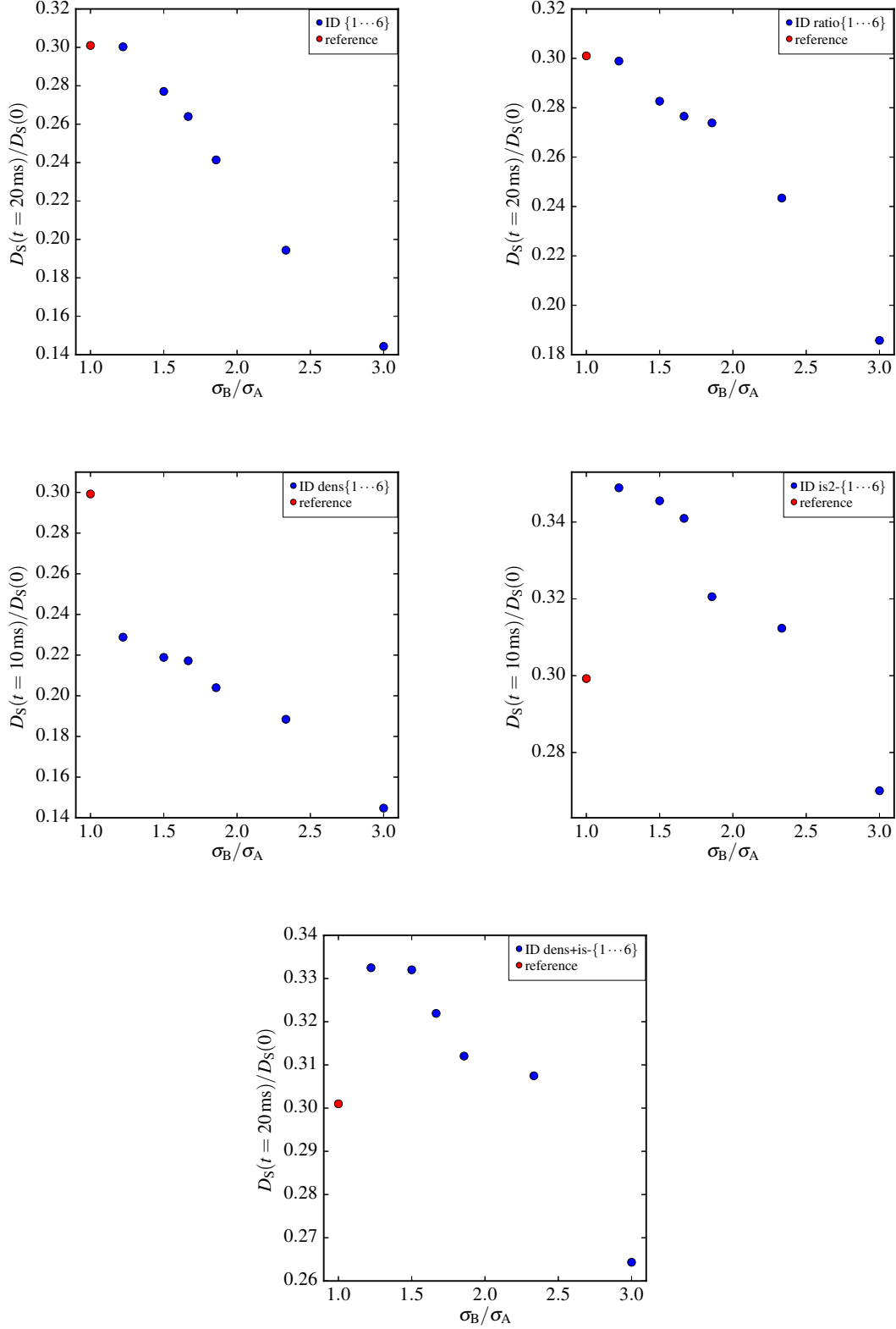


Fig. 6.3: Normalised self-diffusion coefficients $D_S(t=x)/D_S(0)$ of simulated tracers in dependence on the matrix particle size ratio σ_B/σ_A at times x in the range $10 \text{ ms} \leq x \leq 20 \text{ ms}$, at which a long-time limit of the tracer self-diffusion is reached. For simulation sets presented a progressive decrease of long-time tracer self-diffusion is observed with growing matrix particle asymmetry.

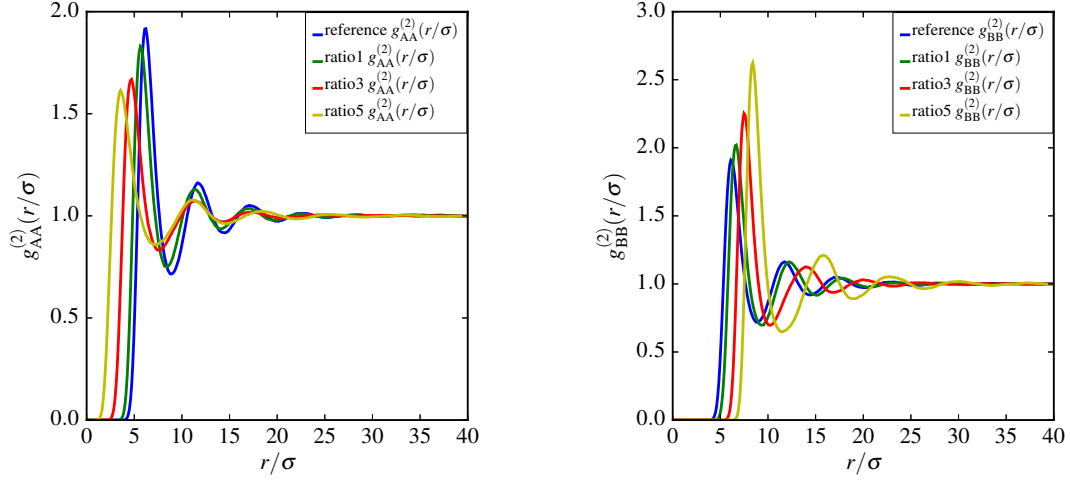


Fig. 6.4: Partial pair distribution functions $g_{AA}^{(2)}(r/\sigma)$ and $g_{BB}^{(2)}(r/\sigma)$ of matrix particles A and B obtained for simulations of the second set. $\sigma = 212$ nm designates the diameter of tracer particles. Despite a decreasing tendency, a liquid-like ordering is maintained among particles A with increasing matrix particle asymmetry. Simultaneously, the liquid-like order among particles B is significantly enhanced.

Long-time tracer self-diffusion independent of matrix asymmetry

Fig. 6.5 illustrates that for three of the simulation sets, the parameters of which are defined in tables 6.1 to 6.3, apparently no significant influence of size and charge asymmetry of matrix particles A and B affects the normalised long-time tracer self-diffusion $D_S(t = x)/D_S(0)$ within statistical accuracy. Here, x is a time in the range $5 \text{ ms} \leq x \leq 10 \text{ ms}$, at which a long-time limit of the tracer self-diffusion is reached.

The three simulation sets, this phenomenon is observed for, have an adjusted stray ion concentration of $c_{\text{stray}} \geq 2 \times 10^{-4} \text{ M}$ in common (cf. table 6.3). For the simulation with $c_{\text{stray}} = 2 \times 10^{-4} \text{ M}$, Fig. 6.6 exemplarily displays the influence of the ionic strength, resulting from a highly elevated stray ion concentration, on the structure of the matrix components A and B in terms of $g_{AA}^{(2)}(r/\sigma)$ and $g_{BB}^{(2)}(r/\sigma)$. Again, $\sigma = 212$ nm designates the tracer particle diameter. With respect to the partial pair distribution functions obtained for the reference, a drastic decline of liquid-like order is identified for both matrix components in the observed simulation. The electrostatic screening due to enhanced ionic strength results in a reduction of particle interactions strong enough, that merely a weak indication of a first coordination shell around a central particle is given by $g_{AA}^{(2)}(r/\sigma)$ and $g_{BB}^{(2)}(r/\sigma)$. Obviously, this effect is not significantly altered by increased size and charge asymmetry of matrix particles.

If any ordering of both matrix components is widely prohibited, the corresponding particles A and B underlie increased configuration fluctuations. These lead to only short-living coordination cages of matrix particles surrounding tracers. Hence the significance of memory effects influencing tracer self-diffusion is largely decreased. As size and charge asymmetry of matrix particles have no significant effect, due to the strong electrostatic screening, the long-time tracer self-diffusion coefficients presented in Fig. 6.5 remain almost constant.

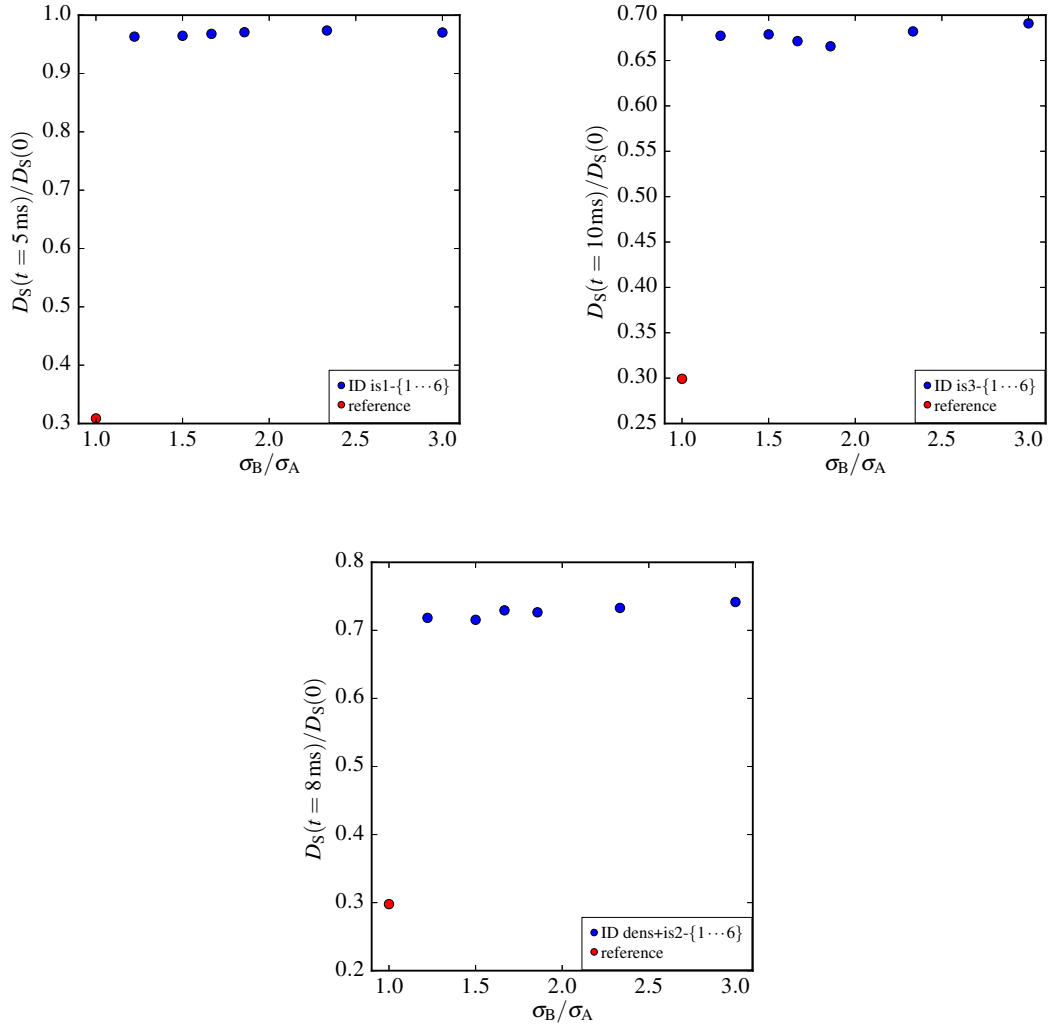


Fig. 6.5: Normalised self-diffusion coefficients $D_S(t = x)/D_S(0)$ of simulated tracers in dependence on the matrix particle size ratio σ_B/σ_A at times x in the range $5 \text{ ms} \leq x \leq 10 \text{ ms}$, at which a long-time limit of the tracer self-diffusion is reached. For simulation sets presented no significant influence on long-time tracer self-diffusion is observed with growing matrix particle asymmetry.

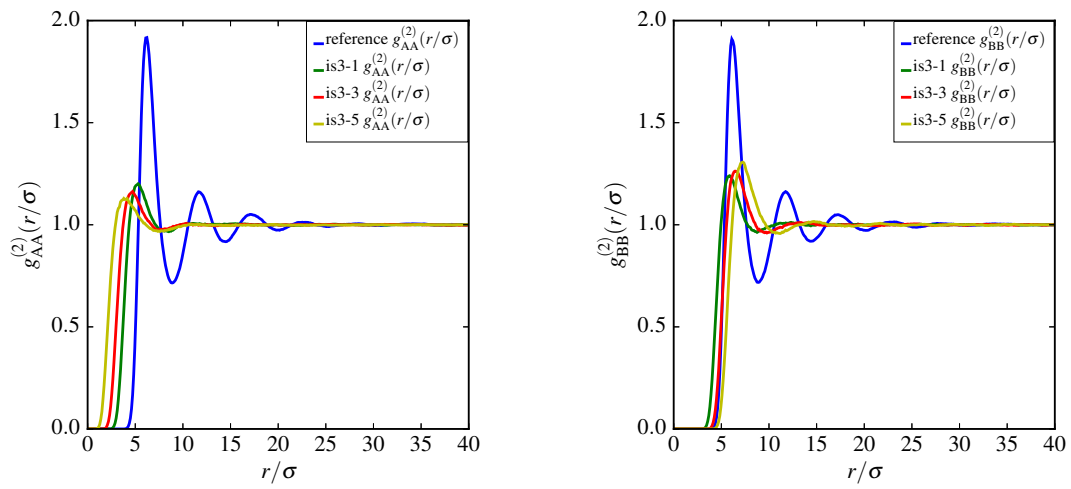


Fig. 6.6: Partial pair distribution functions $g_{AA}^{(2)}(r/\sigma)$ and $g_{BB}^{(2)}(r/\sigma)$ of matrix particles A and B obtained for simulations of the set with a stray ion concentration $c_{\text{stray}} = 2 \times 10^{-4}$ M. $\sigma = 212$ nm designates the diameter of tracer particles. The self-organisation to pronounced liquid-like order among particles A and B is widely prohibited by electrostatic screening. Merely a weak first coordination shell is recognisable in the displayed partial pair distribution functions. The investigated asymmetry of matrix particles apparently has no significant effect on structure formation among matrix particles.

7 Summary and outlook

Dispersions containing mixtures of different, highly charged polymer particles are less investigated up to now, since the composition of mixtures, in terms of the ratios of particles sizes, of the numbers of effective charges and of the number densities of the constituents, opens up a variety of additional parameters that affect the mesoscale structure and dynamics of colloidal mixtures. Furthermore, sophisticated experiments are required to access partial structural and dynamical properties of each constituent. Index-matching in light scattering experiments enables to selectively suppress contributions of one species, if the refractive index of the dispersion medium equals that of a selected particle class. Such experiments give access to structure and dynamics of the unmasked species on mesoscopic scales of space and time. Precondition for employing index-matching, however, is that colloidal stabilisation and particle interactions in the system are not altered by adjusting the refractive index of the dispersion medium. To meet this precondition different colloidal model systems are required, the refractive index of which can be matched by protic water/glycerol mixtures supporting the protolysis of acidic surface groups to maintain colloidal stability.

Theoretical access to structure and dynamics of colloidal mixtures is possible by Brownian Dynamics simulations of mixtures of charged particles. An extended Ermak algorithm, taking into account deterministic forces between differently charged particles and stochastic forces regarding interactions between dispersion medium and differently sized particles, allows for the calculation of particle trajectories in a colloidal mixture.

In this work, starting from well-known homocolloid precursors n-butyl acrylate (BA) and 1H,1H,5H-octafluoropentyl acrylate (OFPA) and the established copolymer constituent 2,2,2-trifluoroethyl acrylate (TFEA), a novel class of highly defined, charge-stabilised (co)polymer colloids is developed utilising emulsion polymerisation in aqueous media. By systematically changing the molar composition of the monomer mixture, a variety of colloidal dispersions of highly charged poly(TFEA) [pTFEA], poly(TFEA-co-BA) (pTcB), poly(TFEA-co-OFPA) (pTcO), and poly(OFPA) [pOFPA] particles is prepared with hydrodynamic particle radii R_h in a wide range of $22 \text{ nm} \leq R_h \leq 154 \text{ nm}$. By dynamic light scattering (DLS) experiments with highly diluted samples particle size distribution functions are determined employing the CONTIN algorithm. Fits of the size distributions by a Schulz-Flory distribution allow for a quantification of the polydispersity p of the (co)polymer particles. For more than half of the prepared polymer colloid dispersions very good uniformity indicated by $p < 0.1$ ($\text{PDI} < 0.01$) is identified. With few exceptions, remaining colloids exhibit moderate uniformity with $p < 0.2$ ($\text{PDI} < 0.04$). The ability of these new, charge-stabilised colloidal particles to self-organise to pronounced liquid-like order, even at unusually low volume fractions $\varphi < 0.005$, is proven by static light scattering (SLS) experiments. The obtained static structure factors $S(Q)$ of homo-colloidal systems are evaluated by employing integral equations, utilising the Ornstein-Zernike equation and the rescaled mean spherical approximation (RMSA) closure relation, which results in the determination of most probable coordination distances, particle number densities ${}^1\rho$ and the effective numbers of surface charges Z_{eff} .

By Brownian Dynamics (BD) simulations the known overestimation of Z_{eff} by RMSA is verified for the experimentally investigated systems and a rough tendency of increasing discrepancy between Z_{eff} (RMSA) and Z_{eff} (BD) is revealed for rising charge number.

The refractive index n_p of these colloidal particles, is determined by UV/VIS spectrophotometric transmission experiments exploiting the dependence of the scattered intensity on the squared difference of n_p and the refractive index of the dispersion medium n_m . It is found, that depending on particle composition, n_p of colloidal particles consisting of the acrylates mentioned above is freely tunable in the range $1.380 \leq n_p \leq 1.449$, enabling index-matching in protic water/glycerol mixtures as dispersion media. By analysis of the static structure factors obtained by SLS for homocolloidal dispersions with identical particles and number densities in different water/glycerol dispersion media, it is shown explicitly for the first time that a decreased protic character of the dispersion medium up to a glycerol mass content of 50 % does not alter the effective number of surface charges. Hence index-matching in such dispersion media will not influence the structure and dynamics of colloidal particles beyond effects related to changes in permittivity and dynamic viscosity, which can easily be taken into account in a theoretical description of the system.

The latter discovery is of critical significance for chapter 5, as therein light scattering experiments with binary mixtures of charge stabilised colloidal particles are performed, while selectively index-matching one component and thus excluding contributions of that species from the detected scattering signal. In case of binary mixtures consisting of strongly scattering polystyrene tracers in an index-matched matrix of pTFEA particles the time-dependent self-diffusion behaviour of the tracers is investigated by means of DLS in the interval $10^{-5} \text{ s} \leq t \leq 2 \times 10^{-2} \text{ s}$ of delay times t . Comparison of BD simulation results of binary mixtures with similar composition as the experimental system leads to very good agreement of the normalised time-dependent self-diffusion coefficient in the short-time domain. For the long-time limit successively better compliance, quantified by deviations of less than half an order of magnitude, is observed for simulations progressively approaching the experimental number ratio of tracer and matrix components. The intermediate time region of the tracer self-diffusion coefficient, however, exhibits significant discrepancies between simulation and experiment, the origin of which could not be resolved in this work and may be an interesting object of future investigations. By DLS also short-time (D_S^S) and long-time (D_S^L) tracer self-diffusion coefficients at varying tracer and matrix particle number densities are explicitly quantified. Expectedly, the ratio D_S^L/D_S^S shows no significant dependence on a decreasing tracer number density, but is considerably increased by reducing the matrix number density. These experimental findings complement studies of tracer self-diffusion in binary mixtures of charged colloidal spheres depending on electrostatic screening by Härtl et al. and theoretical investigations of tracer self-diffusion in such systems by Klein and Nägele et al.

For binary mixtures with similar number densities of the colloidal constituents the determination of partial, static structure factors $S_{ij}(Q, 0)$ by means of SLS experiments is illustrated. Therein, one of the two components consisting of newly developed copolymer particles with tunable, low refractive index is selectively index-matched by a water/glycerol dispersion medium of corresponding composition. With assisting BD simulations it is shown, that even small deviations of well below one percent between the refractive index of the medium, n_m , and that of the particles to be index-matched, n_p , lead to significant contributions of other correlations to the scattering signal. Hence, a particular diligence in exactly index-matching one of the two components is emphasised, to enable a successful determination of partial structure factors from colloidal mixtures by

scattering experiments. Future DLS investigations could comprise the extension to a time-dependent evaluation of field autocorrelation functions $g_1(Q, \tau)$ to gain an experimental access to partial, intermediate scattering functions $S_{ij}(Q, t)$.

In contrast to experimental methods, BD simulations provide a comparably easy access to $S_{ij}(Q, t)$ of binary colloidal mixtures, which is verified within this work. The development of a sophisticated, highly parallel algorithm to correlate pairs of particles in space and time, based on the simulated trajectories, leads to the determination of distinct, partial pair distribution functions $g_{ij}^{(2)}(r, t)$ that are spatially Fourier transformed into $S_{ij}(Q, t)$. For the first time, investigations of systematic variations of particle sizes, numbers of effective surface charges, number densities, and the system temperature are performed by BD simulations to result in a comprehensive study of those influences on binary mixtures of charged colloidal spheres. It is found that a changing temperature, due to a competition of electrostatic repulsion and thermal energy working in different directions, and varying particle sizes do not affect the structure identified in mixtures in a significant manner, as long as a region of thermal stability is observed. A strong enhancing of the formed structures, however, is recognised for correlations, in which particles with increasing effective charges or number ratios are involved. These insights are complemented by indications of non-trivial, indirect influences, resulting from the interplay of both sub-systems in a binary mixture.

Similar, indirect phenomena are found with regard to the collective dynamics of the simulated systems. Due to the strong influence on the dynamic viscosity of the chosen dispersion medium water, a changing temperature exhibits the most dramatic effects on the relaxation of obtained intermediate scattering functions. In comparison, the influences of variations in number densities, particle sizes and effective charges are found to be significant but rather small with respect to temperature effects on collective dynamics in water. For selected examples of BD simulations collective short-time and long-time diffusion coefficients are quantified by fitting single exponential functions to the corresponding regions of the intermediate scattering functions at a given scattering vector Q . Future studies may comprise extensions of the interactions under investigation in the observed mixtures, e. g., to hydrodynamic interactions which have not been considered for the BD simulations in this work.

The addition of tracer particles to a matrix of two different colloidal species with comparable number densities defines a realistic ternary mixture, giving rise to even more complex systems. In this work, the tracer self-diffusion in such ternary mixtures is investigated for the first time by extensive BD simulations. It is shown, that, as might be expected, an increased overall colloidal number density leads to a slowing down of tracer self-diffusion, while adjusting an elevated ionic strength effects a faster diffusive motion of tracer particles, due to decreased electrostatic particle interaction resulting from electrostatic screening. With regard to a progressive size and charge asymmetry of the two matrix particle classes two different effects on long-time tracer self-diffusion are recognised. Below a threshold concentration of stray ions, for the performed simulations identified in the order of magnitude $c_{\text{stray}} \approx 10^{-4}$ M, a successive decrease of the long-time tracer self-diffusion coefficient D_S^L is observed with increasing matrix particle asymmetry. The reason for this is ascribed to long-living coordination cages capturing tracer particles, as a result of progressive order and reduced particle fluctuations in at least one of the two matrix components. Above the afore mentioned threshold stray ion concentration, electrostatic screening apparently causes a suppression of significant ordering and thus results in fast particle fluctuations in both matrix components, hence leading

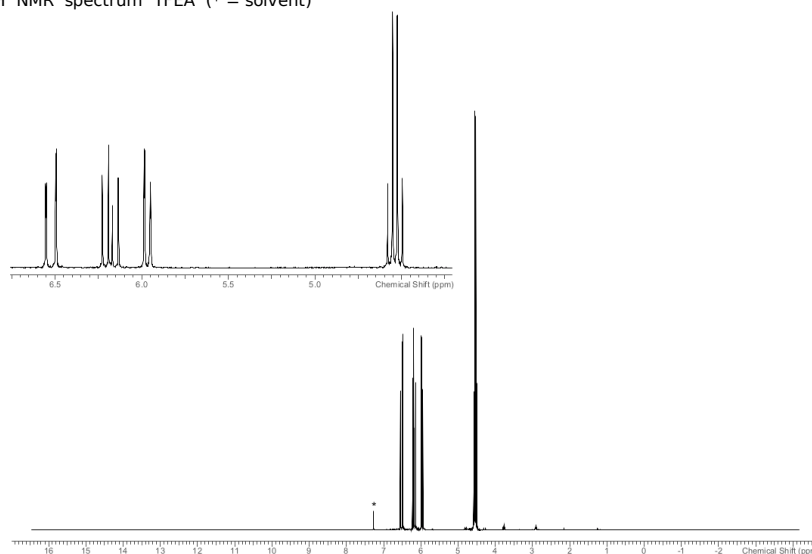
to short lifetimes of coordination cages surrounding tracers. Thus, the long-time tracer self-diffusion behaviour is observed to become independent of growing size and charge asymmetry of matrix particles under these circumstances.

The results obtained from BD simulations for ternary mixtures will need to be verified by experimental investigations in the future. The possibility of generating a binary matrix consisting of particles with different sizes and effective surface charges but the same refractive index is given by the availability of colloidal (co)polymer particles prepared in this work. Introducing, for example, strongly scattering PS particles to such a mixture while matching the refractive index of the dispersion medium to that of the matrix is a demanding preparative task but would enable experimental validation of simulation results provided by this work.

Appendix

A Nuclear magnetic resonance spectra of prepared fluorinated acrylates

^1H NMR spectrum TFEA (* = solvent)



^1H NMR spectrum OFPA (* = solvent)

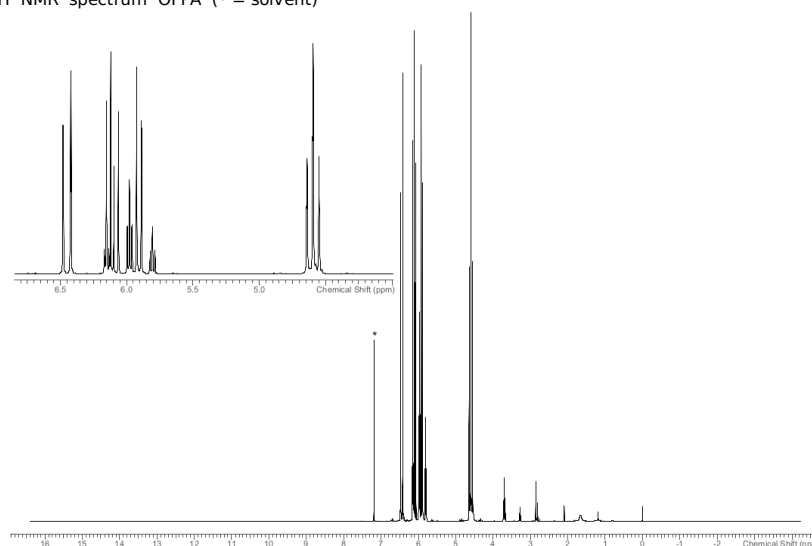
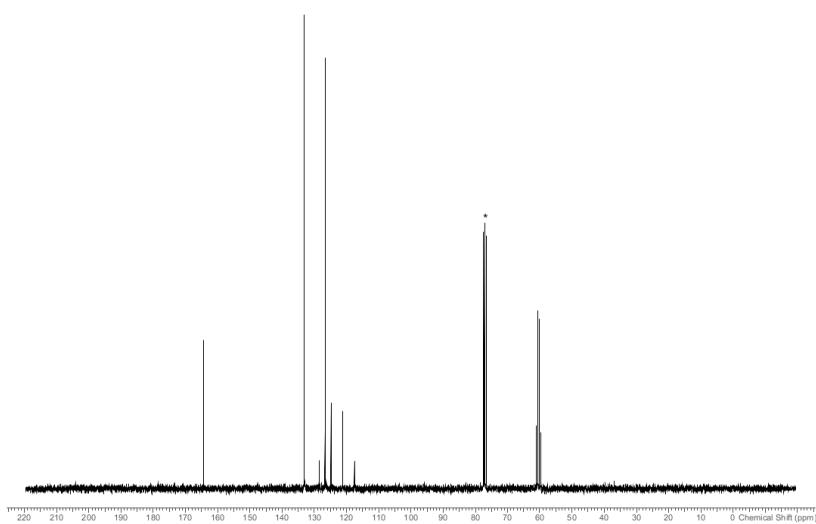


Fig. A.1: ^1H nuclear magnetic resonance (NMR) spectra of the prepared monomers 2,2,2-trifluoroethyl acrylate (TFEA) and 1H,1H,5H-octafluoropentyl acrylate (OFPA) with deuterated chloroform as solvent.

$^{13}\text{C}\{^1\text{H}\}$ NMR spectrum TFEA (* = solvent)



$^{13}\text{C}\{^1\text{H}\}$ NMR spectrum OFPA (* = solvent)

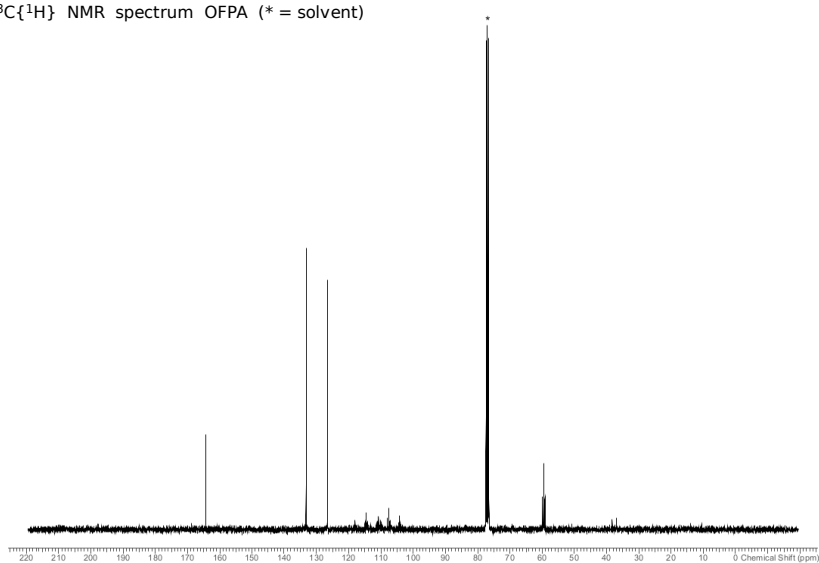
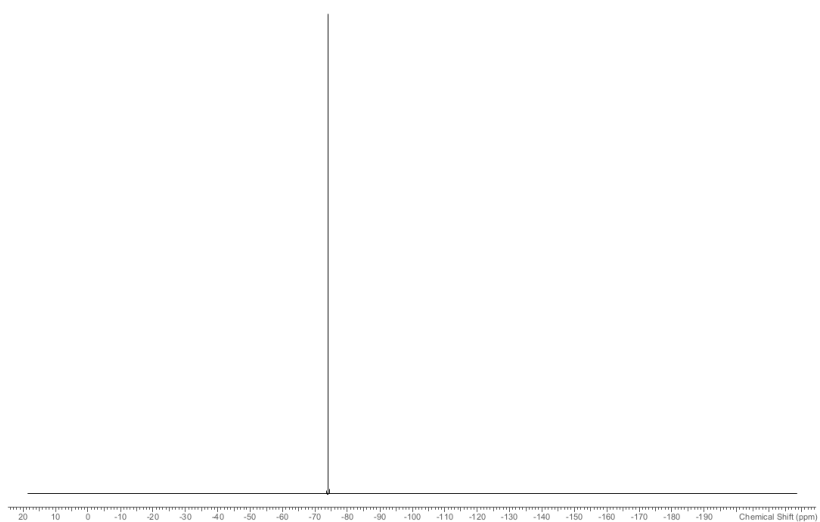


Fig. A.2: $^{13}\text{C}\{^1\text{H}\}$ NMR spectra of the prepared monomers TFEA and OFPA with deuterated chloroform as solvent.

$^{19}\text{F}\{^1\text{H}\}$ NMR spectrum TFEA



$^{19}\text{F}\{^1\text{H}\}$ NMR spectrum OFPA

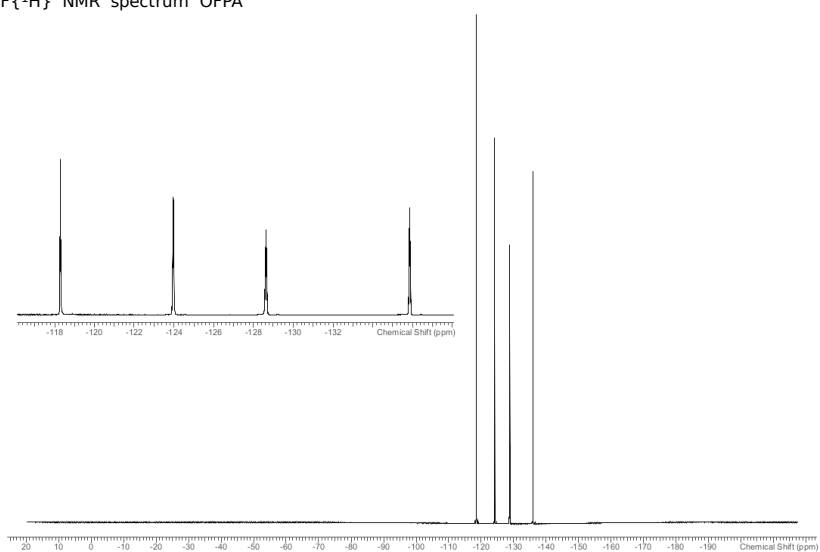


Fig. A.3: $^{19}\text{F}\{^1\text{H}\}$ NMR spectra of the prepared monomers TFEA and OFPA with deuterated chloroform as solvent.

B Intermediate scattering functions for BB and AB correlations

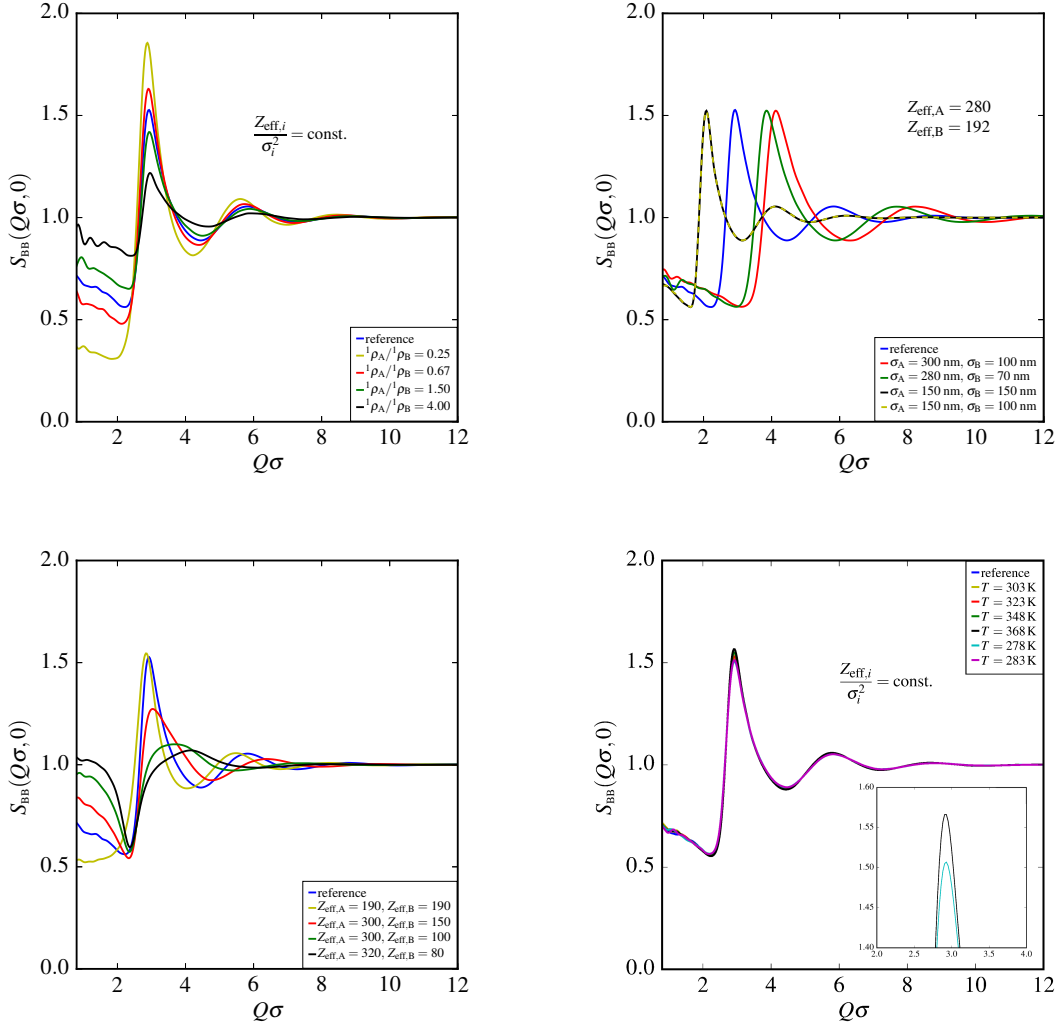


Fig. B.1: Intermediate scattering functions $S_{BB}(Q, 0)$ at $t = 0$ of BB correlations obtained from BD simulations: under variation of the number density ratio $1/\rho_A/1/\rho_B$ (upper left), with different numbers of surface charges $Z_{eff,A}$ and $Z_{eff,B}$ (lower left), varying the particle diameters σ_A and σ_B (upper right), and changing the temperature T of the system (lower right). The reduced scattering vector $Q\sigma$ is displayed with $\sigma = \sigma_A$.

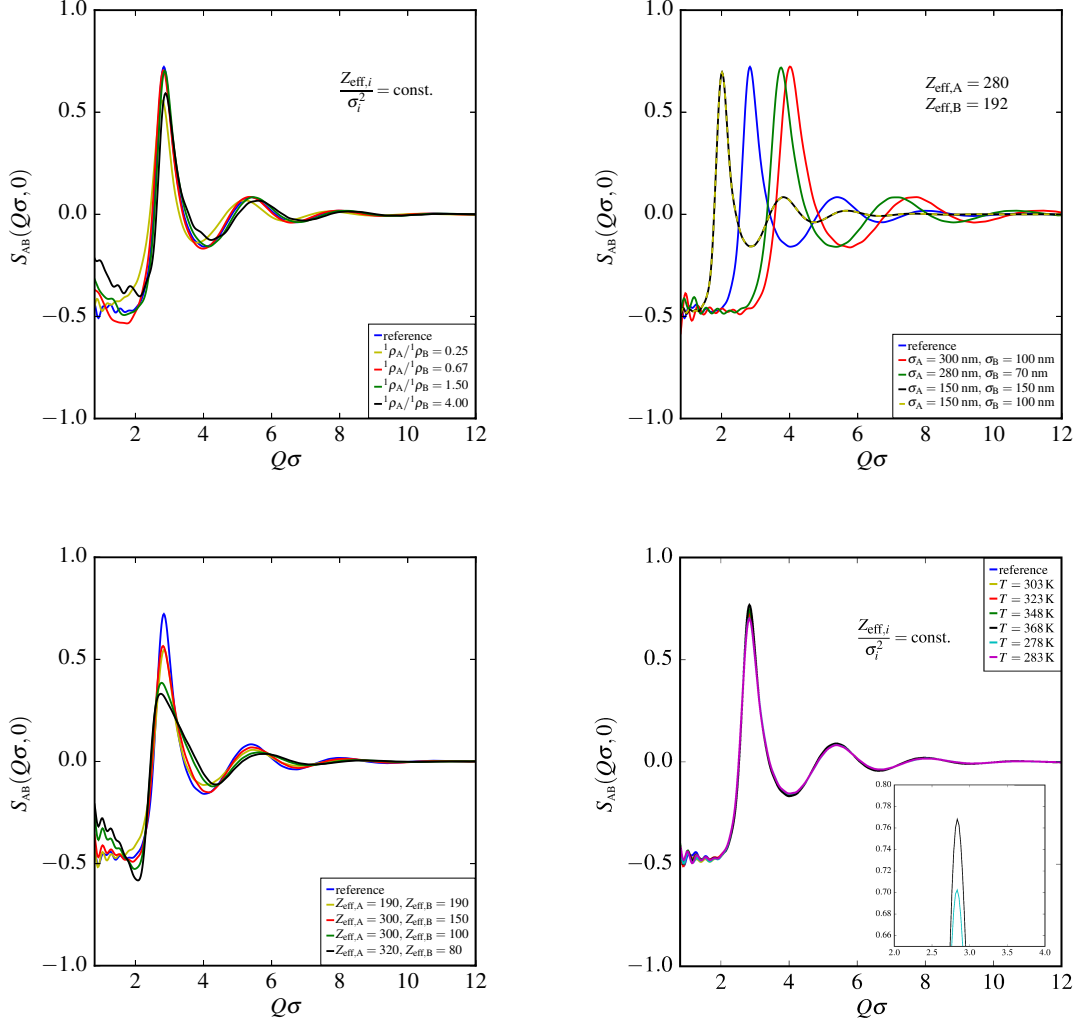


Fig. B.2: Intermediate scattering functions $S_{AB}(Q, 0)$ at $t = 0$ of AB correlations obtained from BD simulations: under variation of the number density ratio ${}^1\rho_A/{}^1\rho_B$ (upper left), with different numbers of surface charges $Z_{\text{eff},A}$ and $Z_{\text{eff},B}$ (lower left), varying the particle diameters σ_A and σ_B (upper right), and changing the temperature T of the system (lower right). The reduced scattering vector $Q\sigma$ is displayed with $\sigma = \sigma_A$.

C Relaxation of intermediate scattering functions for BB and AB correlations

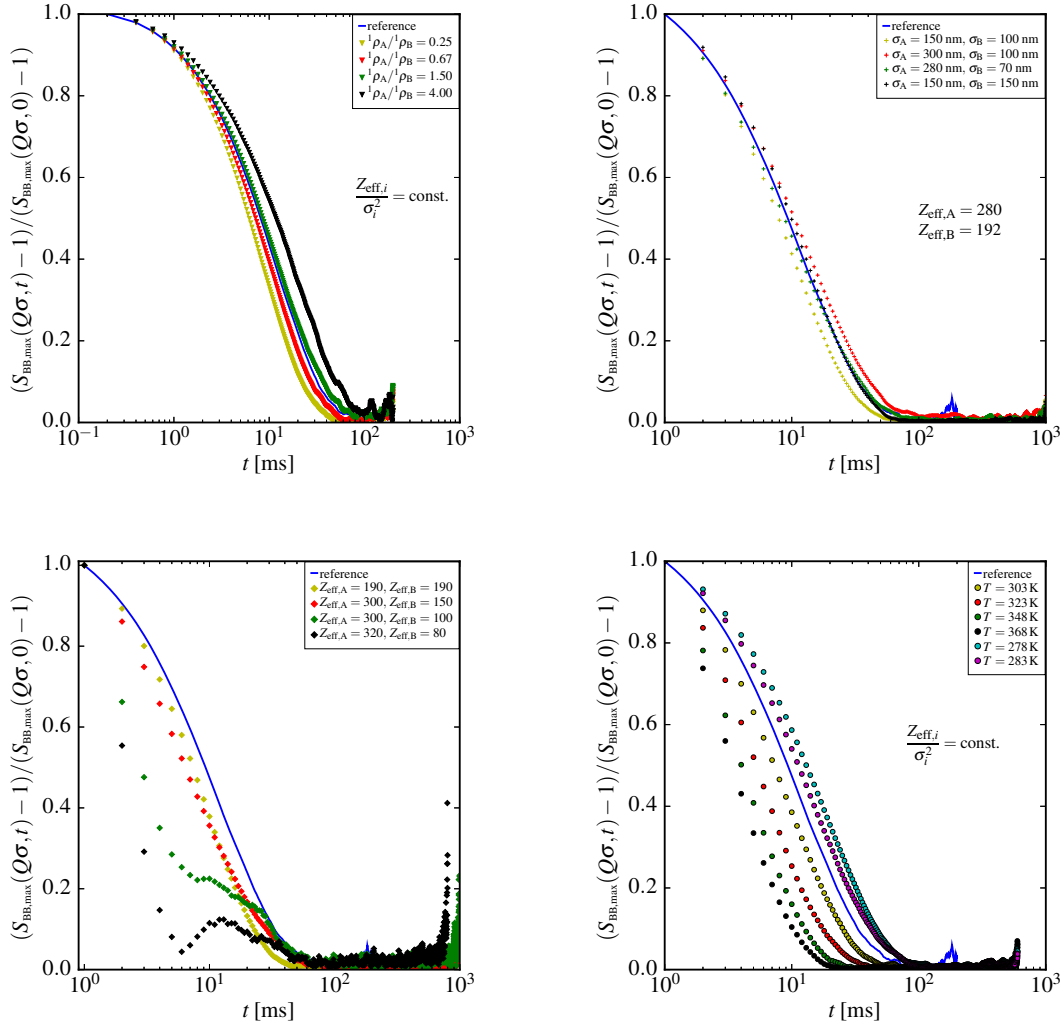


Fig. C.1: Normalised relaxation of the global maxima of partial intermediate scattering functions $S_{BB,max}(Q\sigma, t)$ obtained by BD simulations under variation of: the number density ratio ${}^1\rho_A/{}^1\rho_B$ (upper left), numbers of surface charges $Z_{eff,A}$ and $Z_{eff,B}$ (lower left), particle diameters σ_A and σ_B (upper right), and the system temperature T (lower right). The reduced scattering vector $Q\sigma$ is displayed with $\sigma = \sigma_A$.

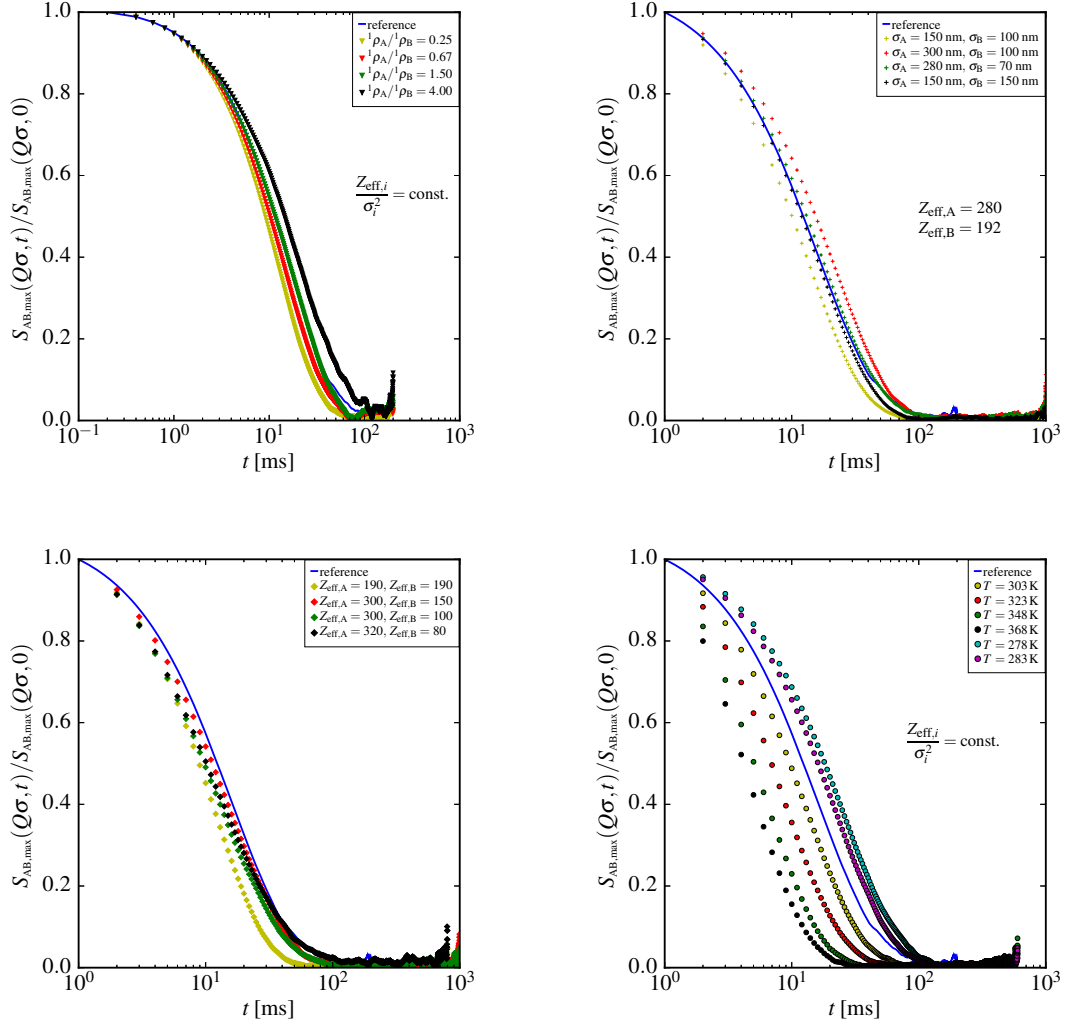


Fig. C.2: Normalised relaxation of the global maxima of partial intermediate scattering functions $S_{AB,\max}(Q\sigma, t)$ obtained by BD simulations under variation of: the number density ratio ${}^1\rho_A/{}^1\rho_B$ (upper left), numbers of surface charges $Z_{\text{eff},A}$ and $Z_{\text{eff},B}$ (lower left), particle diameters σ_A and σ_B (upper right), and the system temperature T (lower right). The reduced scattering vector $Q\sigma$ is displayed with $\sigma = \sigma_A$.

List of Figures

2.1	Typical geometry of a scattering event caused by interaction of light with matter. The angle between the wave vectors of incident wave \mathbf{k}_i and scattered wave \mathbf{k}_f is designated as ϑ . The wave vector difference $\mathbf{Q} = \mathbf{k}_i - \mathbf{k}_f$ is the scattering vector.	8
2.2	Extract of the calculated form factor $P(QR)$ for uniform spherical particles with radius $R = 300$ nm according to (2.8). The first minimum is always observed at $QR \approx 4.49$	9
2.3	Examples for an intensity autocorrelation function $g_2(\tau)$, determined by means of a homodyne scattering experiment, and the corresponding field autocorrelation function $g_1(\tau)$, obtained using the Siegert equation (2.14).	12
2.4	Typical time dependency of the mean squared displacement $\langle r^2 \rangle$ of Brownian particles. The different slopes at very short and long times correspond to a short-time and a long-time self-diffusion coefficient D_S^S and D_S^L , respectively, which generally relate to each other as $D_S^L \leq D_S^S$. In between these limits there is a sub-diffusive region caused by memory effects.	14
2.5	Typical structure factor $S(Q)$ of a liquid-like ordered colloidal dispersion of charged particles and the corresponding collective short-time diffusion coefficient normalised to the self-diffusion coefficient $D_{\text{eff}}(Q)/D_0$. Maxima in $S(Q)$ indicate preferred, more stable configurations leading to a slowed down particle motion, while more unstable configurations marked by minima in $S(Q)$ are not favoured, which causes a faster collective motion on length scales $d \approx 2\pi/Q$	15
3.1	Schematic representation of the homodyne setup employed for light scattering experiments in this work (redrawn with permission from [94]). A detailed description is given in the text.	20
3.2	Linear dependence of the relaxation rate $\Gamma(Q)$ on Q^2 for non-interacting spherical particles. According to the Landau-Placzek relation $\Gamma(Q) = D_E Q^2$ the slope of the straight line defines the Einstein diffusion coefficient D_E of the observed particles.	22
3.3	Illustration of the experimental determination of the static structure factor $S(Q)$ by static light scattering. The scattering function of an ordered sample is normalised to the form factor $P(Q)$, obtained by a fit to the scattering function of a dilute, disordered sample resulting from a separate light scattering experiment. Simultaneously normalising the scattering functions to the number densities of the corresponding samples, leads to $S(Q)$, here multiplied by 10^5 for reasons of display.	23

3.4	The pair distribution function $g^{(2)}(r/\sigma)$, in dependence on the normalised distance r/σ with the particle diameter σ , as gained by BD simulations, is restricted to $r = R_c$. $g^{(2)}(r/\sigma)$ is extrapolated by a damped oscillating function according to (3.11) fit to the simulated data. Hereby artefacts due to truncation effects after Fourier-Bessel transform to obtain the static structure factor $S(Q\sigma)$ are avoided.	25
4.1	Particle size distributions of six examples of the prepared polymer colloids obtained from DLS data via the CONTIN algorithm. Red curves represent fit functions according to a Schulz-Flory distribution, which are employed for determination of the polydispersity p	31
4.2	Left: Relaxation rate $\Gamma(Q)$ acquired from initial slopes of $g_1(Q, \tau)$ determined by DLS for the example colloid pTFEA II. The linear dependence of $\Gamma(Q)$ on Q^2 verifies free Gaussian diffusion of the particles. According to (2.16) the slope gives the self-diffusion coefficient D_0 . Right: Illustration of the linear proportionality between D_0^{-1} and the most probable hydrodynamic particle radii $R_{h,max}$ of the prepared colloids, meeting the Stokes-Einstein equation (2.17).	32
4.3	Dependency of the weighted relative attenuation $\Phi(n_m)$ on the refractive index of the dispersion medium n_m , measured for the system pTcB-50 IV in a photometric transmission experiment with a wavelength $\lambda = 532$ nm. The vertex of the expected minimum indicates the index-matching point, where $n_p = n_m$, thus revealing the particle refractive index $n_p = 1.433$. . .	33
4.4	Dependence of the mean refractive index $\langle n_p \rangle$ of pTFEA, pTcB, and pBA particles on the molar fraction of butyl acrylate, x_{BA} , in the corresponding monomer mixture. For copolymers a linear increase of $\langle n_p \rangle$ is observed proportional to x_{BA} . The homopolymers at $x_{BA} = 0$ (pTFEA) and $x_{BA} = 1$ (pBA) somewhat deviate from this linear behaviour. As indicated by dashed lines for refractive indices of water and glycerol, all displayed types of (co)polymer particles can be index-matched in water/glycerol mixtures.	34
4.5	Left: Determination of the static structure factor $S(Q)$ for the example system pTcB-70 I by SLS. Blue triangles show the scattering function of a dilute sample of pTcB-70 I, that contains 10^{-3} M KCl to avoid electrostatic particle interactions. The red curve is a fit to this function according to the theoretical form factor of Schulz-Flory distributed spheres $P(Q)$. Green circles mark the scattering function obtained for a concentrated sample of pTcB-70 I. Normalising the latter function to the $P(Q)$ -fit and taking into account the ratio of number densities of the investigated samples results in $S(Q)$, here multiplied by 10^5 for better display. Right: RMSA fit to the static structure factor determined for pTcB-70 I. Experimental data and fit show excellent agreement around the coordination maximum, which gives access to the particle number density ${}^1\rho$ and the number of surface charges Z_{eff} of the probed system. Further details are discussed in the text below.	35
4.6	Static structure factors and corresponding RMSA fits of colloidal dispersions with particularly low volume fractions φ : pTFEA IIc (upper left, $\varphi = 2.0 \times 10^{-3}$), pTcB-10 IIc (upper right, $\varphi = 1.2 \times 10^{-3}$), and pTcO-30 (lower centre, $\varphi = 0.6 \times 10^{-3}$). Despite these low volume fractions pronounced liquid-like structures are formed.	38

4.7	Determination of the surface charge number Z_{eff} by comparison of the static structure factor $S(Q\sigma)$ obtained by SLS experiments and RMSA fit to $S(Q\sigma)$ resulting from BD simulations for the example system pTcO-30. The equilibrium structure at $Z_{\text{eff}} = 200$ (upper left) exhibits a structure factor, that is higher than the one determined by experiment. A simulation with $Z_{\text{eff}} = 180$ (upper right) delivers a $S(Q\sigma)$ which is slightly too small. The lower centre graphic corresponding to $Z_{\text{eff}} = 182$ shows a static structure factor obtained from BD in excellent agreement to the SLS result.	39
4.8	Static structure factors of pTcB-70 I particles dispersed in water/glycerol media with six different glycerol mass ratios ω_{gly} in the range $10\% \leq \omega_{\text{gly}} \leq 50\%$. Within a small uncertainty the particle number ratios ${}^1\varrho$ are identical. In good approximation the number of surface charges Z_{eff} is proven independent from the water/glycerol dispersion medium up to $\omega_{\text{gly}} = 50\%$	42
5.1	Left: Particle size distribution for PS3 obtained by DLS employing the CONTIN algorithm, resulting in a most probable hydrodynamic radius $R_{\text{h,max}} = 106$ nm. The polydispersity $p = 0.130$ is derived from a Schulz-Flory fit according to eq. (3.10). Right: Transmission electron micrograph of PS3 spheres, taken at the Centre for Electron Microscopy of the Universitätsmedizin Rostock (EMZUniRo).	44
5.2	Schematic illustration of the preparation of samples investigated in this section. Starting from the stock binary mixture consisting of pTFEA VI and PS3 in the ratio 200:1, a first set of samples with constant matrix number density ${}^1\varrho_{\text{matrix},0}$ and decreasing tracer number density ${}^1\varrho_{\text{PS3}}$ is prepared. Continuing from the sample with ${}^1\varrho_{\text{PS3}} = 0.50 {}^1\varrho_{\text{PS3},0}$ a second sample set with progressively reduced matrix number density ${}^1\varrho_{\text{matrix}}$ is prepared, while the tracer number density remains at ${}^1\varrho_{\text{PS3}} = 0.50 {}^1\varrho_{\text{PS3},0}$	45
5.3	Scattering functions $I(Q)$ of binary mixtures of PS3 tracers and pTFEA VI determined by SLS. On the left results for the first sample set with varying tracer number density are shown, while the graphic on the right presents $I(Q)$ for samples with varying matrix number density. In both pictures the scattering function of a highly diluted sample of pure PS3 containing 10^{-3} M KCl is included for comparison. Graphs obtained for the mixtures do not significantly differ from that of pure PS3.	46
5.4	Determination of a hypothetical static structure factor $S(Q)$ for the binary mixture with matrix number density ${}^1\varrho_{\text{matrix},0}$ and tracer number density ${}^1\varrho_{\text{PS3}} = 0.5 {}^1\varrho_{\text{PS3},0}$. The scattering function $I(Q)$ of the mixture and the form factor $P(Q)$ of pure PS3 are identical within experimental accuracy, such that $S(Q) \approx 1$ over the observed Q -range, which proves successful index-matching of the pTFEA VI matrix.	47
5.5	Upper left: Example field autocorrelation function $g_1(\tau)$ at $Q = 2.308 \times 10^{-2} \text{ nm}^{-1}$ obtained by DLS with one of the binary mixtures employing the Siegert relation (2.14). Upper right: Example short-time fit of $g_1(\tau)$ to determine the initial slope, which is the negative relaxation rate $-\Gamma$. Bottom row: Plots of short-time $\Gamma(Q)$ vs. Q^2 for the first (left) and second (right) set of binary mixtures in comparison to $\Gamma(Q)$ for a sample of highly diluted, pure PS3 containing 10^{-3} M KCl.	48

5.6	Upper left: Example field autocorrelation function $g_1(\tau)$ at $Q = 2.308 \times 10^{-2} \text{ nm}^{-1}$ obtained by DLS with one of the binary mixtures employing the Siegert relation (2.14). Upper right: Example long-time fit of $g_1(\tau)$ to determine the slope, which is the negative relaxation rate $-\Gamma$. Bottom row: Plots of long-time $\Gamma(Q)$ vs. Q^2 for the first (left) and second (right) set of binary mixtures in comparison to $\Gamma(Q)$ for a sample of highly diluted, pure PS3 containing 10^{-3} M KCl	50
5.7	Illustration of the ratio of long-time and short-time self-diffusion coefficients of tracer particles D_S^L/D_S^S determined for binary mixtures with varying tracer number density ${}^1\rho_{\text{PS3}}$ (left) and with varying matrix number density ${}^1\rho_{\text{matrix}}$ (right). A decrease of ${}^1\rho_{\text{PS3}}$ down to a fourth of the original density shows no significant influence on D_S^L/D_S^S , while a decline of ${}^1\rho_{\text{matrix}}$ leads to an increase of D_S^L/D_S^S , which is strong at first and becoming weaker with decreasing matrix number density. The addition of 10^{-3} M KCl largely enhances D_S^L/D_S^S	52
5.8	Magnification of the low Q region of the lower right graphic of Fig. 5.6, presenting the long-time relaxation rates $\Gamma(Q)$ determined for binary mixtures with varying matrix number density ${}^1\rho_{\text{matrix}}$. A tendency of an increased slope with decreasing ${}^1\rho_{\text{matrix}}$ is apparent, indicating an enhanced long-time self-diffusion of the tracer particles.	53
5.9	Mean squared displacements $\langle r^2 \rangle$ of tracer and matrix particles determined from trajectories obtained by BD simulations of binary mixtures with three different compositions. Graphs are labelled with "TracerXX" and "MatrixYY", where "XX" and "YY" give the percentage molar ratios of the respective component.	55
5.10	Time-dependent self-diffusion coefficients $D_S(t)$ of PS3 tracers in a matrix of pTFEA VI determined by DLS experiments and BD simulations. Each $D_S(t)$ is normalised to its starting value $D_S(0)$. The key gives the molar ratio of the components of the mixture as A : B, where A denotes the tracers and B the matrix.	57
5.11	Approximation of the short-time limit of the partial intermediate scattering function $S_{\text{BB}}(Q, 0)$ of pTcB-30 II particles in a binary mixture with pOFPA III particles. Due to a deliberate mismatch between refractive indices of the water/glycerol dispersion medium, $n_m = 1.377$, and of pOFPA III particles, $n_A = 1.380$, contributions of AA and AB correlations to the presented partial intermediate scattering function are assumed.	59
5.12	Left: Partial pair distribution functions $g_{ij}^{(2)}(r/\sigma)$ obtained by BD simulations of a binary mixture corresponding to the experimentally investigated system. Right: Partial static structure factors $S_{ij}(Q\sigma)$ determined by Fourier-Bessel transform of $g_{ij}^{(2)}(r/\sigma)$. Here, $\sigma = \sigma_A$, i. e., the particle diameter of pOFPA III. For better display, the mixed correlation structure factor is presented as $S_{\text{AB}}(Q\sigma) + 1$	61

5.13	Comparison of the static intermediate scattering functions $S_{BB}(Q, 0)$ determined by DLS and BD simulation. Calculation of the effective structure factor $I(Q)/I'(Q)$ according to eq. (5.2) proves that, due to incomplete index-matching of pOFPA III, actually a linear combination of $S_{AA}(Q, 0)$, $S_{AB}(Q, 0)$, and $S_{BB}(Q, 0)$ is detected by DLS. Hence the imperative of exact index-matching for the determination of partial scattering functions in mixtures is clarified.	62
5.14	Qualitative presentation of a typical space-time pair distribution function $g^{(2)}(r, t)$. The representation $g^{(2)}(r, t = 0)$ vs. r exhibits the damped oscillation known for the static pair distribution function of a liquid-like ordered system. In the representation $g^{(2)}(r, t)$ vs. t , a temporal decay indicates the progressive loss of correlation between two particles over time at a given particle distance r	63
5.15	Time-dependencies of the partial intermediate scattering functions $S_{ij}(Q\sigma, t)$. These result from Fourier-Bessel transform of partial space-time pair distribution functions $g_{ij}^{(2)}(r/\sigma, t)$ obtained by BD simulations of the experimental binary mixture of pOFPA III and pTcB-30 II. The reduced scattering vector $Q\sigma$ is displayed with $\sigma = \sigma_A = 212$ nm. Relaxation times of the intermediate scattering functions scale with the strength of correlation quantified by the global maxima of $S_{ij}(Q\sigma, t)$ relative to the corresponding baseline.	64
5.16	Partial intermediate scattering functions $S_{ij}(Q\sigma, t)$ and normalised temporal relaxation functions characterising the reference system modelled by BD simulations. The reduced scattering vector $Q\sigma$ is displayed with $\sigma = \sigma_A = 212$ nm.	68
5.17	Intermediate scattering functions $S_{AA}(Q, 0)$ at $t = 0$ of AA correlations obtained from BD simulations: under variation of the number density ratio ${}^1\rho_A/{}^1\rho_B$ (upper left), with different effective surface charges $Z_{\text{eff},A}$ and $Z_{\text{eff},B}$ (lower left), varying the particle diameters σ_A and σ_B (upper right), and changing the temperature T of the system (lower right). The reduced scattering vector $Q\sigma$ is displayed with $\sigma = \sigma_A$	69
5.18	Distinct pair distribution functions $g_{AB}^{(2)}(r/\sigma, t)$ at $t = 0$ obtained by BD simulations with varied numbers of surface charges $Z_{\text{eff},A} = 300, Z_{\text{eff},B} = 150$ and $Z_{\text{eff},A} = 300, Z_{\text{eff},B} = 100$. The reduced distance r/σ is displayed with $\sigma = \sigma_A$. It can be seen, that for a lower charge number $Z_{\text{eff},B}$ particles B may be located slightly closer to a central particle A than for a larger charge number $Z_{\text{eff},B}$	72
5.19	Normalised relaxation of the global maxima of partial intermediate scattering functions $S_{AA,\text{max}}(Q\sigma, t)$ obtained by BD simulations under variation of: the number density ratio ${}^1\rho_A/{}^1\rho_B$ (upper left), effective surface charges $Z_{\text{eff},A}$ and $Z_{\text{eff},B}$ (lower left), particle diameters σ_A and σ_B (upper right), and the system temperature T (lower right). The reduced scattering vector $Q\sigma$ is displayed with $\sigma = \sigma_A$	74

5.20	Normalised temporal relaxation functions of $S_{AA,\max}(Q\sigma, t)$ determined for BD simulations with differing particle diameters σ_A and σ_B . Renormalisation of the delay time t to the respective diameter σ_A (left) leads to slight deviations remaining between the presented relaxation functions, while renormalisation of the delay time t to the corresponding sum of particle diameters $\sum \sigma_i = \sigma_A + \sigma_B$ (right) leads to identity of all presented relaxation functions.	76
5.21	Time relaxation functions for the maxima of the partial intermediate scattering functions $S_{ij,\max}(Q\sigma, t)$ with $\sigma = \sigma_A = 212$ nm obtained for the simulated reference system. Respectively fitting a single exponential function to short-time and long-time data, identifies two different diffusive regions, for which corresponding collective short-time and long-time diffusion coefficients can be determined. In between the two limits, a sub-diffusive region is recognised, in which collective diffusion is time-dependent.	77
6.1	Time dependency of the normalised tracer self-diffusion coefficients $D_S(t)/D_S(0)$ determined for the eight simulation sets of ternary mixtures investigated. Displayed are results for the first three ratios of matrix particle diameters σ_A and σ_B . Integers in the keys designate these ratios as: " $\sigma_A/\text{nm} : \sigma_B/\text{nm}$ ". The tracer self-diffusion coefficient obtained for the reference simulations is provided for comparison.	81
6.2	Time dependency of the normalised tracer self-diffusion coefficients $D_S(t)/D_S(0)$ determined for the eight simulation sets of ternary mixtures investigated. Displayed are results for the remaining three ratios of matrix particle diameters σ_A and σ_B . Integers in the keys designate these ratios as: " $\sigma_A/\text{nm} : \sigma_B/\text{nm}$ ". The tracer self-diffusion coefficient obtained for the reference simulations is provided for comparison.	82
6.3	Normalised self-diffusion coefficients $D_S(t = x)/D_S(0)$ of simulated tracers in dependence on the matrix particle size ratio σ_B/σ_A at times x in the range $10 \text{ ms} \leq x \leq 20 \text{ ms}$, at which a long-time limit of the tracer self-diffusion is reached. For simulation sets presented a progressive decrease of long-time tracer self-diffusion is observed with growing matrix particle asymmetry.	84
6.4	Partial pair distribution functions $g_{AA}^{(2)}(r/\sigma)$ and $g_{BB}^{(2)}(r/\sigma)$ of matrix particles A and B obtained for simulations of the second set. $\sigma = 212$ nm designates the diameter of tracer particles. Despite a decreasing tendency, a liquid-like ordering is maintained among particles A with increasing matrix particle asymmetry. Simultaneously, the liquid-like order among particles B is significantly enhanced.	85
6.5	Normalised self-diffusion coefficients $D_S(t = x)/D_S(0)$ of simulated tracers in dependence on the matrix particle size ratio σ_B/σ_A at times x in the range $5 \text{ ms} \leq x \leq 10 \text{ ms}$, at which a long-time limit of the tracer self-diffusion is reached. For simulation sets presented no significant influence on long-time tracer self-diffusion is observed with growing matrix particle asymmetry.	86

6.6	Partial pair distribution functions $g_{AA}^{(2)}(r/\sigma)$ and $g_{BB}^{(2)}(r/\sigma)$ of matrix particles A and B obtained for simulations of the set with a stray ion concentration $c_{\text{stray}} = 2 \times 10^{-4}$ M. $\sigma = 212$ nm designates the diameter of tracer particles. The self-organisation to pronounced liquid-like order among particles A and B is widely prohibited by electrostatic screening. Merely a weak first coordination shell is recognisable in the displayed partial pair distribution functions. The investigated asymmetry of matrix particles apparently has no significant effect on structure formation among matrix particles.	87
A.1	^1H nuclear magnetic resonance (NMR) spectra of the prepared monomers 2,2,2-trifluoroethyl acrylate (TFEA) and 1H,1H,5H-octafluoropentyl acrylate (OFPA) with deuterated chloroform as solvent.	X
A.2	$^{13}\text{C}\{^1\text{H}\}$ NMR spectra of the prepared monomers TFEA and OFPA with deuterated chloroform as solvent.	XI
A.3	$^{19}\text{F}\{^1\text{H}\}$ NMR spectra of the prepared monomers TFEA and OFPA with deuterated chloroform as solvent.	XII
B.1	Intermediate scattering functions $S_{BB}(Q, 0)$ at $t = 0$ of BB correlations obtained from BD simulations: under variation of the number density ratio $^1\rho_A/^1\rho_B$ (upper left), with different numbers of surface charges $Z_{\text{eff},A}$ and $Z_{\text{eff},B}$ (lower left), varying the particle diameters σ_A and σ_B (upper right), and changing the temperature T of the system (lower right). The reduced scattering vector $Q\sigma$ is displayed with $\sigma = \sigma_A$	XIII
B.2	Intermediate scattering functions $S_{AB}(Q, 0)$ at $t = 0$ of AB correlations obtained from BD simulations: under variation of the number density ratio $^1\rho_A/^1\rho_B$ (upper left), with different numbers of surface charges $Z_{\text{eff},A}$ and $Z_{\text{eff},B}$ (lower left), varying the particle diameters σ_A and σ_B (upper right), and changing the temperature T of the system (lower right). The reduced scattering vector $Q\sigma$ is displayed with $\sigma = \sigma_A$	XIV
C.1	Normalised relaxation of the global maxima of partial intermediate scattering functions $S_{BB,\text{max}}(Q\sigma, t)$ obtained by BD simulations under variation of: the number density ratio $^1\rho_A/^1\rho_B$ (upper left), numbers of surface charges $Z_{\text{eff},A}$ and $Z_{\text{eff},B}$ (lower left), particle diameters σ_A and σ_B (upper right), and the system temperature T (lower right). The reduced scattering vector $Q\sigma$ is displayed with $\sigma = \sigma_A$	XV
C.2	Normalised relaxation of the global maxima of partial intermediate scattering functions $S_{AB,\text{max}}(Q\sigma, t)$ obtained by BD simulations under variation of: the number density ratio $^1\rho_A/^1\rho_B$ (upper left), numbers of surface charges $Z_{\text{eff},A}$ and $Z_{\text{eff},B}$ (lower left), particle diameters σ_A and σ_B (upper right), and the system temperature T (lower right). The reduced scattering vector $Q\sigma$ is displayed with $\sigma = \sigma_A$	XVI

List of Tables

2.1	General classification of colloidal dispersions depending on the aggregate states of dispersed and continuous phase	4
3.1	Particle diameters σ , relative number densities ${}^1\rho_i/{}^1\rho_{\text{total}}$, and surface charges Z_{eff} defined for the reference system in BD simulations of ternary mixtures.	26
4.1	Compilation of the quantities of monomers, radical initiator, $\text{K}_2\text{S}_2\text{O}_8$, and redox catalyst system of $\text{Na}_2\text{SO}_3/(\text{NH}_4)_2\text{Fe}(\text{SO}_4)_2$ as well as topological parameters of the resulting colloidal polymer particles. The two digits in the copolymer sample names indicate the molar ratio of BA in the monomer mixture in percent. The molar quantities n_{mono} for the copolymers are displayed as $n_{\text{TFEA}} + n_i$, with i denoting BA or OFPA, respectively. For monomer amounts indicated by an asterisc, in addition 1 mmol of the crosslinker EGDMA is added to the monomer mixture. The refractive indices n_p are determined at ambient temperature for $\lambda = 532 \text{ nm}$. The Einstein self-diffusion coefficients D_0 are determined in aqueous dispersion containing $10^{-3} \text{ mol L}^{-1}$ KCl at $T = 298 \text{ K}$	28
4.2	Compilation of results derived from static structure factors of liquid-like ordered dispersions employing RMSA. Lower case characters at the end of the sample names indicate dilutions of the same colloidal dispersion. Given are the most probable next neighbour distance d_{max} , the amplitude of the coordination maximum $S_{\text{max}}(Q)$, the number of effective particle surface charges Z_{eff} and the particle number density ${}^1\rho$. n_m is the refractive index and ϵ_r the relative permittivity of the dispersion medium.	37
4.3	Compilation of numbers of effective surface charges Z_{eff} determined by RMSA-fit of SLS data and by BD simulations. Generally, BD delivers significantly smaller charge numbers, due to the known overestimation of Z_{eff} by RMSA. A rough tendency of growing discrepancy between Z_{eff} (BD) and Z_{eff} (RMSA) is identified with increasing charge number.	40
5.1	Compilation of short-time (D_S^S) and long-time (D_S^L) self-diffusion coefficients of PS3 tracers determined for the first sample set with varying tracer number density.	51
5.2	Compilation of short-time (D_S^S) and long-time (D_S^L) self-diffusion coefficients of PS3 tracers determined for the second sample set with varying matrix number density. Also the impact of adding 10^{-3} M KCl is shown. .	51

5.3	Particle diameters σ_i , numbers of surface charges $Z_{\text{eff},i}$ and total colloidal number density ${}^1\rho_{\text{total}}$ for BD simulation of PS3 tracers in a pTFEA VI matrix. Dynamic viscosity η and permittivity ε_r are adjusted for a water/glycerol dispersion medium with a refractive index $n_m = 1.3945$, corresponding to a glycerol mass ratio of 47.5%. Subscripts A and B denote properties of PS3 and pTFEA VI, respectively.	54
5.4	Long-time self-diffusion coefficients of PS3 tracers obtained from BD simulations of binary mixtures with different compositions. $D_S^{L,23}$ and $D_S^{L,50}$ correspond to upper time limits of 23 ms and 50 ms, respectively, for the determination of the long-time self-diffusion coefficients.	55
5.5	Total colloidal number density ${}^1\rho_{\text{total}}$, relative number densities ${}^1\rho_i/{}^1\rho_{\text{total}}$, particle diameters σ_i and numbers of surface charges $Z_{\text{eff},i}$ defined for BD simulation of the reference system for systematic investigations of binary mixtures with similar number densities. Subscripts A and B denote properties of the corresponding component.	66
5.6	Parameters of the first simulation set: variation of the number densities ${}^1\rho_A$ and ${}^1\rho_B$	67
5.7	Parameters of the second simulation set: variation of particle diameters σ_A and σ_B	67
5.8	Parameters of the third simulation set: variation of effective surface charges $Z_{\text{eff},A}$ and $Z_{\text{eff},B}$	67
5.9	Parameters of the fourth simulation set: variation of temperature T , viscosity η and permittivity ε_r of the medium.	67
5.10	Compilation of collective short-time (D^S) and long-time (D^L) diffusion coefficients for the simulated binary reference system and two chosen examples of simulations with varied parameters. For all three presented simulations diffusion coefficients are determined at the global maxima of the corresponding intermediate scattering functions with the scattering vectors: $Q_{AA} = 1.30 \times 10^{-2} \text{ nm}^{-1}$, $Q_{AB} = 1.34 \times 10^{-2} \text{ nm}^{-1}$, and $Q_{BB} = 1.38 \times 10^{-2} \text{ nm}^{-1}$. The short-time self-diffusion coefficients of particles A ($D_{S,A}^S$) and B ($D_{S,B}^S$) are calculated for comparison according to the Stokes-Einstein relation.	78
6.1	Adjusted particle sizes σ_i and effective surface charges $Z_{\text{eff},i}$ for matrix components A and B in the first simulation set of ternary mixtures. A constant surface charge density of the particles is maintained.	80
6.2	Number densities ${}^1\rho_i$ of matrix components A and B defined for the second simulation set ensuring a constant total charge number. Matrix particle sizes and charge numbers are identical to the first simulation set.	80
6.3	Further simulation sets with modifications of the total colloidal number density ${}^1\rho_{\text{total}}$ and addition of a given concentration of stray ions c_{stray} . Remaining simulation parameters are identical to those of the second simulation set defined in table 6.2.	80

Bibliography

- [1] J. C. Brown and P. N. Pusey. Measurement of diffusion coefficients of polydisperse solutes by photon correlation spectroscopy. *J. Phys. D: Appl. Phys.*, 7(2):L31–L35, 1974.
- [2] M. Sutton. A review of x-ray intensity fluctuation spectroscopy. *C. R. Phys.*, 9(5-6):657–667, 2008.
- [3] T. Graham. Liquid diffusion applied to analysis. *Phil. Trans. R. Soc. Lond.*, 151:183–224, 1861.
- [4] S. G. Mokrushin. Thomas graham and the definition of colloids. *Nature*, 195:861, 1962.
- [5] C. W. W. Ostwald. *Grundriss der Kolloidchemie*. Theodor Steinkopff, Dresden, 1909.
- [6] C. W. W. Ostwald. *Die Welt der vernachlässigten Dimensionen. Eine Einführung in die Kolloidchemie mit besonderer Berücksichtigung ihrer Anwendungen*. Theodor Steinkopff, Dresden, 1914.
- [7] C. W. W. Ostwald and M. Fischer. *An introduction to theoretical and applied colloid chemistry, "the world of neglected dimensions"*. John Wiley & Sons, Inc., New York, 1917.
- [8] W. van Megen, R. H. Ottewill, S. M. Owens, and P. N. Pusey. Measurement of the wave-vector dependent diffusion coefficient in concentrated particle dispersions. *J. Chem. Phys.*, 82(1):508–515, 1985.
- [9] W. van Megen and P. N. Pusey. Dynamic light-scattering study of the glass transition in a colloidal suspension. *Phys. Rev. A*, 43(10):5429–5441, 1991.
- [10] W. van Megen, S. M. Underwood, and P. N. Pusey. Nonergodicity parameters of colloidal glasses. *Phys. Rev. Lett.*, 67(12):1586–1589, 1991.
- [11] G. Cinacchi, Y. Martinez-Raton, L. Mederos, G. Navascues, A. Tani, and E. Velasco. Large attractive depletion interactions in soft repulsive-sphere binary mixtures. *J. Chem. Phys.*, 127(21), 2007.
- [12] D. Paloli, P. S. Mohanty, J. J. Crassous, E. Zaccarelli, and P. Schurtenberger. Fluid-solid transitions in soft-repulsive colloids. *Soft Matter*, 9:3000–3004, 2013.
- [13] W. Härtl and H. Versmold. Temperature dependence of the structure factor $s(q)$ of liquid-like ordered colloidal dispersions. *J. Chem. Phys.*, 81(5):2507–2510, 1984.
- [14] W. Härtl and X. Zhang-Heider. The synthesis of a new class of polymer colloids with a low index of refraction. *J. Colloid Interface Sci.*, 185:398–401, 1997.

- [15] F. M. Horn, W. Richtering, J. Bergenholtz, N. Willenbacher, and N. J. Wagner. Hydrodynamic and colloidal interactions in concentrated charge-stabilized polymer dispersions. *J. Colloid Interface Sci.*, 225(1):166–178, 2000.
- [16] J. Wagner, W. Härtl, and H. Walderhaug. Long time self-diffusion in suspensions of highly charged colloids: a comparison between pulsed field gradient nmr and brownian dynamics. *J. Chem. Phys.*, 114(2):975–983, 2001.
- [17] A. Yethiraj and A. van Blaaderen. A colloidal model system with an interaction tunable from hard sphere to soft and dipolar. *Nature*, 421(6922):513–517, 2003.
- [18] J. Wagner, B. Fischer, and T. Autenrieth. Field induced anisotropy of charged magnetic colloids: a rescaled mean spherical approximation study. *J. Chem. Phys.*, 124:114901, 2006.
- [19] J. Wagner, B. Fischer, T. Autenrieth, and R. Hempelmann. Structure and dynamics of charged magnetic colloids. *J. Phys.: Condens. Matter*, 18:S2697–S2711, 2006.
- [20] M. Dijkstra, J. P. Hansen, and P. Madden. Gelation of a clay colloid suspension. *Phys. Rev. Lett.*, 75:2236–2239, 1995.
- [21] M. Dijkstra, J.-P. Hansen, and P. A. Madden. Statistical model for the structure and gelation of smectite clay suspensions. *Phys. Rev. E*, 55:3044–3053, 1997.
- [22] J. C. Brown, P. N. Pusey, J. W. Goodwin, and R. H. Ottewill. Light scattering study of dynamic and time-averaged correlation in dispersions of charged particles. *J. Phys. A: Math. Gen.*, 8(5):664–682, 1975.
- [23] W. C. K. Poon. Colloids as big atoms. *Science*, 304:830–831, 2004.
- [24] N. Sultanova, S. Kasarova, and I. Nikolov. Dispersion properties of optical polymers. *Acta Phys. Pol., A*, 116(4):585–587, 2009.
- [25] F. Stieber and W. Richtering. Fiber-optic-dynamic-light-scattering and two-color-cross-correlation studies of turbid, concentrated, sterically stabilized polystyrene latex. *Langmuir*, 11(12):4724–4727, 1995.
- [26] L. F. Rojas, R. Vavrin, C. Urban, J. Kohlbrecher, A. Stradner, F. Scheffold, and P. Schurtenberger. Particle dynamics in concentrated colloidal suspensions. *Faraday Discuss.*, 123:385–400, 2003.
- [27] B. Vincent. *Colloid Science: Principles, Methods and Applications*, chapter Introduction to Colloidal Dispersions, pages 1–13. Blackwell Publishing Ltd., Oxford, UK, 2005.
- [28] H.-D. Dörfler. *Grenzflächen und kolloid-disperse Systeme - Physik und Chemie*. Springer, 2002.
- [29] S. Slomkowski, J. V. Alemán, R. G. Gilbert, M. Hess, K. Horie, R. G. Jones, P. Kubisa, I. Meisel, W. Mormann, S. Penczek, and R. F. T. Stepto. Terminology of polymers and polymerization processes in dispersed systems (iupac recommendations 2011). *Pure Appl. Chem.*, 83(12), 2011.

- [30] K. Tauer. *Colloids and Colloid Assemblies*, chapter Latex Particles, pages 1–51. Wiley-VCH, Weinheim, 2004.
- [31] D. J. Siler and K. Cornish. A protein from ficus-elastica rubber particles is related to proteins from hevea-brasiliensis and parthenium-argentatum. *Phytochemistry*, 1993.
- [32] H. C. Hamaker. The london – van der waals attraction between spherical particles. *Physica*, 1937.
- [33] B. V. Derjaguin and L. D. Landau. Theory of the stability of strongly charged lyophobic sols and of the adhesion of strongly charged particles in solutions of electrolytes. *Acta Phys. Chim. URSS*, 14:633–662, 1941.
- [34] E. J. W. Verwey and J. T. G. Overbeek. *Theory of the Stability of Lyophobic Colloids*. Elsevier, 1948.
- [35] N. A. Clark, A. J. Hurd, and B. J. Ackerson. Single colloidal crystals. *Nature*, 281:57–60, 1979.
- [36] T. Palberg. Crystallization kinetics of colloidal model suspensions: recent achievements and new perspectives. *J. Phys.: Condens. Matter*, 26(33), 2014.
- [37] W. Härtl, H. Versmold, and X. Zhang-Heider. The glass transition of charged polymer colloids. *J. Chem. Phys.*, 102:6613, 1995.
- [38] P. N. Pusey and W. van Meegen. Phase behaviour of concentrated suspensions of nearly hard colloidal spheres. *Nature*, 320:340–342, 1986.
- [39] J. Wagner, C. Märkert, B. Fischer, and L. Müller. Direction dependent diffusion of aligned magnetic rods by means of x-ray photon correlation spectroscopy. *Phys. Rev. Lett.*, 110:048301, 2013.
- [40] L. K. Mansson, J. N. Immink, A. M. Mihut, P. Schurtenberger, and J. J. Crassous. A new route towards colloidal molecules with externally tunable interactions sites. *Faraday Discuss.*, 181:49–69, 2015.
- [41] D. J. Pine, D. A. Weitz, P. M. Chaikin, and E. Herbolzheimer. Diffusing-wave spectroscopy. *Phys. Rev. Lett.*, 60(12):1134–1137, 1988.
- [42] G. Maret. Diffusing-wave spectroscopy. *Curr. Opin. Colloid Interface Sci.*, 2(3):251–257, 1997.
- [43] O. Kratky and G. Porod. Diffuse small-angle scattering of x-rays in colloid systems. *J. Colloid Sci.*, 4(1):35–70, 1949.
- [44] M. Stieger, W. Richtering, J. S. Pedersen, and P. Lindner. Small-angle neutron scattering study of structural changes in temperature sensitive microgel colloids. *J. Chem. Phys.*, 120(13):6197–6206, 2004.
- [45] R. Brown. A brief account of microscopical observations made in the months of june, july and august, 1827, on the particles contained in the pollen of plants; and on the general existence of active molecules in organic and inorganic bodies. *Philos. Mag.*, 4:161–173, 1828.

- [46] J. Ingenhousz. *Vermischte Schriften von Ingenhousz*, chapter Bemerkungen über den Gebrauch des Vergrößerungsglases, pages 123–124. Wien, 1784.
- [47] A. Einstein. Über die von der molekularkinetischen theorie der wärme geforderte bewegung von in ruhenden flüssigkeiten suspendierten teilchen. *Annalen der Physik*, 17:549–560, 1905.
- [48] M. von Smoluchowski. Zur kinetischen theorie der brownschen molekularbewegung und der suspensionen. *Annalen der Physik*, 21:756–780, 1906.
- [49] P. Langevin. Sur la theorie du mouvement brownien. *Comptes Rendus*, 146:530, 1908.
- [50] J.-B. Perrin. Mouvement brownien et realite moleculaire. *Annales de chimie et de physique*, 18:5–114, 1909.
- [51] S. L. Lauritzen. *Thiele: Pioneer in Statistics*. Oxford University Press, 2002.
- [52] N. Wiener. Generalized harmonic analysis. *Acta Math.*, 55:117–258, 1930.
- [53] R. Zwanzig. Memory effects in irreversible thermodynamics. *Phys. Rev.*, 124:983, 1961.
- [54] H. Mori. Transport, collective motion, and brownian motion. *Progr. Theor. Phys.*, 33(3):423–455, 1965.
- [55] D. L. Ermak. A computer simulation of charged particles in solution. i. technique and equilibrium properties. *J. Chem. Phys.*, 1975.
- [56] B. J. Berne and R. Pecora. *Dynamic Light Scattering - With Applications to Chemistry, Biology and Physics*. Dover Publications, 2000.
- [57] J. B. Hayter and J. Penfold. Self-consistent structural and dynamic study of concentrated micelle solutions. *J. Chem. Soc., Faraday Trans. 1*, 77:1851–1863, 1981.
- [58] R. Pecora and S. R. Aragon. Theory of light scattering from hollow spheres. *Chem. Phys. Lipids*, 13:1–10, 1974.
- [59] W. C. K. Poon and D. Andelman, editors. *Soft Condensed Matter Physics in Molecular and Cell Biology*. CRC Press, 2006.
- [60] M. P. Allen and D. J. Tildesley. *Computer Simulation of Liquids*. Oxford University Press, 1997.
- [61] L. S. Ornstein and F. Zernike. Accidental deviations of density and opalescence at the critical point of a single substance. *Proc. Akad. Sci. (Amsterdam)*, 17:793–806, 1914.
- [62] M. S. Wertheim. Exact solution of the percus-yevick integral equation for hard spheres. *Phys. Rev. Lett.*, 10(8):321–323, 1963.
- [63] J. L. Lebowitz and J. K. Percus. Mean spherical model for lattice gases with extended hard cores and continuum fluids. *Phys. Rev.*, 144(1):251–258, 1966.

- [64] G. Nägele. *The physics of colloidal soft matter - Lecture Notes 14*. Institute of Fundamental Technological Research, Warsaw, 2004.
- [65] J.-P. Hansen and J. B. Hayter. A rescaled msa structure factor for dilute charged colloidal dispersions. *Mol. Phys.*, 46(3):651–656, 1982.
- [66] A. J. F. Siegert. *On the fluctuations in signals returned by many independently moving scatterers*. [Cambridge, Mass.] : Radiation Laboratory, Massachusetts Institute of Technology, 1943.
- [67] A. R. Altenberger and J. M. Deutch. Light scattering from dilute macromolecular solutions. *J. Chem. Phys.*, 59(2):894–898, 1973.
- [68] D. E. Koppel. Analysis of macromolecular polydispersity in intensity correlation spectroscopy: The method of cumulants. *J. Chem. Phys.*, 57(11):4814–4820, 1972.
- [69] J. Hadamard. Sur les problèmes aux dérivés partielles et leur signification physique. *Princeton University Bulletin*, 13:49–52, 1902.
- [70] B. J. Frisken. Revisiting the method of cumulants for the analysis of dynamic light-scattering data. *Appl. Opt.*, 40(24):4087–4091, 2001.
- [71] S. W. Provencher. Contin - a general-purpose constrained regularization program for inverting noisy linear algebraic and integral-equations. *Comput. Phys. Commun.*, 27(3):229–242, 1982.
- [72] S. W. Provencher. A constrained regularization method for inverting data represented by linear algebraic or integral-equations. *Comput. Phys. Commun.*, 27(3):213–227, 1982.
- [73] A. N. Tikhonov and V. Y. Arsenin. *Solutions of Ill-Posed Problems*. Winston, New York, 1977.
- [74] G. Nägele. On the dynamics and structure of charge-stabilized suspensions. *Phys. Rep.*, 272(5-6):215–372, 1996.
- [75] H. Löwen, T. Palberg, and R. Simon. Dynamical criterion for freezing of colloidal liquids. *Phys. Rev. Lett.*, 70(10):1557–1560, 1993.
- [76] J.-P. Hansen and L. Verlet. Phase transitions of the lennard-jones system. *Phys. Rev.*, 184(1), 1969.
- [77] B. J. Ackerson, P. N. Pusey, and R. J. A. Tough. Interpretation of the intermediate scattering function at short times. *J. Chem. Phys.*, 76(3):1279–1282, 1982.
- [78] G. Nägele and P. Baur. Long-time dynamics of charged colloidal suspensions: hydrodynamic interaction effects. *Physica A*, 245(3-4):297–336, 1997.
- [79] P. N. Pusey. *Liquids, freezing and glass transition*, chapter Colloidal suspensions, pages 763–942. Amsterdam: Elsevier, 1991.
- [80] P. Baur, G. Nägele, and R. Klein. Nonexponential relaxation of density fluctuations in charge-stabilized colloids. *Phys. Rev. E*, 53(6):6224–6237, 1996.

- [81] J. Rotne and S. Prager. Vocolloids treatment of hydrodynamic interactions in polymers. *J. Chem. Phys.*, 50(11):4831–4837, 1969.
- [82] C. Beenakker and P. Mazur. Diffusion of spheres in a concentrated suspension ii. *Physica A: Statistical Mechanics and its Applications*, 126(3):349–370, 1984.
- [83] U. Genz and R. Klein. Collective diffusion of charged spheres in the presence of hydrodynamic interaction. *Physica A*, 171:26–42, 1991.
- [84] C. Schotten. Ueber die oxydation des piperidins. *Berichte der deutschen chemischen Gesellschaft*, 17(2):2544–2547, 1884.
- [85] E. Baumann. Ueber eine einfache methode der darstellung von benzoessäureäthern. *Berichte der deutschen chemischen Gesellschaft*, 19(2):3218–3222, 1886.
- [86] D. W. Coddling, T. S. Reid, A. H. Ahlbrecht, G. H. J. Smith, and D. R. Husted. Fluorine-containing polymers. ii. 1,1-dihydroperfluoroalkyl acrylates: Preparation of monomers. *J. Polym. Sci.*, 15:515–519, 1955.
- [87] B. Boutevin, G. Regal, and A. Rousseau. Synthèse de Matériaux Polymères Transparents - Partie II Synthèse et Polymérisation d'Acrylates et de Méthacrylates d'Halogénoalkyle. *Journal of Fluorine Chemistry*, 38:47–73, 1988.
- [88] P. A. Lovell and M. S. El-Aasser, editors. *Emulsion Polymerization and Emulsion Polymers*. John Wiley & Sons, Chichester, 1997.
- [89] D. C. Blackley. *Polymer Latices: Science and Technology*. Springer Springer & Business Media, 2nd edition, 1997.
- [90] J. Wagner, W. Härtl, and R. Hempelmann. Characterization of monodisperse colloidal particles: comparison between saxs and dls. *Langmuir*, 16(9):4080–4085, 2000.
- [91] M. Schmitt, J. Wagner, G. Jung, and R. Hempelmann. Functionalized polymer colloids bearing primary amino groups. *J. Colloid Interface Sci.*, 311:425–429, 2007.
- [92] B. Fischer, J. Wagner, C. Gutt, F. Westermeier, and G. Grübel. Structure and dynamics of glassy charged colloids studied with coherent small angle x-ray scattering. *J. Phys.: Conf. Ser.*, 247(1):012026, 2010.
- [93] L. F. Hoyt. New table of the refractive index of pure glycerol at 20°C. *Ind. Eng. Chem.*, 26(3):329–332, 1934.
- [94] C. Passow. *Untersuchungen richtungsabhängiger Phänomene in kolloidalen Systemen*. PhD thesis, University of Rostock, 2015.
- [95] R. G. Gilbert, M. Hess, A. D. Jenkins, R. G. Jones, P. Kratochvil, and R. F. T. Stepto. Dispersity in polymer science. *Pure Appl. Chem.*, 81(2):351–353, 2009.
- [96] P. J. Flory. Fundamental principles of condensation polymerization. *Chem. Rev.*, 39(1):137–197, 1946.

- [97] G. V. Schulz. Molecular weight determination in macromolecular compounds. viii. distribution function of multimolecular compounds and their determination by fractionation. *Z. Phys. Chem. (Muenchen, Ger.)*, B47:155–193, 1949.
- [98] J. Wagner. Small-angle scattering from spherical core-shell particles: an analytical scattering function for particles with schulz-flory size distribution. *J. Appl. Crystallogr.*, 37(5):750–756, 2004.
- [99] B. Fischer, T. Autenrieth, and J. Wagner. Highly charged inorganic-organic colloidal core-shell particles. *Langmuir*, 26(9):6201–6205, 2010.
- [100] D. L. Ermak and J. A. McCammon. Brownian dynamics with hydrodynamic interactions. *J. Chem. Phys.*, 69(4):1352–1360, 1978.
- [101] P. Linse. Accurate solution of a highly asymmetric electrolyte: Molecular dynamics simulation and integral equation. *J. Chem. Phys.*, 93(2):1376–1385, 1990.
- [102] L. Verlet. Computer "experiments" on classical fluids. i. thermodynamical properties of lennard-jones molecules. *Phys. Rev.*, 159(1):98–103, 1967.
- [103] E. Hairer, C. Lubich, and G. Wanner. Geometric numerical integration illustrated by the störmer-verlet method. *Acta Numerica*, 12:399–450, 2003.
- [104] N. I. of Advanced Industrial Science and T. A. Japan. Spectral database for organic compounds. http://sdbs.db.aist.go.jp/sdbs/cgi-bin/direct_frame_disp.cgi?sdbno=11294. accessed 24-November-2016.
- [105] N. I. of Advanced Industrial Science and T. A. Japan. Spectral database for organic compounds. http://sdbs.db.aist.go.jp/sdbs/cgi-bin/direct_frame_disp.cgi?sdbno=51363. accessed 24-November-2016.
- [106] J. Wagner, W. Härtl, C. Lellig, R. Hempelmann, and H. Walderhaug. Complex liquids consisting of low- t_g polymer- colloids: structure and self-diffusion. *J. Molecular Liquids*, 98:183–190, 2002.
- [107] W. Yao, Y. Li, and X. Huang. Fluorinated poly(meth)acrylate: synthesis and properties. *Polymer*, 55(24):6197–6211, 2014.
- [108] D. A. McQuarrie. *Statistical Mechanics*. University Science Books, 2000.
- [109] W. Härtl, C. Beck, and R. Hempelmann. Determination of hydrodynamic properties in highly charged colloidal systems using static and dynamic light scattering. *J. Chem. Phys.*, 110(14):7070–7072, 1999.
- [110] W. Härtl, J. Wagner, C. Beck, F. Gierschner, and R. Hempelmann. Self-diffusion and hydrodynamic interactions in highly charged colloids. *J. Phys.: Condens. Matter*, 12:A287–A293, 2000.
- [111] E. Marx and G. W. Mulholland. Size and refractive index determination of single polystyrene spheres. *Journal of Research of the National Bureau of Standards*, 88(5):321–338, 1983.

- [112] X. Ma, J. Q. Lu, R. S. Brock, K. M. Jacobs, P. Yang, and X.-H. Hu. Determination of complex refractive index of polystyrene microspheres from 370 to 1610 nm. *Phys. Med. Biol.*, 48(24):4165, 2003.
- [113] R. Krause, J. L. Arauz-Lara, G. Nägele, H. Ruiz-Estrada, M. Medina-Noyola, R. Weber, and R. Klein. Statics and tracer-diffusion in binary suspensions of polystyrene spheres: experiment vs. theory. *Physica A*, 1991.
- [114] R. Krause, G. Nägele, J. L. Arauz-Lara, and R. Weber. Brownian motion in binary colloidal suspensions. *J. Colloid Interface Sci.*, 1992.
- [115] G. Nägele, T. Zwick, R. Krause, and R. Klein. Brownian motion in polydisperse charged colloidal suspensions. *J. Colloid Interface Sci.*, 1993.
- [116] W. Härtl and X. Zhang-Heider. Tracer diffusion of highly charged polymer colloids. *J. Chem. Phys.*, 105(21):9625–9632, 1996.
- [117] A. van Blaaderen, J. Peetermans, G. Maret, and J. K. G. Dhont. Long-time self-diffusion of spherical colloidal particles measured with fluorescence recovery after photobleaching. *J. Chem. Phys.*, 96(6):4591–4603, 1992.
- [118] J. G. Kirkwood and F. P. Buff. The statistical mechanical theory of solutions. i. *J. Chem. Phys.*, 19(6):774–777, 1951.
- [119] R. Venkatesh and R. V. G. Rao. Total and partial structure factor, compressibility, diffusion coefficients and other associated properties of an ag-se semiconducting alloy. *Journal of Molecular Structure (Theochem)*, 361:283–288, 1996.
- [120] V. Pierce, M. Kang, M. Aburi, S. Weerasinghe, and P. E. Smith. Recent applications of kirkwood-buff theory to biological systems. *Cell Biochem. Biophys.*, 50(1):1–22, 2008.
- [121] T. E. Colla, A. P. dos Santos, and Y. Levin. Equation of state of charged colloidal suspensions and its dependence on the thermodynamic route. *J. Chem. Phys.*, 136:194103, 2012.

Danksagung

Prof. Dr. Joachim Wagner danke ich für die Gelegenheit mich nach meiner Masterarbeit weiter in die "Welt der vernachlässigten Dimensionen" zu vertiefen und dieses interessante und anspruchsvolle Thema zu bearbeiten. Für die geleistete Unterstützung bei Problemen vielfältiger Art, die während einer Doktorarbeit naturgemäß auftreten können, bin ich ihm insbesondere dankbar.

Ich danke Prof. Dr. Ralf Stannarius für die Erstellung des zweiten Gutachtens meiner Dissertation und die darin enthaltenen wertvollen Anmerkungen und Hinweise.

Dr. Christopher Passow möchte ich für die stete Bereitschaft danken, mir bei den kleinen und auch großen Herausforderungen des Doktorandenalltags jederzeit behilflich zu sein. Wenn ich mich recht erinnere, gab es keine Frage, die von ihm unbeantwortet blieb. Annemarie Nack bin ich für immer auf professioneller wie auf persönlicher Ebene zu tiefstem Dank verpflichtet. In der Summe aller Faktoren, war die Zeit, in der wir ein Büro geteilt haben mit Sicherheit die Beste während der Doktorarbeit. Annemarie und Christopher: abseits des Alltags im charmanten Dr.-Lorenz-Weg, werden mir besonders die Reisen zu Workshops und Konferenzen mit euch immer sehr gut in Erinnerung bleiben.

Sabine Kindermann und Margitta Prieß danke ich für die unvergleichliche, familiäre Atmosphäre auf "unserem" Flur. Daneben haben sie unschätzbare und unkomplizierte Hilfe bei allen administrativen Problemen geleistet.

Michael Koof bin ich zu großem Dank verpflichtet. Das Gelingen dieser Arbeit basiert zu einem signifikanten Teil auch auf unserer effektiven Zusammenarbeit während der ersten zwei Jahre meiner Doktorarbeit. Julian Seifert, Kira Arndt, Elisabeth Herold und Philipp Marienhagen danke ich für die schöne gemeinsame Zeit in der Arbeitsgruppe von Prof. Wagner.

Den übrigen Angehörigen der Physikalischen Chemie an der Universität Rostock danke ich für die freundliche Aufnahme in die Abteilung und die Möglichkeit, mich durch die Betreuung von Studenten im Praktikum persönlich und professionell weiter zu entwickeln.

Den analytischen Abteilungen des Institutes für Chemie und dem Elektronenmikroskopiezentrum der Universitätsmedizin Rostock danke ich für die Hilfe bei der Charakterisierung meiner Proben.

Den Kollegen von der Universität Siegen und vom DESY in Hamburg, insbesondere Prof. Dr. Christian Gutt und Matthias Kampmann, danke ich für die Gelegenheiten an Messzeiten am PSI und am DESY teilzunehmen und dabei interessante Phänomene zu untersuchen, die nicht direkt mit meinem eigenen Thema in Verbindung stehen.

Meinen Freunden und meiner Familie gebührt mein großer Dank dafür, dass sie mir immer ein Rückhalt sind und mich auf so vielfältige Weise unterstützen.

Abschließend gebührt mein unermesslicher und immerwährender Dank meiner Freundin, die mich so kennt wie niemand sonst, und die mir während der manchmal auch schwierigen Arbeit an dieser Dissertation ihre uneingeschränkte Geduld und Unterstützung entgegen gebracht hat. Juli: ohne dich wäre ich nicht in der Lage gewesen, diese Arbeit erfolgreich abzuschließen.

Selbständigkeitserklärung

Ich versichere hiermit an Eides statt, dass ich die vorliegende Arbeit selbständig und nur unter Verwendung der von mir angegebenen Hilfsmittel und Quellen angefertigt habe. Die den benutzten Werken inhaltlich oder wörtlich entnommenen Stellen habe ich entsprechend kenntlich gemacht. Die Arbeit wurde bisher in gleicher oder ähnlicher Form in keiner anderen Prüfungsbehörde vorgelegt und auch noch nicht veröffentlicht.

Rostock, 24.03.2017

Unterschrift